Micro/Nano Machining of Steel and Tungsten Carbide Utilizing Elliptical Vibration Cutting Technology

Zhang Jianguo

A Thesis Submitted for the
Degree of Doctor of Philosophy
Department of Mechanical Engineering
Nagoya University
2014

Contents

Chapter 1

Introduction

1.1 Background

Structured surfaces with sophisticated micro/nano structures can provide advanced and useful functions, such as hydrophobicity, low friction, beam path guiding, and so on [1]. To achieve the maximum benefit from the structured surfaces, application technologies of the micro/nano-structured surfaces have been a fascinating research topic in the last few decades. According to literatures, these structured surfaces have been increasingly demanded in various applications, such as optics, solar energy technology, bioengineering, self-cleaning, manufacturing, and so on. To promote widespread use of the structured surfaces, their applications and their mass production, manufacturing technology of structured surfaces for a variety of materials, especially for ultra-precision dies and molds made of hardened steel and tungsten carbide, is absolutely essential. Hardened steel and tungsten carbide can be used in high performance molding applications because of their unique and practical characteristics in physical, mechanical, thermal and chemical properties.

In this section, comprehensive survey associated with structured surface technologies is addressed as a background of the present thesis. Firstly, representative applications of structured surfaces are introduced in Section 1.1.1. Subsequently, conventional fabrication methods of micro/nano structured surfaces are presented in Section 1.1.2. Then, elliptical vibration cutting technology, which is utilized in the proposed fabrication method, is introduced in Section 1.1.3.

1.1.1 Application of micro/nano structures

1.1.1.1 Optics

In optical industry, sophisticated micro/nano structures have greatly applied to optical elements in order to satisfy both the maximum optical functions and the

miniaturization requirements arising from the communications, computing, consumer electronics and aerospace industries. There are numerous applications of structured optics in reflective, refractive, and diffractive optical systems. They are mainly used for guiding the beam path to obtain high-performance imaging, concentration, illumination and other applications. For example, a diffractive grating is an optical component and is applied to digital lens (EF 400mm F4L DO IS, Canon inc.) to cancel out the glare [2], as shown in Fig. 1.1.

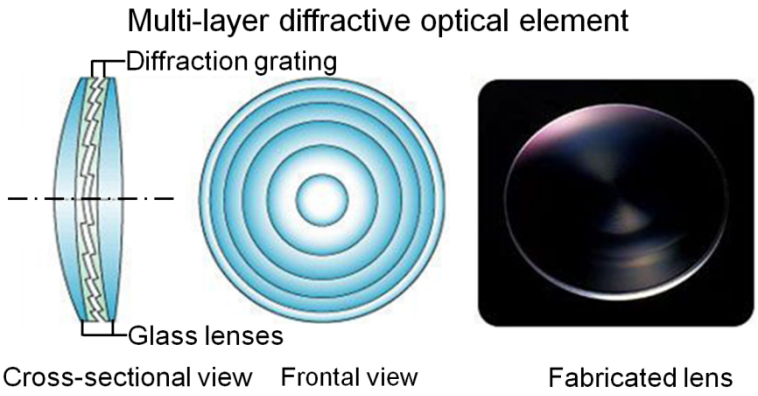

Fig. 1.1 Diffraction grating for digital camera in Canon inc. [2]

Li and Yi [3] designed and fabricated a freeform micro lens array for a compact large-field-of-view compound-eye camera in image formation. The molded micro lens array can achieve a large-field-of-view and can be directly integrated with an imaging detector to form a compact camera. It has further potential applications in motion/position detection, machine vision, and robotics for its large-field-of-view with low cost. Reichle, et al. [4] also presented an aspheric surface with diffractive microstructure. It can cope with the image aberration and the chromatic aberration and improve the imaging quality. This optical element reduces the components number effectively, and satisfies the requirements of miniaturized and compact designs.

There are also several other micro/nano structures used for optical industry. For example, D.Shieh et al. [5] confirmed that micro grooves and micro dimples can be used as backlight panels of LCD (Liquid Crystal Display) to achieve the improvement of brightness and scatter. A freeform lens array was optimized by Sun et al. [6] to produce

a controlled luminance distribution on the road surface and improve the overall road surface luminance uniformity.

1.1.1.2 Solar energy technology

During the recent two decades, several micro/nano structures have been pioneered for solar energy concentration, where the purpose is to collect the incident light from a large incident aperture to a small exit aperture. Solar energy concentration technology using regularly-arrayed Fresnel lens is an effective way to make full use of sunlight, as reported by Xie et al. [7]. It is installed in order to concentrate sunlight and raise the efficiency of the power generation in the solar cell system. Suzuki et al. [8] presented that the sunlight onto the solar cell can be irradiated uniformly by the glass Fresnel lenses.

1.1.1.3 Bioengineering

In bioengineering, textured surface with micro/nano structures firstly appeared in the literature in 1959 when Lewis and McCutchen [9] published the article in Nature about the role that surface structure of cartilage played in lubricating animal joints. In the following decades, further understanding of surface phenomena, particularly at a micrometer and nanometer scale, has played a fundamental role in the development of bioengineering. An intersecting grooved surface applied to bioengineering was presented by Miyoshi et al. [10]. It can maintain a certain stem cell's viability and proliferation in a designed material niche and promote outward migration at an appropriate stage of differentiation. This functional structure can be applied to the separation of cancer cells from a mixture of cancer and normal cells. It has a significant benefit for the diagnosis in the basic cancer research. Moreover, Henry et al. [11] reported that micro needles can be applied to the transdermal drug delivery. They are fabricated long enough (about 150 μm) to cross the permeability barrier of skin but not so long that they stimulate nerves, therefore potentially causing no pain.

1.1.1.4 Self-cleaning

Some micro/nano structures can also be applied to self-cleaning, where the structures provide hydrophobic function. For example, these structures can be applied to glass protection industry. It allows dirt and water to simply wash off and decreases the

cost by nonuse of cleaning chemicals. One of the most famous examples of hydrophobic surface is reported in nature [12]. This kind of hydrophobic surface has a low surface energy and a high roughness or micro/nano structured surface relief. Callies et al. [13] applied a sample of pillars array to hydrophobic experiments. Different types of micro/nano structures, e.g., shallow cavities and micro grooves, can also be applied as hydrophobic surfaces as reported by Bico et al. [14].

1.1.1.5 Manufacturing industry

Furthermore, functional surfaces with micro/nano structures can be used to enhance the productivity and efficiency of the manufacturing industry. Lithographer is one of the established processes to manufacture diffractive optical elements and micro-structured surfaces. Wu et al. [15] show a freeform lens array for optical lithography that maximizes the image contrast and reduces the complexity of the exposure system.

Moreover, with the development of ultra-precision engineering, precision measurement in positioning of machine tool is necessary. Gao et al. [16, 17] applied micro/nano-structured surface with sinusoidal grids as a surface encoder to the measurement of multi-axis position. The optical path and the prototype sensor were proposed by Gao et al. [17]. With identical pitches (10 μm) and amplitudes (60 nm) of X- and Y-directional sine waves, the sensor has been verified to have the ability to distinguish 5 nm step motions. As compared with conventional multi-axis laser interferometers, this sensor is considered to be more thermally stable and less expensive for practical use.

According to tribological applications, it has been studied that friction between sliding surfaces can be reduced effectively by texturing in a micrometer scale. The micro-structures could be regarded as a set of micro-bearings distributed over the sliding surface [18, 19]. They can offer excellent tribological performances because of the improvement of lubrication and the enhancement of a hydrodynamic pressure due to the constituted converging wedges. Micro-structured surface is one of the potential applications to sliding surfaces in a manufacturing system with the decrease of the friction coefficient. With the aforementioned benefits, Kawasegi et al. [20] also certified

that micro/nano structures created on the tool rake face lead to efficient lubrication conditions and high cutting performance. Obikawa et al. [21] also confirmed that parallel type and square-dot type of micro-textures effectively improved the lubrication conditions as the pattern of texture became smaller and deeper.

Micro/nano-structured surfaces can exhibit a number of novel and excellent functions and features as compared with just simple smooth surfaces. They have also been used in various other applications. For example, micro-structured surfaces with micro pyramids of different heights can significantly improve the cooling performance of a super-heated wall [22]. Micro-lens array has been used in fiber coupling and optical switching, collimation of lasers diodes, beam homogenizers for lasers and illumination systems, creating the best imaging characteristics [23], and so on.

1.1.2 Fabrication methods of micro/nano structures

In order to utilize the structured surface technologies, high performance manufacturing technology is required for their fabrications. When the feature size of designed structure is downscaled into micrometer or nanometer level, those fabrications may become extremely challenging. To overcome this problem, numerous fabrication methods for micro/nano structure have been proposed so far. Typical methods for micro/nano structure fabrication are introduced comprehensively in this section.

1.1.2.1 Lithographic machining

A wide variety of lithographic methods are applied to the fabrication of micro/nano-scale structured surfaces. Photolithography is historically the most widely used micro-patterning technique. The size of the features can be precisely controlled in micrometer/nanometer dimensions [24]. Photolithography is often applied to semiconductor manufacturing of large-scale integration (LSI) circuits and also commonly used for the fabrication of microelectromechanical systems (MEMS) devices. Photolithography generally uses a pre-fabricated photomask or reticle as a master from which the final pattern is derived. Moreover, binary optics can also be fabricated by a series of steps in which the photoresist is exposed in an appropriate pattern and then etched. Setzu et al. [25] successfully applied photolithography to two-dimensional

optical microstructure fabrication in porous silicon. This process can fabricate some dense micro/nano structures with extremely short pitch, but it is mostly specific to a particular class of materials, highly sophisticated and expensive.

1.1.2.2 Laser beam machining

Laser light is highly directional and has high power density, resulting in better focusing performance. These unique characteristics of laser beam are useful in processing of materials. For laser beam machining, different types of lasers have been used for micromachining of diverse materials. Ultra-short excimer laser (wave length=157-248 nm) is one of the potential technologies for micro/nano structures fabrication on materials as diverse as polymers, glass, ceramics and metals [26, 27]. Both laser direct writing and excimer laser machining can be used effectively in fabricating microstructures [28].

1.1.2.3 Focused ion beam machining

Focused ion beam machining [29, 30] is an alternative method for fine structure fabrication, but the removal rate is very low, with the order of some $\mu m^3/s$. Gallium ions are typically used with the introduction of secondary gases into the focused ion beam system. The gallium (Ga+) ion beam hits the sample surface and sputters a small amount of material to form a micro/nano-scale structure. With a higher current of ion beam, a great volume of material can be removed by sputtering, allowing precision milling of the workpiece sample down to a sub micrometer or even several nanometer scales. This technology has been used to fabricate micro/nano-lens arrays [31-33], but the surface quality and machining accuracy are heavily dependent on the working temperature and pressure.

1.1.2.4 Electron beam machining

Electron beam machining [34] of micro/nano structures is an alternative to laser writing because it can achieve much smaller spot size. This technique is mainly developed for integrated circuit (IC) mask production and useful for production of micro-structured surfaces such as binary optics [1]. Electron beams have the advantage of consisting charged particles which can be influenced by electric and magnetic fields, and the wave length is even shorter than that of x-rays (0.01-10 nm), which is benefit for

nano structure machining [35]. The drawback is that it is a relatively time consuming and expensive technology for pattern generation. Therefore, it is mainly used in the fabrication of masks for lithography. In combination with replication techniques, electron beam can be an interesting approach to fabricate both refractive and diffractive optical elements [32].

1.1.2.5 Diamond machining

Diamond machining is crucial for the fabrication of micro-structured surfaces, either for direct machining of the parts or making of molds for their mass production. These processes mainly include diamond cutting and grinding.

Evans and Bryan [1] investigated capabilities and limitations in typical methods for micromachining such as cutting, laser machining, lithographic methods, focused ion beam machining, replication, and so on. Ultra-precision diamond cutting is superior to produce ultra-precision and sophisticated structures in the pitch range of several to hundreds micrometers practically. It also has many advantages of high geometrical accuracy, good surface quality and high machining efficiency. Diamond cutting allows a high degree of freedom for structural design as compared with other methods, and thus it has been widely used especially for plasitic molding applications of a variety of optical elements. Commercial diamond cutting machines are generally available for machining axisymmetric or free-form surfaces [36, 37], e.g. sphere and cone shape with optical-quality surface finish. However, due to the large moving mass, it is time consuming for the fabrication of micro-structured surfaces in practical application. To overcome this shortcoming, combination of the conventional diamond cutting and the fast tool servo (FTS) technology enables highly-efficient fabrication of micro/nano structures in a variety of applications [38-42]. Combining with mass production process such as injection molding and compression molding, diamond cutting becomes available for manufacturing of high-quality and low-cost consumer products, and hence, quickly popularizes among the related industries.

Among a series of diamond cutting technoques, the ultra-precision diamond milling is frequently utilized for fabrication of micro/nano structures. A high-speed spindle with a hydrostatic bearing is generally utilized in ultra-precision diamond milling, and

specially-designed milling tool made of diamond is mounted. This method is commonly used to fabricate simple micro-grooves and micro dimples. For example, a series of V-shaped, trapezoid-shaped, R-shaped, and square grooves are successfully fabricated on plastic materials with high machining accuracy [43-45]. Moreover, some micro structures are also fabricated on difficult-to-cut materials by micro milling process. Micro-lenses on a silicon plate are fabricated by rotating a circular arc diamond cutting edge and feeding the tool along an axis perpendicular to the silicon plate [44]. Recently, with the development of micro milling tool made of PCD, micro-Fresnel moulds and micro lens with concave spherical shape are successfully fabricated on binderless tungsten carbide [46-47].

Instead of diamond cutting, ultra-precision diamond grinding is also applied to the fabrication of micro/nano structures. Ultra-precision grinding is generally used to generate high quality and functional parts made from difficult-to-cut materials, such as ceramics, carbides, glasses, hardened steel, semiconductor materials, and so on [48]. In order to realize the fabrication of micro/nano structures, a number of microgrinding processes have been developed especially for decreasing the cutting tool dimensions and increasing the achievable aspect ratio. Hoffmeister and Wittmer [49] have successfully fabricated micro pillars array on silicon and silica glass substrates with microgrinding wheels. Suzuki [8, 50, 51] proposed a new 4-axes grinding system for fabricating micro array lens and micro-Fresnel shape on tungsten carbide for glass moulding. By applying a minimum wheel tip radius of 8.2 μm, Yin and Ohmori [52] introduced a V-groove fabrication process to obtain large arrayed microstructures with constant surface quality on germanium.

Based on the aforementioned reference literatures, the typical machining dimensions of periodic patterns fabricated by the different micromachining methods are investigated. The relationships between the representative heights and pitches of the patterns are approximately evaluated and presented in Fig. 1.2. These relations indirectly represent the capabilities of machining geometry in the micro machining methods.

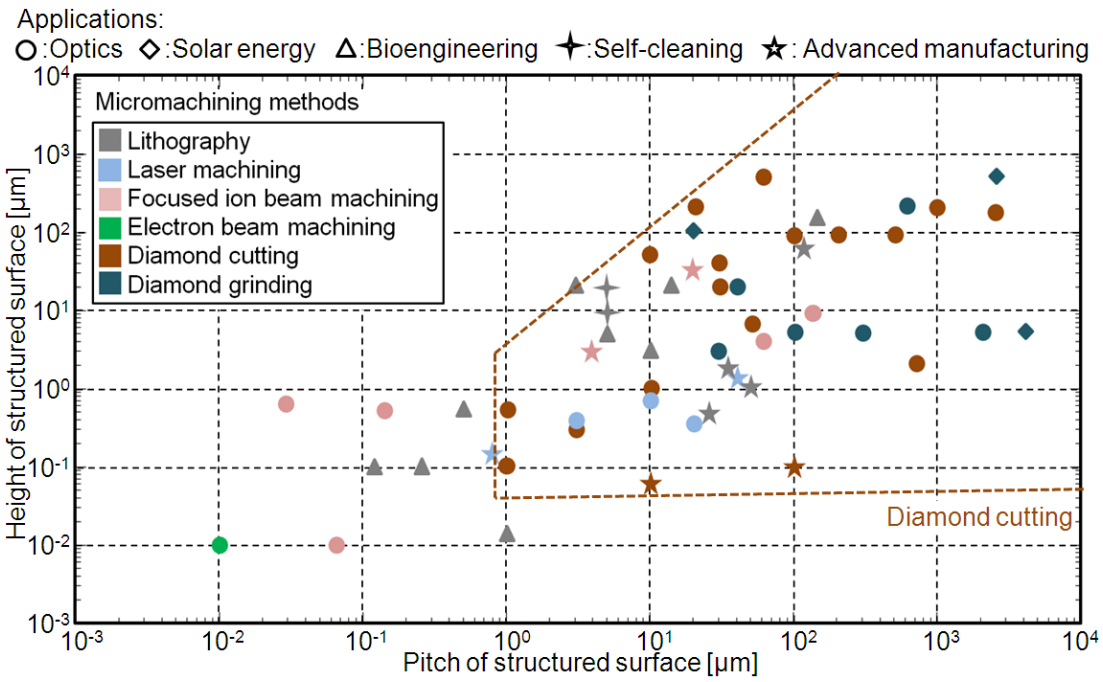

Fig. 1.2 Capability of micromachining methods for micro/nano structure fabrication

Lithography, focused ion beam machining and electron beam machining play a critical role in micro/nano-structure fabrication. These processes are advantageous to fabricate highly-dense micro/nano structures with a high aspect ratio and straight sidewalls. The feature size can be downscaled into tens of nanometers or even several single nanometers. However, these manufacturing technologies are not available for a large structure height of several hundred micrometers due to their low removal rate and time consuming nature. The machining efficiency is improved by applying laser machining, however it is difficult to fabricate highly-dense nanometer-scale structures due to the physical restriction in the minimum dimension of focused laser beam. Considering the mechanical micromachining technologies, micro grinding is not available for dense micro/nano structure fabrication due to the size restriction of grinding wheel, especially the radius of wheel tip. And also, it is difficult to fabricate sophisticated three-dimensional structures by applying the aforementioned processes. On the other hand, diamond cutting has a large dimension span in micro/nano structure fabrication, which is flexible and capable for many different designs. It also has a distinctive advantage of fabricating three-dimensional features and free-form sculptured

surfaces. Diamond cutting is superior to fabricate structures with a wide-ranged feature size from sub-microns up to more than several millimeters on non-ferrous materials, as shown in Fig. 1.2. The challenge of nanometer-scale structure fabrications and ferrous or brittle materials applications in diamond cutting will promote the diamond cutting technology more practical in the industrial applications.

Ultra-precision diamond cutting is usually applied to the fabrication of precision parts on plasitic materials, such as the soft metals including oxygen-free copper, brass, aluminum alloy, polymeric material such as PMMA, electroless nickel-phosphorus plating [53], and so on. As introduced at the beginning of this chapter, ultra-precision dies and molds made of hardened steel and tungsten carbide are greatly required for the mass production of functional elements with micro/nano structures, especially in optical industry. However, the conventional diamond cutting is not applicable directly to steel materials due to the extremely chemical tool wear [54]. Many researchers have dedicated to attain diamond machining of steel materials with suppressing tool wear propagation. For example, Casstevens [55] carried out a series of experiments under different gaseous atmospheres, e.g., inert atmosphere and carbon saturated atmosphere, and achieved significant tool wear reduction in a methane atmosphere. Evans [56] carried out cryogenic cutting by cooling the tool-workpiece system, which is advantageous for decreasing the chemical reactions between the iron in the workpiece and the carbon in the diamond tool. Brinksmeier et al. [57] developed a nitriding process based on workpiece modifications for avoiding chemical reactions between the diamond tool and the workpiece material. Song et al. [58] also applied an ultra-intermittent cutting method to reduce tool wear by decreasing the contact time between the diamond tool and the steel workpiece. However, none of these methods was found applicable to industrial applications. In addition, tungsten carbide is a typically hard and brittle material, and its ductile machining is extremely difficult by the conventional diamond cutting due to generations of brittle fracture on machined workpiece surface and excessive tool damage [59]. On the other hand, micro/nano structured components are mass-produced by glass molding and/or injection molding with complicated micro/nano structured molds/dies made of tungsten carbide and/or hardened steel. Although high

quality surface finish can be achieved by ultra-precision grinding method for those difficult-to-cut materials, it is extremely difficult to fabricate sophisticated micro/nano-scale structures especially with sharp edges. Hence, advanced diamond cutting technology is highly required for the micro/nano structure fabrication on tungsten carbide and hardened steel. For the last few decades, ultrasonic vibration cutting technology has been successfully applied to difficult-to-cut materials machining [60]. In particular, Shamoto and Moriwaki [61] proposed a new cutting method named as elliptical vibration cutting (EVC). The feasibility of steel material machining and tungsten carbide machining was verified by applying EVC with single crystal diamond (SCD) tools. Furthermore, Suzuki et al. [62] proposed a unique micro/nano sculpturing method by controlling the vibration amplitude in EVC. It is expected to enable highly-efficient fabrication of sophisticated micro/nano structures on hardened steel and tungsten carbide. The following Section 1.1.3 will introduce the elliptical vibration cutting technology in detail.

1.1.3 Linear vibration cutting and elliptical vibration cutting

Vibration assisted cutting (VAC) technique is an emerging cutting process that has been increasingly applied in the manufacturing industry since the 1960s [63]. In the early developing era of this technology, only vibration assisted machining with a linear vibration motion in the nominal cutting direction (or slightly inclined with respect to the nominal cutting direction) is commonly practiced by researchers. This type of VAC is named as “linear vibration cutting (LVC)”. The nominal cutting speed is set lower than the maximum tool vibration speed so that the tool can be separated from the workpiece in each vibration cycle. Figure 1.3 illustrates the process of LVC.

In the last three decades, LVC was successfully applied to various difficult-to-cut materials, such as ceramics [64], Inconel 718 [65], fused silica glass [66], soda-lime glass [67], stainless steel [68], tungsten carbide [69], and so on. The vibration of the cutting tool enhances entrance of the lubrication and/or reduces the friction on the rake face, which result in easier shear deformation in the cutting zone and reduction of chemical interactions between the diamond tool and the workpiece materials. As

compared with ordinary cutting (OC), LVC technology can lead into better cutting performances, such as smaller cutting forces [70], longer tool life [71], higher cutting stability [72], better surface finishing [68], and so on. It was also explored that SCD tools can be applied to LVC for precise machining of steel materials with roughness Rz of less than 0.1 μm at a cutting distance of 1600 m [68].

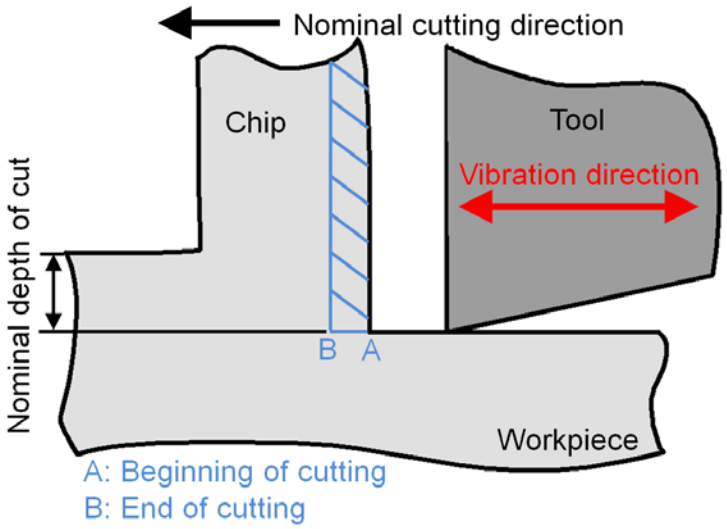

Fig. 1.3 Schematic illustration of linear vibration cutting process

In the LVC process, it should be noted that the actual vibration at the tool tip needs to be adjusted precisely so that the cutting edge does not interfere with the cut surface when it moves backward. Otherwise, the sharp and brittle cutting edge is easily chipped due to tensile stress generation at the flank face. In practical application, the LVC process causes vibration mark generation on the finished surface. This is because the tool vibration direction is inclined with respect to the nominal cutting direction to avoid the chipping occurrence. This roughness can be large in an ultra-precision level, and causes the deterioration of finished surface quality.

To overcome the aforementioned problems, a novel cutting technology named elliptical vibration cutting (EVC) [61] was first proposed in 1994 by Shamoto and Moriwaki. This technology has been the foreseen alternative to attain ultra-precision machining of difficult-to-cut materials in particular. Figure 1.4 shows the schematic illustration of the EVC process presented by Shamoto et al. [73, 74]. The cutting tool is

fed at a nominal cutting speed, and the tool tip is generally controlled to vibrate elliptically in the plane determined by the nominal cutting direction and the chip flow direction. As shown in Fig. 1.4, in each cycle of the elliptical vibration, the tool starts to cut the workpiece at time t_1, and then the workpiece material is removed in the form of a chip. After the tangential direction of the tool trajectory becomes parallel to the rake face, the cutting tool separates from the chip at t_5. The nominal cutting speed is set to be lower than the maximum vibration speed in the nominal cutting direction, ensuring that the tool is separated from the workpiece in each vibration cycle. When the tangential direction of the tool trajectory exceeds the shear direction of the material removing, the friction direction between the tool rake face and the chip is reversed as compared with that in the ordinary cutting process. This reverse of the friction leads to an increase in the nominal shear angle, resulting in significant decreases of the chip thickness and the average cutting forces [61, 73, 74]. Moreover, due to the separation in each vibration cycle, the contact surfaces of the cutting edge and the workpiece can be exposed into the surrounding gas and/or the cutting fluid, resulting in cooling of the tool and workpieces. This also allows suppression of adhesion and diffusion between the workpiece and the tool. As a result, the thermo-chemical wear can be supressed efficiently.

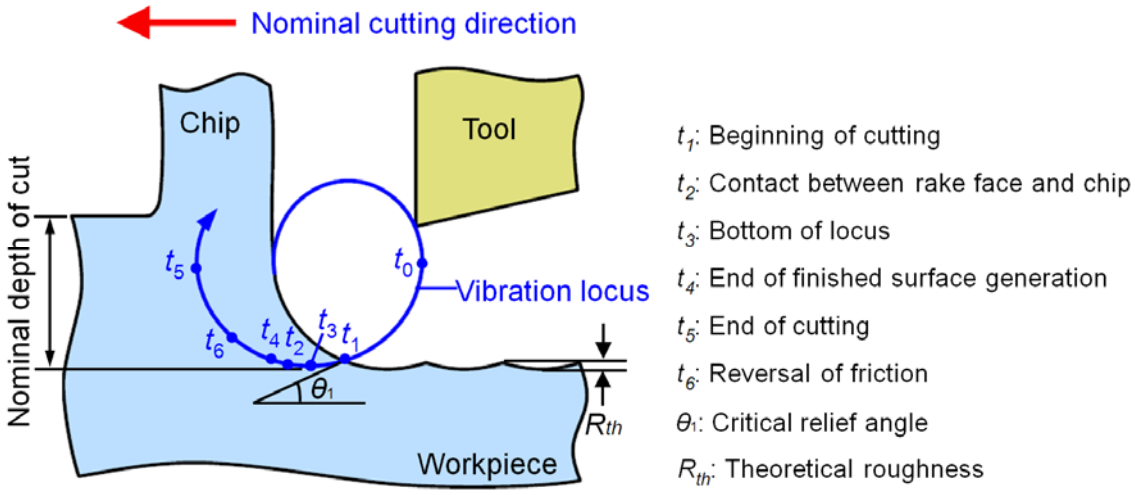

Fig. 1.4 Elliptical vibration cutting process [73, 74]

Some ultrasonic elliptical vibration tools [75, 76] have been developed so far, and their machining performance has been investigated for some difficult-to-cut materials machining. This technology is tested in industries mainly for ultra-precision diamond cutting of dies, molds, and optical parts. Through constant development in two decades, this novel method has been proved to be a promising method in terms of almost all cutting performances as compared with the OC and LVC methods in cutting various materials, especially difficult-to-cut materials. Ultra-precision machining of difficult-to-cut materials, such as hardened steel [77-80], tungsten alloy [81], sintered tungsten carbide [82-86] and other various materials [87], were realized by applying EVC technology. Suzuki et al. [78, 82] presented some experimental results when machining hardened steel and tungsten carbide by applying the EVC technology, as shown in Fig. 1.5. Especially in hardened steel machining, optical quality surfaces with maximum roughness of less than 0.05 μm Rz can be obtained up to a cutting distance of 2250 m by applying EVC [77].

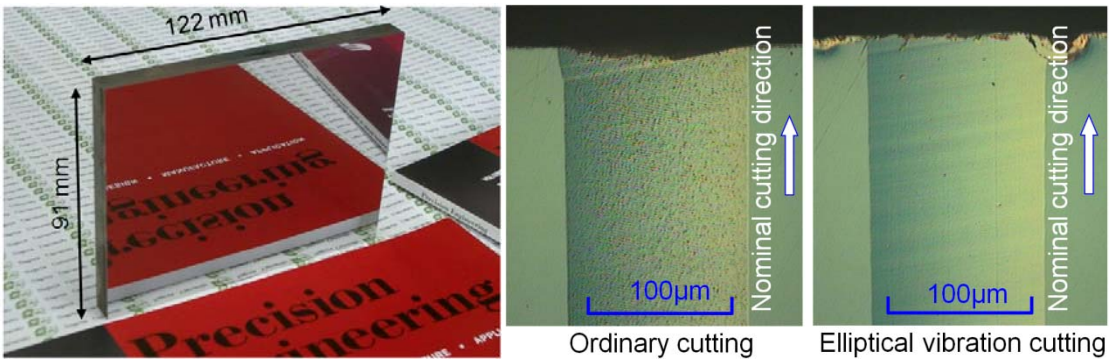

(a) Mirror surface of hardened steel (b) Tungsten carbide machining

Fig. 1.5 (a) Mirror surface obtained on hardened steel [78] and (b) tungsten carbide machining by applying ordinary cutting and elliptical vibration cutting [82]

With further development of the EVC process, Shamoto et al. [88] developed a three-degrees-of-freedom (3 DOF) ultrasonic vibration tool. It can generate an arbitrary ultrasonic elliptical vibration in the three-dimensional (3D) space so that it is suitable to machine 3D sculptured surfaces on difficult-to-cut materials.

Based on the successful cutting performance of EVC in practical applications, Suzuki et al. [62] explored further possibilities of functional surface machining on difficult-to-cut materials by applying EVC, and proposed a unique micro/nano sculpturing method, as shown in Fig. 1.6 (a). In this proposed method, vibration amplitude of the elliptical vibration is actively controlled while machining. Because of this amplitude control, the depth of cut can be changed rapidly without FTS but as being controlled by the conventional FTS technology. In other words, the EVC technology is already equipped with a FTS function by itself. Suzuki et al. [62] also presented several kinds of simple micro/nano textured patterns fabricated on hardened steel, as shown in Fig. 1.6 (b). Through primary experimental works, the feasibility of the proposed amplitude control sculpturing method was verified. Nowadays, EVC is attracting more and more attention due to its excellent machining performances.

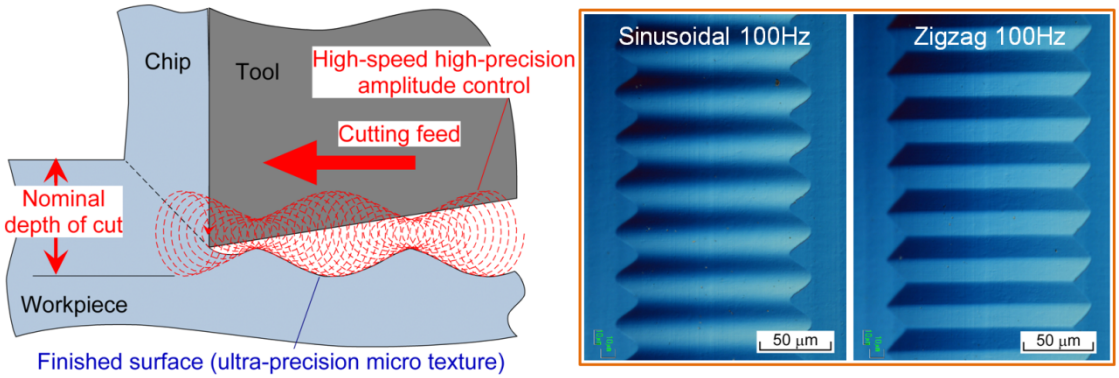

(a) Principle of amplitude control sculpturing method (b) Textured grooves on hardened steel

Fig. 1.6 (a) Amplitude control sculpturing method and (b) fabricated samples [62]

1.2 Motivation and objective

The proposed amplitude control sculpturing method in EVC has been expected to be one of the solutions to fabricate micro/nano structures on hardened steel and tungsten carbide in the molding industry. However, there are some challenges to apply the proposed sculpturing method to these difficult-to-cut materials in practice. The feasibility of hardened steel machining by applying EVC has been certified with detailed experimental investigations, however there is a lack of systematic studies on tungsten

carbide machining by applying EVC with single crystal diamond (SCD) tools.

Tungsten carbide is a crucial material for glass molding in optics manufacturing industry. As reviewed at the beginning of this chapter, sophisticated micro-nano structures have greatly applied into optics elements design in order to achieve advanced functions. Application of the proposed sculpturing method to tungsten carbide machining will be a notable step forward in molding industry. However, tungsten carbide is a typically hard and brittle material, and its ductile machining is extremely difficult due to brittle fracture generations in the workpiece and excessive tool damage. Even though the fundamental mechanism of tungsten carbide machining in ductile mode was clarified by applying EVC in the primitive researches, the tool damage is significantly excessive as compared with hardened steel machining and the cutting area is restricted to be extremely small. In order to improve the finished surface quality and increase the tool life, it is necessary to carry out more detailed investigations on the ductile machining of tungsten carbide by applying EVC. Moreover, it is also important to clarify the restrictions in machining parameters and cutting distance for ductile mode machining considering practical applications. Therefore, this study aims to fulfill the following systematic researches for tungsten carbide machining as a first step.

(1) Influence of process parameters

In the EVC process, several parameters, e.g., vibration amplitudes, nominal cutting speed and depth of cut, have significant influence on the cutting performance. In order to suppress the brittle defect generation and to increase the tool life, appropriate process conditions need to be clarified through experimental and theoretical investigations.

(2) Influence of material properties

Material researchers have been studying and developing the tungsten carbide material with better properties by modifying the material compositions and the grain size. They have significant influence not only on the mechanical and chemical properties but also on the machining performance of tungsten carbide.

Hence, it is necessary to clarify what kind of material is suitable to machine in high surface quality. In order to indicate the appropriate materials for industrial application, fundamental grooving investigations on tungsten carbide workpieces with different type of material properties are required.

(3) Feasibility study on micro/nano-structure machining

Feasibility of micro/nano structure machining by the proposed method has not been clarified so far. By applying the best combinations of the process parameters and the material properties investigated in the aforementioned researches, ultra-precision textured grooves and a dimple pattern may be fabricated in ductile mold.

(4) Comprehensive study on tool life and surface integrity for practical applications

A further research contribution to increase the tool life and improve the machined surface quality may be necessary to realize practical machining of tungsten carbide by applying the proposed sculpturing method in EVC. Hence, comprefensive study on the machining performances, i.e., tool life and the surface integrity deterioration, is conducted focusing on the following points:

(4-1) Grain size and binder material have a significant influence on the hardness and toughness of workpiece materials. Binder material may also have a chemical affinity to diamond. In order to clarify the influence of the material compositions and grain size on the tool wear progression, fundamental planing investigations on different workpiece materials are required.

(4-2) It is well-known that the crystal orientations often have a significant influence on life of the SCD tools. For further possibility of increasing the tool life, the influence of crystal orientation of SCD tools on the tool wear progression and the machined surface quality needs to be investigated.

(4-3) Due to the unique characteristics of EVC process, the actual cutting distance becomes much longer than the tool feed distance in one vibration

cycle. For better understanding of the process, the relationship between the tool wear and the actual cumulative cutting distance are investigated.

Based on the above-mentioned studies, prediction models of the tool wear, cutting force, and surface roughness are developed. Then, the machining performance may be predicted in advance by utilizing the proposed models. Hence, this study will give a basic guidance for selecting the appropriate cutting conditions in tungsten carbide machining.

The research outcomes in the the first research step may clarify the feasibility of micro/nano strucutures machining on tungsten carbide by the proposed method. However, we just can know the feasibility of micro/nano structures fabrication at this moment. There is a lack of knowledge about the restrictin on the machinable part geometry and machining accuracy by the proposed method in practice. As it is obviously difficult to machine steep downhill structures due to the flank face contact, this fact addresses not negligible restriction on the machinable part geometry. Systematic investigations on the micro/nano machining performance by the proposed amplitude control sculpturing method in EVC is important for applying the proposed method into practical applications. Hence, as a second step, analytical model to predict the restriction and machining accuracy is considered. This study aims to fulfill the following systematic researches. For simplification, hardened steel is adopted as the workpiece material. Note that hardened steel is also a typical difficult-to-cut material and our target material for micro/nano structure machining.

(1) Investigation on the restriction on the minimum machinable dimension

A variety of structures are required depending on the required functions as reviewed in Section 1.1, whose dimensions vary from several nanometers to hundreds of micrometers. In order to machine sophisticated fine structure, resolution of machinable structure geometry and its accuracy are important. As a primitive study on the machining performance of the proposed sculpturing

method, experimental investigations on the minimum machinable dimension are required.

(2) Kinematic study on the restriction in machinable part geometry

The proposed amplitude control sculpturing method imposes several restrictions in machinable part geometry, such as height variation range, curvature, and slope angle of the target part geometry. In order to clarify the restriction in machinable pert geometry, analytical model to predict the feasibility of functional surface machining in advance is required. This model is considered to be derived from the kinematic study on relative motion and geometries.

(3) Reference command compensation

There is one problem addressed in the past study [62]. The envelope of the cutting edge trajectory differs from the reference command shape due to the existence of finite amplitude in elliptical vibration. Although this difference leads machining error, it can be canceled by compensating the reference command. Therefore, a compensation method for the reference command needs to be developed.

(4) Experimental investigation of the machining feasibility

Finally, machining experiments of highly-accurate micro/nano structures, which can be applicable to practical use, need to be performed. Then, the feasibility of the proposed sculpturing method needs to be investigated.

1.3 Structure of thesis

This thesis consists of six chapters.

In Chapter 1, various applications of micro/nano structures are firstly introduced. Then a brief overview of the fabrication techniques is presented. In order to realize mass production of micro/nano structures, difficult-to-cut materials including hardened

steel and tungsten carbide are heavily demanded in manufacturing industry. The problems of micro/nano structure fabrication on these materials are described. Subsequently, the VAC technologies, especially the EVC technology, are presented. Finally, the motivation and research objectives are described. This section outlines the organization of this dissertation.

Chapter 2 presents the experimentally-investigated mechanism of ductile machining of tungsten carbide. A series of fundamental grooving tests are conducted firstly and the influences of vibration conditions and material compositions on surface integrity are investigated. A criterion is clarified to indicate how to obtain ductile machining. Based on these fundamental results, successful machining results of ultra-precision textured grooves and a dimple pattern are presented.

Chapter 3 carries out further contributions to increase the tool life in tungsten carbide machining by applying EVC. A series of planing tests are conducted to investigate the influences of material compositions, cumulative cutting distance and crystal orientations of SCD tools on the tool wear progression. By formulating the relations, the tool life and ductile machining conditions can be estimated in advance. The machining performance for each application is also roughly evaluated in advance.

Chapter 4 presents the analytical investigations on machinable part geometry and command compensation method in the proposed sculpturing method. According to the vibration conditions and the tool geometry, restrictions in machinable part geometry are clarified and formulated by considering the kinematic model of EVC. Then, mechanism of the machining error generation is expounded. Then, the compensation method of the vibration amplitude command for modifying the envelope shape of the vibration trajectory is presented, and its performance is verified through computational simulations.

Chapter 5 clarifies the highly-accurate micro/nano structure fabrication by experimental investigations. Machining accuracy of the proposed amplitude control sculpturing method is experimentally investigated. In what follows, the performance of the proposed command compensation method is experimentally evaluated and the machining error is efficiently suppressed. Moreover, the restriction in tool geometry and

the machinable part geometry is also experimentally verified comparing with the theoretical analyses. Finally, the proposed sculpturing method is applied to the machining applications of nano-textured grooves and a three-dimensional grid surface, which verifies the feasibility of efficient and accurate micro/nano machining by the proposed amplitude control sculpturing method.

Chapter 6 concludes the thesis with brief summary of the achieved results.

The structure of the thesis is summarized in Fig. 1.7.

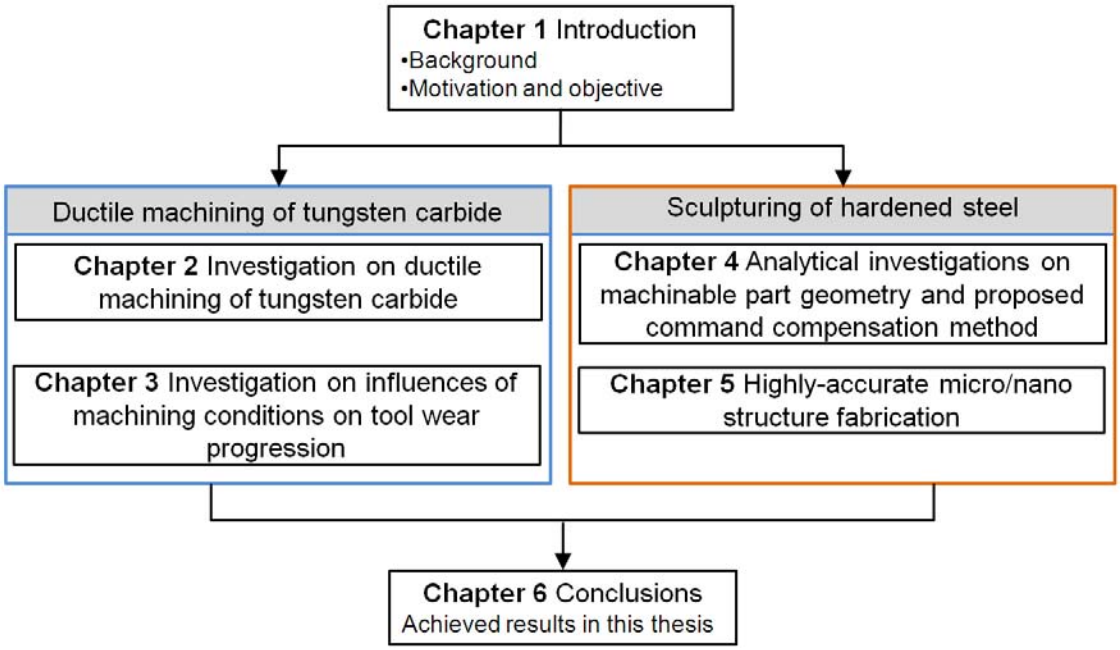

Fig. 1.7 Flow chart of this study

Chapter 2

Investigation on ductile machining of tungsten carbide

2.1 Introduction

With the rapidly developing of optoelectronics industry, demand for advanced manufacturing technology for sophisticated micro/nano structures on optical systems is increasing drastically. For example, glass lenses with small radius and large curvature have been used in various devices to miniaturize their structures and/or to attain large storage capacity. Some micro/nano optical gratings have been used in optical communication equipments, encoders, and digital cameras. In order to realize mass production of those glass devices, tungsten carbide is heavily used in the molding industry because of its unique mechanical, thermal and chemical properties. Ultra-precision diamond cutting equipped with fast tool servo has been generally applied to fabricate sophisticated micro/nano structures, and it has been widely used especially for a variety of plastic molding applications. However, application of ultra-precision diamond cutting to brittle materials is limited. Since tungsten carbide is a typically hard and brittle material, its ductile machining is extremely difficult by the ordinary ultra-precision cutting technology due to generations of brittle fracture in the workpiece and excessive tool damage. In contrast to cutting, ultra-precision grinding is applicable to ductile mode machining of tungsten carbide [8, 50, 51, 89-91]. Suzuki et al. [92, 93] additionally reported that following lapping and/or polishing are also effective to achieve higher quality surface finish. However it is extremely difficult to fabricate sophisticated micro/nano-scale structures especially with sharp edges by these methods. These facts impose significant restrictions in practical use of tungsten carbide and define the bottleneck of ultra-precision machining of tungsten carbide. In the last few decades, ultrasonic vibration cutting technology has been successfully applied to difficult-to-cut materials machining. In particular, elliptical vibration cutting technology has been the foreseen alternative to attain ultra-precision machining of hard/brittle

materials.

Suzuki et al. [82] have applied the elliptical vibration cutting technology to machining of tungsten carbide with Cobalt binder, and its ductile machining has been attained successfully by applying single crystal diamond tools. This former work also captured the following nature of the process. In the elliptical vibration cutting, the instantaneous uncut chip thickness in each vibration cycle becomes significantly small especially when the tool cuts the finished surface around the bottom of the elliptical vibration. Because of this process, the actual depth of cut may become smaller than the critical value for ductile machining. This fact also indicates that the selection of the appropriate parameters for the elliptical vibration cutting process, i.e., vibration amplitudes, nominal cutting speed and depth of cut, is very important to attain ductile mode machining. In the previous research, the influences of cutting/vibration conditions on the surface quality were roughly studied. However, evaluated conditions are limited and thus the most appropriate parameters for ductile mode cutting cannot be determined. Meanwhile, a systematic study to identify the most appropriate parameters is required. As the maximum instantaneous uncut chip thickness (MIUCT) while cutting the finished surface is considered to be directly associated with the surface deterioration, a key parameter, MIUCT, is proposed in the present research. With MIUCT derived from the cutting and vibration conditions, a criterion of ductile to brittle transition may be modeled.

In addition, the machined surfaces were mainly evaluated by use of optical micro scopes in the former researches. Due to the insufficient resolution, it is difficult to detect the tiny defects with a size of less than several hundred nanometers, which is almost identical to the grain size in the latest material technology. Consequently, the surface deterioration was only defined considering the multi-grain-size defects, i.e., drop off of massive grains together from the workpiece surface. In the present research, machined surfaces are investigated by means of a scanning electron microscope (SEM), which has a better resolution as compared with the optical micro scope.

Recently, tungsten carbide material has been studied and developed with better properties by modifying the material compositions and the grain size. Material property

affects machining characteristics of tungsten carbide significantly at the same time. For instance, material strength depends on the grain size and binder material, which may have chemical affinity to the diamond. The material strength and the chemical affinity have major influence on tool wear. Nevertheless, few researchers have investigated the influence of material composition on the ultra-precision machining of sintered tungsten carbide so far. Hence, further study on tungsten carbide machining considering material technology may lead to further advance in the machining performance.

In this chapter, a series of fundamental grooving tests are conducted. Through analytical and experimental investigations, the influence of binder material composition, grain size of tungsten carbide, cutting and vibration conditions on the machining performances are studied in elliptical vibration cutting of tungsten carbide. A criterion is clarified for indicating how to achieve ductile machining of tungsten carbide by applying elliptical vibration cutting technology. Based on the fundamental findings, feasibility of ultra-precision machining of tungsten carbide with micro/nano-scale structures, i.e., textured grooves and a dimple pattern, are explored. The main research outcomes presented in this chapter are also presented in the author's published papers [94-96].

2.2 Experimental conditions and experimental setup

Eight kinds of workpieces with different binder materials and grain size are prepared for experimental investigations. The material properties including catalog values of hardness and elastic modulus are listed in Table 2.1.

Table 2.1: Types of tungsten carbide materials used in grooving experiments.

No.	Average grain size [μm]	Binder phase	Hardness [GPa]	Elastic Modulus [GPa]
BL1	0.3	Binderless	25.48	675
BL2	0.5	Binderless	23.52	680
BL3	1.3-1.5	Binderless	19.60	650
BL4	0.3	Binderless	25.98	680
Co1	0.5	Co(≤10%wt)	19.60	560
Co2	1.3-1.5	Co(≤10%wt)	13.72	560
Co3	0.5	Co(12%wt)	17.30	580
Ni1	0.5	Ni(≤10%wt)	16.66	510

Before the machining experiments, all workpieces are ground to make flat surfaces. Note that the subsurface damage has significant influence on the machining performance of tungsten carbide. Therefore, lapping with fine diamond abrasives with a mean size of 0.25 μm is followed to make a flat mirror surface and to remove subsurface damage from the workpiece surfaces. Grooving experiments are performed on an ultra-precision machine tool ASP01UPX made by Nachi-Fujikoshi Corp., as shown in Fig. 2.1. A positioning resolution of linear axes is 1 nm.

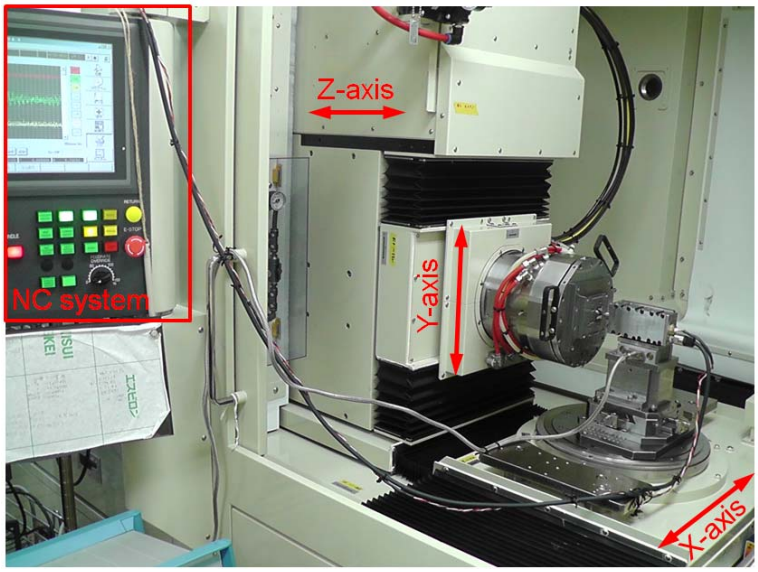

Fig. 2.1 Ultra-precision machine tool ASP01UPX made by Nachi-Fujikoshi

The elliptical vibrator, which can generate an arbitrary elliptical vibration at a frequency of about 36.2 kHz, was attached to the X axis table. Figure 2.2 illustrates the elliptical vibrator and its control system for the elliptical vibration cutting. It was designed as a two-degree-of-freedom (2-DOF) elliptical vibrator. The vibrator can be actuated by exciting PZT actuators that are sandwiched with metal cylindrical parts. Since the vibrator is designed to have the same resonant frequencies in the second resonant mode of longitudinal vibration and the fifth resonant mode of bending vibration, it can generate large longitudinal and bending vibrations simultaneously at the same ultrasonic frequency by exciting the actuators. As a result, a 2-DOF elliptical vibration

can conveniently be obtained at the diamond tool tip. Mean-to-peak vibration amplitudes can be adjusted arbitrary within 2 $\mu m_{0\text{-}p}$ by controlling the amplifier gains as shown in Fig. 2.2. The tool used in grooving experiments is a single crystal diamond (SCD) tool with a nose radius of 1 mm, a clearance angle of 10 deg and a negative rake angle of -20 deg.

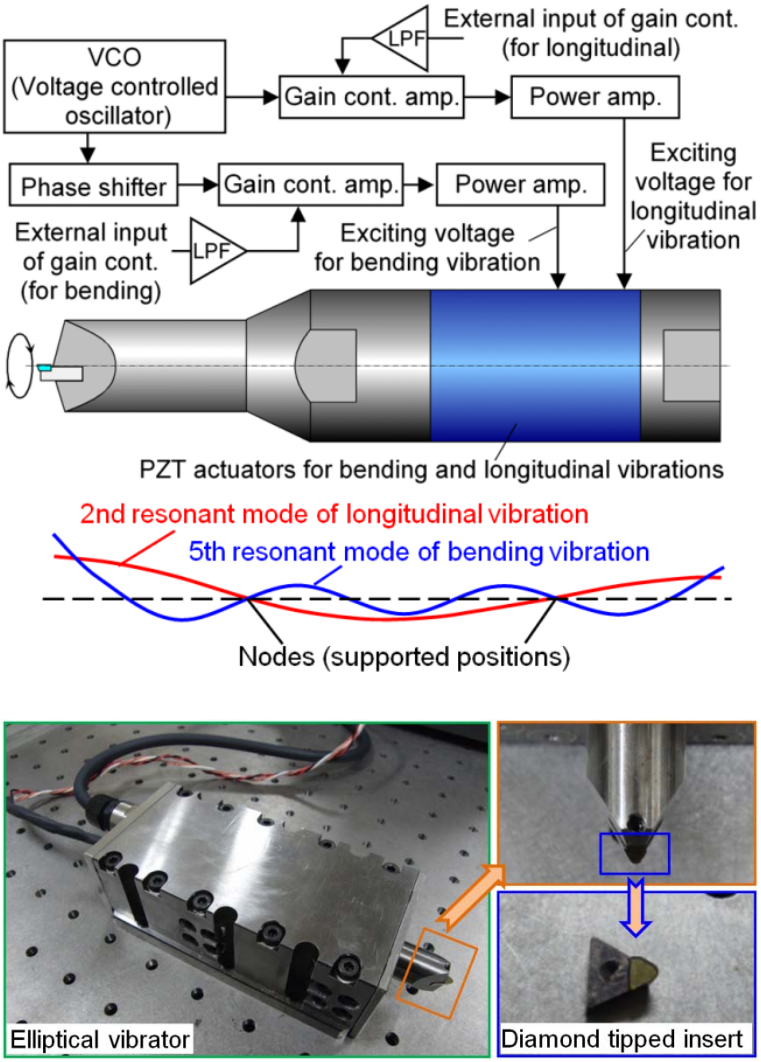

Fig. 2.2 2-DOF elliptical vibration tool

Figure 2.3 shows the experimental setup. In order to investigate the influence of the depth of cut on the machined surface quality, the cutting feed is controlled by the synchronized motion of the X axis table and the Z axis table. The depth of cut was

linearly increased in grooving experiments, as illustrated in Fig. 2.3. Experimental conditions are summarized in Table 2.2.

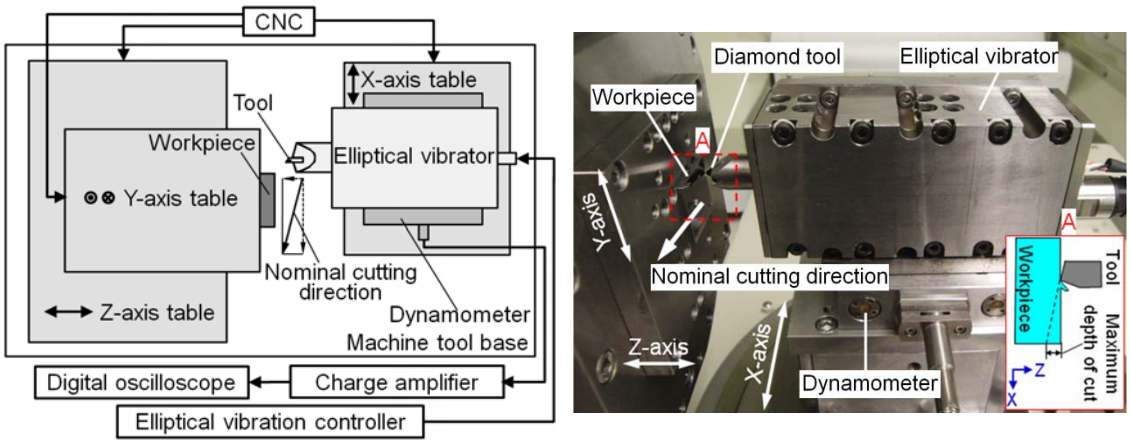

Fig. 2.3 Illustration and picture of experimental setup for grooving

Table 2.2: Experimental conditions in grooving experiments

Elliptical vibration conditions	Frequency [kHz]	36.2
	Amplitude in nominal cutting direction [$\mu m_{0\text{-}p}$]	1-2
	Amplitude in depth of cut direction [$\mu m_{0\text{-}p}$]	0.5-2
	Phase shift [deg]	90
Cutting conditions	Depth of cut [μm]	0- maximum 2
	Nominal cutting speed [mm/min]	137.5-1100
	Cutting fluid (oil moistening)	Bluebe LB-10

Before the experiments, the vibration amplitudes along nominal cutting and depth of cut directions are measured by using the orthogonally-aligned laser doppler vibrometer. Amplitudes of the vibration can be obtained in both directions simultaneously. Then the elliptical vibration locus can be plotted as a Lissajous curve. For example, when the mean-to-peak amplitudes of elliptical vibration in nominal cutting and depth of cut directions are set to be 2 $\mu m_{0\text{-}p}$ and 1 $\mu m_{0\text{-}p}$, respectively, and a phase difference is 90 deg, then the measurement locus is shown in Fig. 2.4.

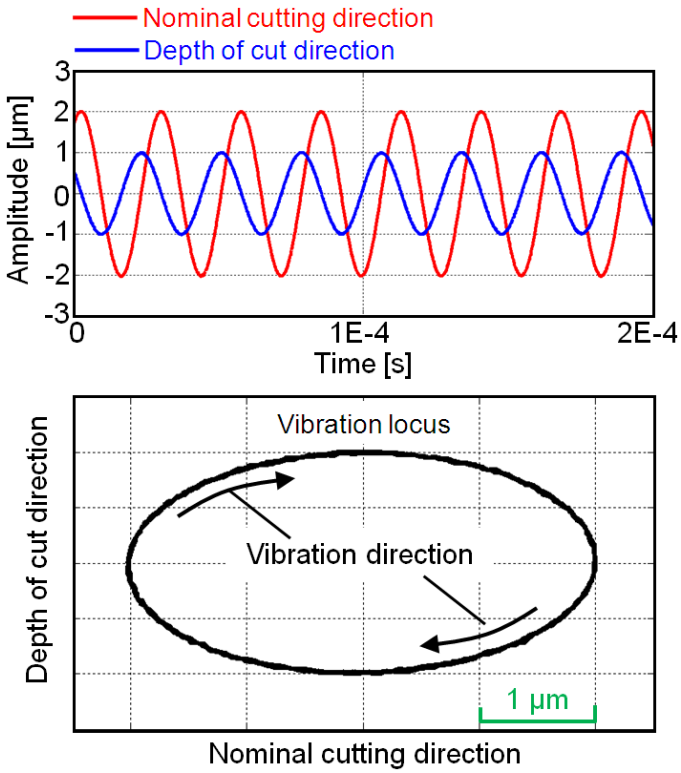

Fig. 2.4 Measured vibration locus (A_c-A_d: 2-1 $\mu m_{0\text{-}p}$)

2.3 Fundamental grooving experiments

2.3.1 Comparison of elliptical vibration cutting with ordinary cutting

At first, investigations are undertaken to compare elliptical vibration cutting performance against ordinary cutting. The binderless workpiece of BL4 is grooved by ordinary cutting and the elliptical vibration cutting. Figure 2.5 shows the scanning electron microscope (SEM) images of the grooved surface on BL4 at a depth of cut of 0.2 μm. In this experiment, the nominal cutting speed is set to 150 mm/min. Mean-to-peak amplitudes of elliptical vibration in nominal cutting and depth of cut directions A_c and A_d are set to 2 $\mu m_{0\text{-}p}$ and 1 $\mu m_{0\text{-}p}$ to realize an elliptical vibration locus. As noted from Fig. 2.5, the groove formed by the ordinary cutting is filled with numerous brittle fractures. In contrast, a smooth surface can be obtained by the elliptical vibration cutting. As any brittle cracks and asperities can't be observed on the surface in the elliptical vibration cutting, ductile mode machining was attained successfully. From this fact, it can be expected that the inside of tungsten carbide grains existing at the topmost layer of the remained surface was cut without fracture generation on the surface or

pull-out of the grains, which are observed in the ordinary cutting.

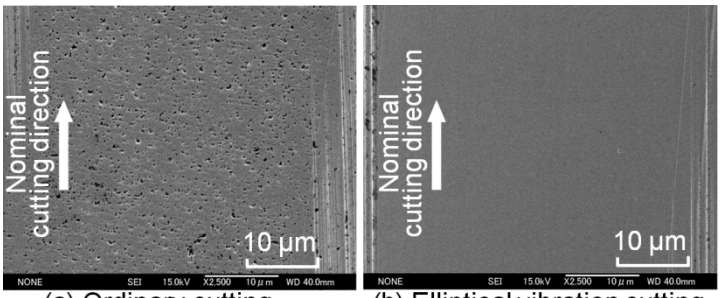

(a) Ordinary cutting (b) Elliptical vibration cutting

Fig. 2.5 SEM images of grooved surface (workpiece: BL4, depth of cut: 0.2 μm, nominal cutting speed: 150 mm/min, A_c-A_d: 2-1 $\mu m_{0\text{-}p}$)

Next, Fig. 2.6 shows the cutting edges after grooving of the binder-containing workpiece, Co1.

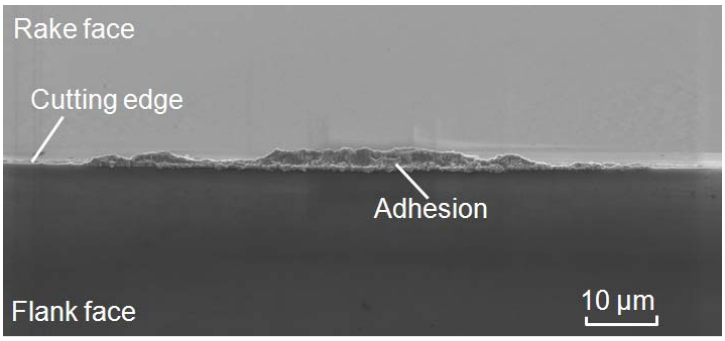

(a) Ordinary cutting

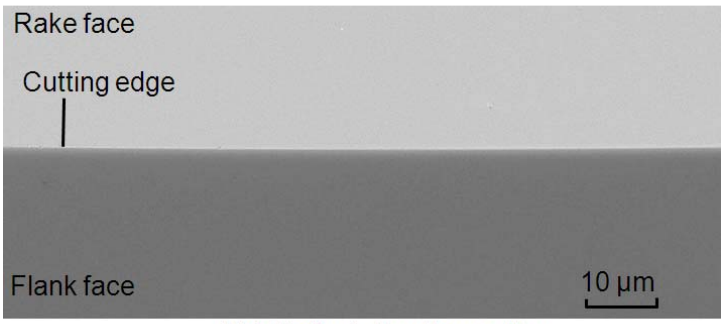

(b) Elliptical vibration cutting

Fig. 2.6 Cutting edges after grooving (workpiece: Co1)

Considerable adhesion of the workpiece material can be observed on the rake face of the tool used in ordinary cutting, which may result in adhesion wear and/or considerable thermo-chemical reaction. The same phenomena was observed in the

ordinary cutting of other binder-containing materials. On the other hand, any adhesion was not observed in the elliptical vibration cutting. This fact indicates that the elliptical vibration cutting may be effective to suppress tool wear progress and to attain better surface quality in machining of binder-containing tungsten carbide as well as steel materials.

Mechanism of the ductile mode machining is considered as follows. In elliptical vibration cutting, the tool cuts the surface that is finished in the previous vibration cycle. Thus, the actual uncut chip, i.e., instantaneous uncut chip thickness as shown in Fig. 2.7, becomes extremely thin.

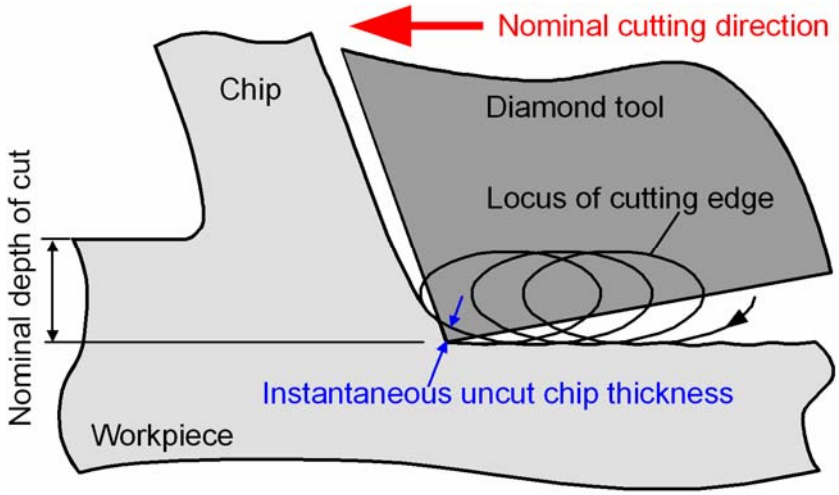

Fig. 2.7 Elliptical vibration cutting with thin instantaneous uncut chip thickness

Note that this uncut chip thickness becomes generally smaller as compared with the nominal depth of cut. In other words, the process is similar to that of milling. This instantaneous uncut chip thickness in each vibration cycle becomes significantly small especially when the tool cuts the finished surface around the bottom of the elliptical vibration. Because of this process, the actual depth of cut becomes smaller than the critical value for ductile machining due to the size effect in fracture toughness, resulting in significant improvement of nominal critical depth of cut for ductile machining of tungsten carbide. The process is similar to that in milling, and Arif et al. [97] clarified similar improvement in milling process through experiments with the PCD tool.

2.3.2 Influence of cutting parameters on surface quality

In this section, the influence of several cutting parameters, i.e., vibration amplitudes, depth of cut, and nominal cutting speed, on the surface quality is investigated in an empirical manner. Firstly, fundamental micro grooving experiments were carried out under several conditions. Figure 2.8 demonstrates the surface quality of micro grooves machined on Co1 where the nominal cutting speed and mean-to-peak vibration amplitudes in the nominal cutting and depth of cut directions, A_c and A_d, are changed. The speed ratio, i.e., the ratio of the maximum vibration speeds in the nominal cutting direction to the nominal cutting speed, is kept to be a constant value of 25.

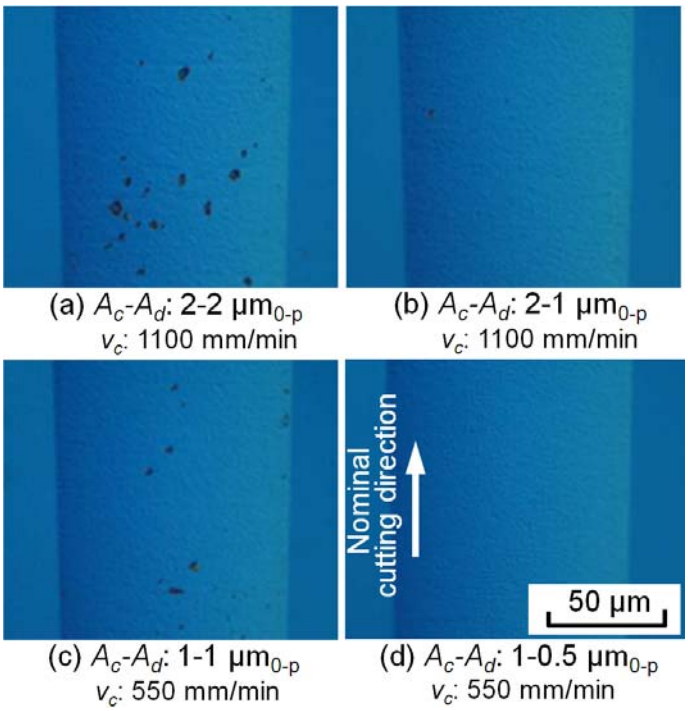

Fig. 2.8 Influence of vibration amplitude on surface quality (workpiece: Co1, depth of cut: 0.9 μm, mean-to-peak amplitudes in nominal cutting and depth of cut directions: A_c-A_d μm$_{0\text{-p}}$, nominal cutting speed: v_c mm/min)

The grooved surfaces at the vibration amplitudes A_c-A_d of 2-2 μm$_{0\text{-p}}$ and 1-1 μm$_{0\text{-p}}$ are filled with micrometer-scale brittle cracks, as shown in Fig. 2.8. The defect size is several times larger than the single grain size of 0.5 μm. Thus, these defects are

considered to be due to the pull-out of agglomerated tungsten carbide grains from the workpiece surface. On the other hand, similar large defects do not generate at vibration amplitudes of 2-1 and 1-0.5 $\mu m_{0\text{-}p}$. Similar experimental results were also observed in case of other binder-containing and binderless materials and hence it can be concluded that the influence of vibration amplitudes on ductile machining is not negligible.

The influence of the depth of cut on the surface quality was also investigated. Figure 2.9 demonstrates a groove surface of BL4, which was machined with a circular vibration (1 $\mu m_{0\text{-}p}$) at a cutting speed of 150 mm/min. The depth of cut is gradually increased from 0 μm to 2 μm. Surface quality changes depending on the depth of cut, where brittle cracks can generate at a large depth of cut even in the elliptical vibration cutting. Transition border from ductile to brittle modes are observed at the depth of cut of about 1.5 μm. Agglomerated grains seem to be pulled out at one time from the surface, and this feature of the defects is the same as that shown in Fig. 2.8. This kind of defect characterized by their size is defined as “multi-grain-size defect” in the present research. Note that similar surface deterioration with large defects is not observed in ordinary cutting. Hence, this is considered to be a specific problem in elliptical vibration cutting.

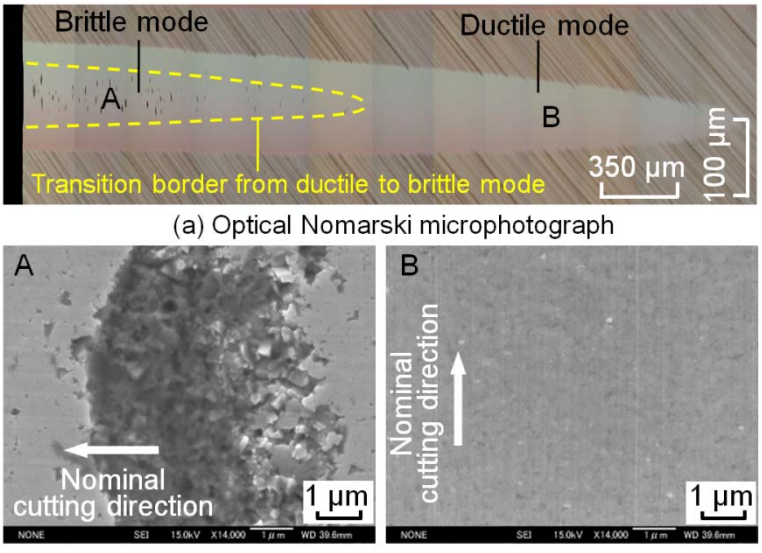

(a) Optical Nomarski microphotograph

(b) SEM image of position A (c) SEM image of position B

Fig. 2.9 Machined groove with the increasing of depth of cut

These amplitude and depth of cut dependencies are considered to be related to the chip pulling-up-motion in the elliptical vibration cutting. Figure 2.10 shows schematic illustrations of the elliptical vibration cutting process with different vibration amplitudes. When the vibration amplitude is larger in depth of cut direction, chip pulling-up-distance in this direction becomes longer. In addition, the chip pulling-up-distance increases up to about mean-to-peak amplitude when the depth of cut is large. Sintered materials are not tough against tensile stress. Because of this nature, massive grains may be pulled out from the workpiece surface by the pulling-up-motion especially when upward motion distance in depth of cut direction is longer than the grain size. When the ratio of amplitude in the depth of cut direction to that in the nominal cutting direction is large, slope of the cutting edge trajectory becomes steep while pulling up the chip. This steep trajectory is also considered to enhance the above-mentioned pull-out phenomena. Hence, the vibration amplitudes and the depth of cut need to be selected properly to avoid the “multi-grain-size defect” occurrence due to the pull-out of massive grains.

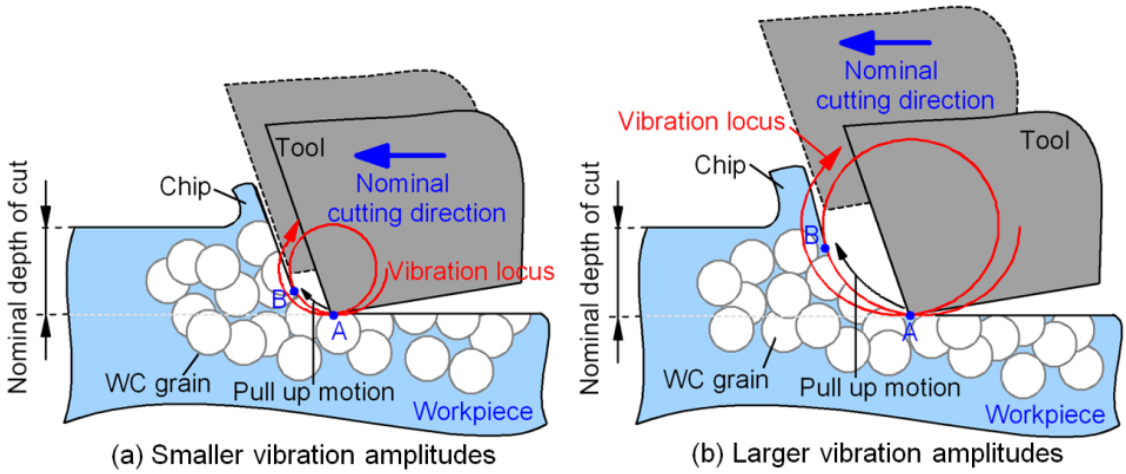

Fig. 2.10 Pull up motion with different vibration amplitudes

The influence of the nominal cutting speed on the surface quality is also examined by conducting several grooving experiments. SEM images of the machined surfaces of BL1 at a depth of cut of 0.5 μm are shown in Fig. 2.11. It is confirmed that higher quality surfaces in the ductile mode can be attained at lower nominal cutting speed. On the contrary, poor surfaces with a number of defects were observed distinctively at higher

nominal cutting speed. The defect size is less than several hundred nanometers, which is almost identical to the grain size. Experiments performed on other workpieces indicated a similar tendency. To differentiate from “multi-grain-size defect”, this kind of defect is defined as “single-grain-size defect” in the present research. This cutting-speed dependency of surface quality is considered to be associated with the cut volume in each vibration cycle. It should be noted that the instantaneous uncut chip thickness is almost proportional to the nominal cutting speed. Thus, the cutting forces decrease and the strain energy at the deformed zone is reduced when the nominal cutting speed decreases. Small force and strain energy are beneficial to suppress crack propagations while machining. Hence, the selection of the cutting speed condition is significantly important to suppress “single-grain-size defect” occurrence.

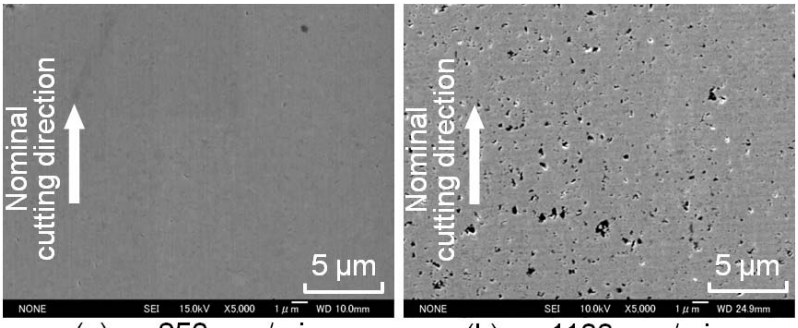

(a) v_c: 250 mm/min (b) v_c: 1100 mm/min

Fig. 2.11 Effect of nominal cutting speed on surface quality (workpiece: BL1, amplitudes: 2-1 $\mu m_{0\text{-}p}$, depth of cut: 0.5 μm).

2.3.3 Influence of material compositions on surface quality

Material compositions and the grain size have a significant influence on the material properties, e.g., hardness, abrasive resistance, fracture toughness, ability of chemical reactions, and so on. For example, Jia and Fischer [98] conducted a series of scratch tests of tungsten carbide with cobalt binder by means of a modified Vickers hardness tester, where significant advantage of small-sized grain in abrasion resistance was clarified. Paul et al. reported significance of chemical aspect of tool wear in cutting with SCD tools. Saito et al. [99] studied the influences of cobalt content and grain size

on the wear resistance of tungsten carbide against carbon steel in their abrasion experiments, where the wear rate increased with cobalt content and grain size of tungsten carbide. Krakhmalev et al. [100] also studied abrasion wear process of tungsten carbide against silicon carbide abrasive. Ren et al. [101] investigated influence of grain size and cobalt binder on grinding process. In the other hand, few researchers have investigated the influence of material composition on the ultra-precision machining of sintered tungsten carbide so far.

In this section, further study on tungsten carbide machining with considering material technology is carried out to evaluate influence of material composition on machining performance in detail by applying elliptical vibration cutting. Grooving experiments are conducted on tungsten carbide with different binder content and grain sizes, such as BL1, Co1, BL2, BL3 and Co2. SEM images of grooved surfaces of BL1 and Co1 are shown in Fig. 2.12. As noted, brittle fractures are not observed from the machined surfaces. This also indicates that ductile mode machining is realized at a large depth of cut of 0.9 μm. However, ductile machining was not realized by the same cutting conditions in BL2, BL3 and Co2 even when the depth of cut is smaller. This can be validated from Fig. 2.13. Their surfaces are filled with the “single-grain-size defects” due to brittle fracture, which were observed in the high-cutting-speed machining experiment.

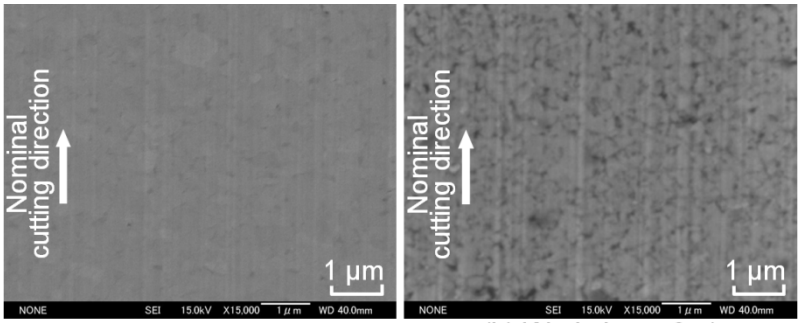

(a) Workpiece: BL1 (b) Workpiece: Co1

Fig. 2.12 SEM micrographs of machined groove surface (depth of cut: 0.9 μm, vibration amplitudes: 1-0.5 $\mu m_{0\text{-}p}$, nominal cutting speed: 137.5 mm/min)

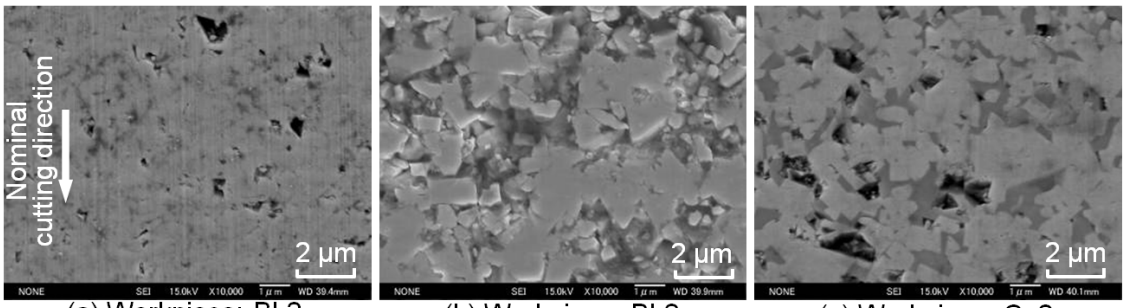

(a) Workpiece: BL2 (b) Workpiece: BL3 (c) Workpiece: Co2

Fig. 2.13 Brittle fracture of machined groove surface (depth of cut: 0.2 μm, vibration amplitudes: 1-0.5 $\mu m_{0\text{-}p}$, nominal cutting speed: 137.5 mm/min)

Comparing the grooving results of BL1, BL2 and BL3, the difference in surface integrity indicates that smaller grain size is advantageous to attain ductile mode machining. It is known that sintered materials consisting of smaller particles generally have better crack resistance due to smaller initial defect size inside the material, as reported by Fang and Eason [102]. Because of this nature, finer grain is advantageous not only to increase the toughness of the material but also to realize ductile mode machining. Comparing the grooving results of Co1 and BL2, it is apparent that the binder phase is also advantageous to suppress the generation of brittle fracture. The defect size is, therefore, smaller in Co2 than that in BL3, where the grain sizes are the same. The same advantage in fracture suppression was also confirmed in Ni1.

2.3.4 Clarify a criterion for ductile machining of tungsten carbide

Through the grooving experiments, we found that single-grain-size defects can be generated much more easily as compared to multi-grain-size defects. Therefore, it is important to select appropriate process conditions focusing upon suppression of the single-grain-size defect generation. In order to evaluate the relative difference in surface deterioration due to single-grain-size defects, the machined surface quality was classified into nine levels and a scale from 0 to 8 are provided by the authors based on optical microscope observation. 0 represents the best surface with minimal defects and 8 is associated with the worst surface finish. Yan et al. [103] developed the similar method to evaluate surface integrity of silicon carbide machined by SCD tools.

Unlike SEM observation, single-grain-size defects are simply observed as asperities or hazes by means of an optical microscope due to insufficient resolution. However, it is considered to be available to evaluate an extent of single-grain-size defects from the observed optical images. In the present study, machined surfaces are observed by the optical microscope. Then, optical micrographs of the machined surfaces with a size of 250 x 250 pixels were processed using the data processing software, MATLAB. One pixel size is 0.18 μm x 0.18 μm. As the defect area becomes darker than the smooth area without defects, darker portion is identified as the defect surface. By counting the total number of pixels identified as defect, the scores of machined surfaces are evaluated, which is summarized in Table 2.3. For instance, the high quality surfaces of BL1 and Co1 shown in Fig. 2.12 are indexed as 0 and 1 where no single-grain-size defect is observed. As compared with Co1, the score of the machined surface of BL1 is judged as 0 because of the smoother surface. Scores of machined surfaces of BL2, BL3 and Co2 in Fig. 2.13 are evaluated as 5, 8, and 6 due to the single-grain-size defect. This quantification process might be influenced by threshold in data processing, but relative difference in the evaluation results seem to be mostly reliable.

Table 2.3: Definition of machined surface score

Number of pixels regarded as defect	Score
0	0,1
1-50	2
51-100	3
101-500	4
501-1000	5
1001-1500	6
1501-2000	7
2001-4000	8

As mentioned above, surface deterioration due to single-grain-size defects may depend on the instantaneous uncut chip thickness in elliptical vibration cutting process. In particular, the maximum instantaneous uncut chip thickness (MIUCT) while cutting

the finished surface is considered to be directly associated with surface deterioration. Figure 2.14 illustrates the tool trajectory around the bottom and theoretical MIUCT at the i-th vibration cycle. By considering the kinematic model of elliptical vibration cutting, Table 2.4 summarizes the MIUCT values in the grooving experiments.

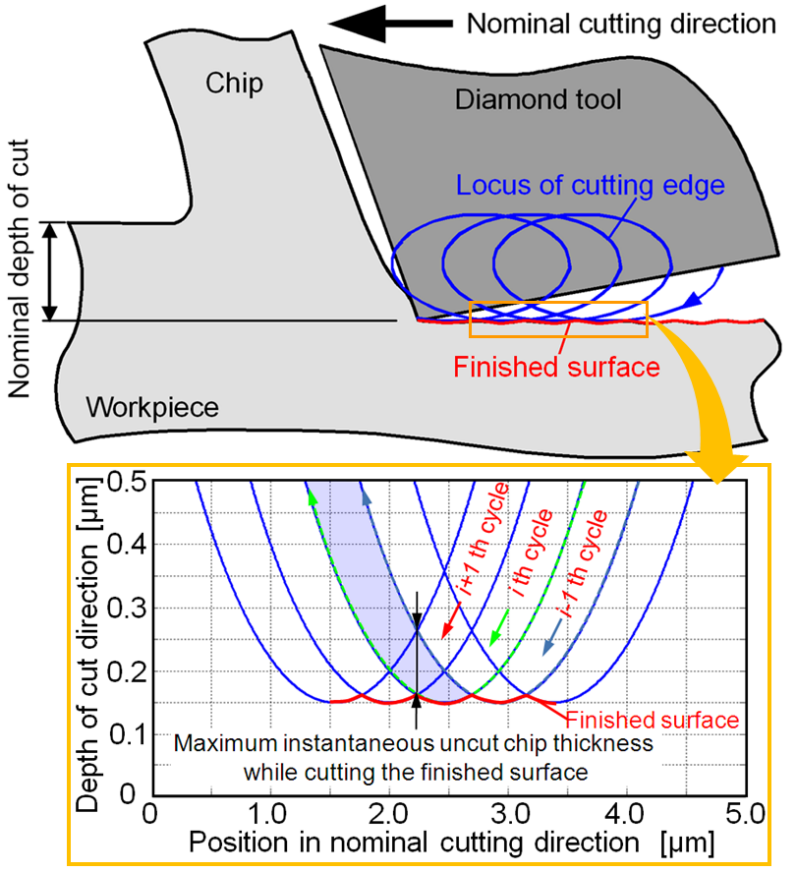

Fig. 2.14 Maximum instantaneous uncut chip thickness while cutting finished surface

Table 2.4: Values of maximum instantaneous uncut chip thickness (MIUCT) in grooving experiments [nm]

		Vibration amplitudes in nominal cutting/depth of cut directions [$\mu m_{0\text{-}p}$]				
		2/2	2/1	2/0.5	1/1	1/0.5
Nominal cutting speed [mm/min]	137.5	2	1	0.5	4	2
	275	8	4	2	16	8
	550	32	16	8	62	31
	1100	124	62	31	--	--

Figure 2.15 indicates relations of surface quality score and the maximum instantaneous uncut chip thickness (MIUCT) for all evaluated materials in grooving. The values of surface quality index increase with an increase of MIUCT regardless of the workpiece material. Hence, the MIUCT needs to be decreased to achieve better surface quality. High quality surfaces in ductile mode, whose score is 0 or 1, are obtained when the MIUCT is less than or equal to 4 nm and the workpieces are BL1, BL4, Co1, Co3, and Ni1. In other words, ductile machining cannot be attained for Co2, BL2 and BL3 under all evaluated conditions. These facts indicate that appropriate vibration amplitude and cutting speed conditions need to be selected to satisfy a small MIUCT, which is less than or equal to 4 nm. The grain size also needs to be less than or equal to 0.5 μm and binder material is helpful to attain ductile mode machining. The feature of multi-grain-size defect occurrence is almost the same as that of the single-grain-size defect occurrence on the machined surface.

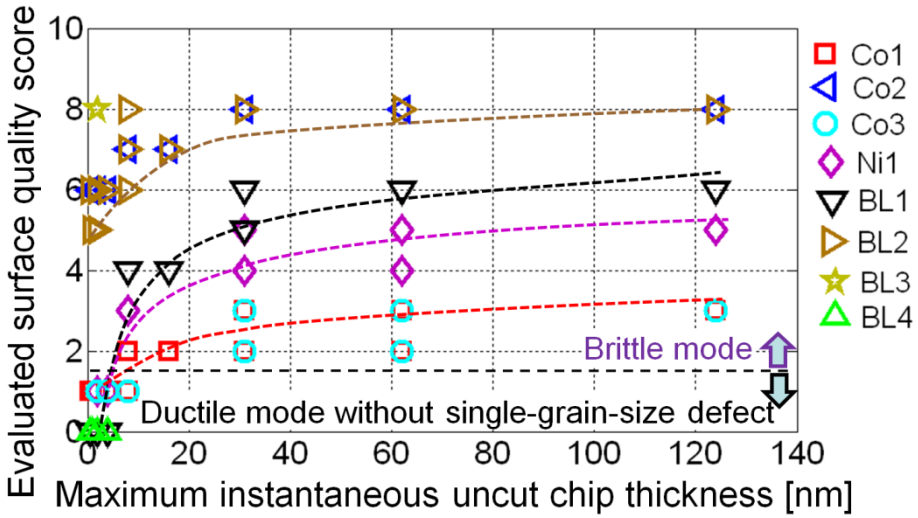

Fig. 2.15 Influence of maximum instantaneous uncut chip thickness on surface quality (evaluated at a depth of cut of about 1 μm)

2.4 Feasibility of micro/nano structure machining

The above critical findings in grooving investigations are utilized to ductile machining tungsten carbide. For instance, binderless tungsten carbide with the grain size of 0.3 μm and binder-containing tungsten carbide with the grain size of 0.5 μm

showed the excellent machinability in ductile mode. Therefore, BL4 and Co3 were used in this section. The feasibility of micro/nano-scale structures fabrication is investigated by applying elliptical vibration cutting.

In order to investigate feasibility of micro structure fabrication with shape edges, V-grooves machining experiments were conducted on Co3 using V-shaped diamond tool. Two V-shaped grooves with a depth of 20 μm were cut, where the depth of the groove was increased by cumulating the grooving with a depth of cut of 0.5 μm 40 times. A constant nominal cutting speed of 250 mm/min was applied. A V-shaped single crystal diamond tool with a nose radius of less than 0.5 μm, an included angle of 90 deg, a rake angle of -20 deg and a clearance angle of 10 deg, was used. The nominal cutting distance in the whole machining process is about 0.8 m. As shown in Fig. 2.16, V-grooved surface with sharp edges can be obtained with no considerable defect generation by applying elliptical vibration cutting. However, V-grooved surface formed by the ordinary cutting is filled with numerous brittle fractures. Hence, ultra-precision machining of sintered tungsten carbide is not feasible by means of the ordinary cutting technology.

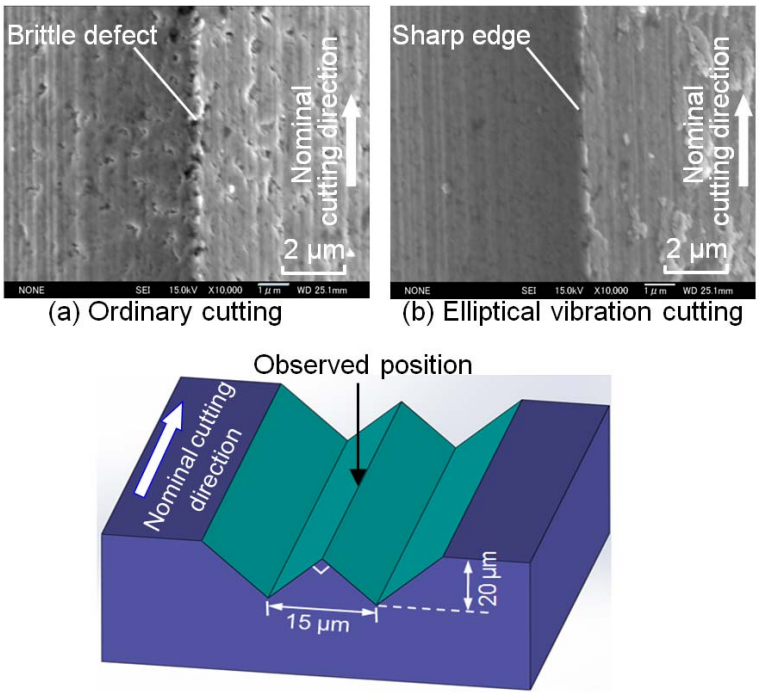

Fig. 2.16 V-grooved surface with sharp edge fabricated by elliptical vibration cutting

The microphotographs of the cutting edges after the V-shape grooving experiments are shown in Fig. 2.17. Similar with the grooving result in Section 2.3.1, no adhesion and no serious tool wear can be observed in the elliptical vibration cutting.

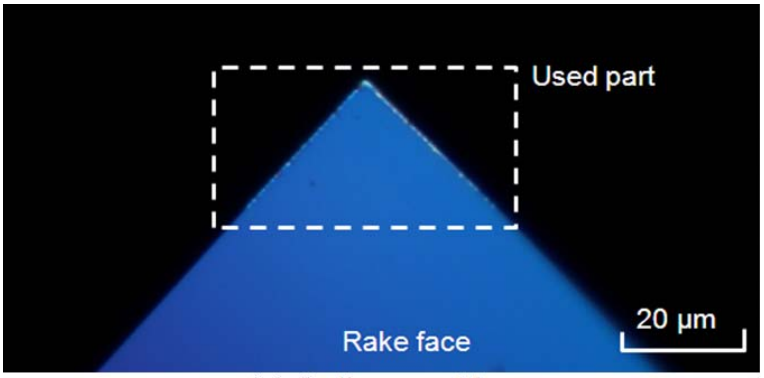

(a) Ordinary cutting

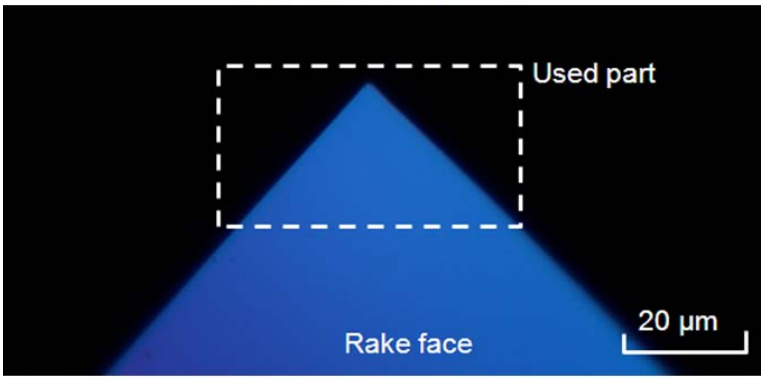

(b) Elliptical vibration cutting

Fig. 2.17 Microphotographs of V-shaped tool edge in different cutting methods

In the following section, the feasibility of micro/nano-scale sculpturing is clarified through micro-textured grooving and nano-dimple pattern machining experiments. The amplitude control sculpturing method is applied, where the depth of cut is regulated by controlling the vibration amplitude in the depth of cut direction during machining. Figure 2.18 shows a principle of the sculpturing method by utilizing the elliptical vibration cutting [62]. The envelope of the cutting edge trajectory is transferred to the machined surface, resulting in sculpturing of micro structures on the workpiece. In this section, BL4 and Co3 were used for the textured grooving and the dimple machining,

respectively. The experimental conditions and cutting parameter selections are presented in Table 2.5.

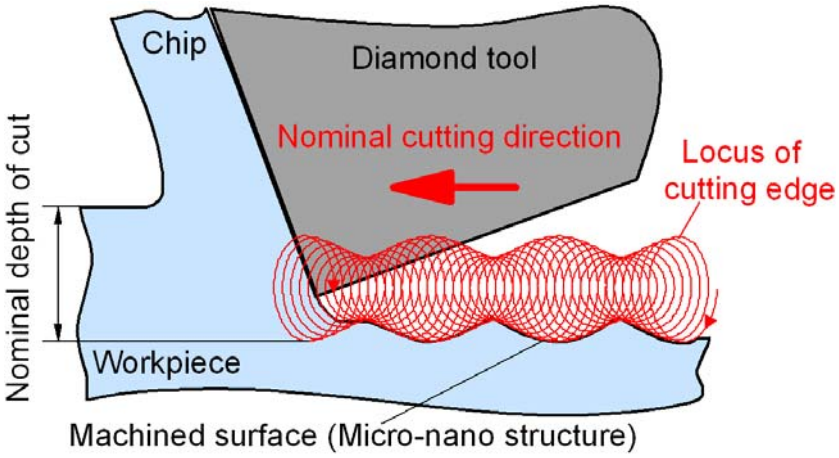

Fig. 2.18 Principle of micro/nano structures sculpturing [62]

Table 2.5: Experimental conditions for sculpturing of micro/nano structures

Conditions		A	B
Cutting conditions	Nominal cutting speed [mm/min]	150	284
	Pick feed [μm]	--	100
	Maximum depth of cut [μm]	1.2	0.2
Vibration conditions	Frequency of elliptical vibration [kHz]	36.2	36.2
	Frequency of amplitude oscillation [Hz]	42-84	60
	Amplitude in depth of cut direction [$\mu m_{0\text{-}p}$]	0.5-1	0.5-1
	Amplitude in nominal cutting direction [$\mu m_{0\text{-}p}$]	2	2
Tool	Nose radius [mm]	1.0	1.0
	Rake angle [deg]	-20	-20
	Clearance angle[deg]	10	10
Workpiece	Material	BL4	Co3

Textured grooves with three kinds of patterns, i.e., sinusoidal, zigzag and ramp waves, were machined under Condition A. Figure 2.19 shows the microphotographs of micro textured grooves and the measured surface profile along the nominal cutting direction. Amplitude of these wave commands was set to be about 0.5 μm. The profiles of the textured grooves were measured by an optical surface profiler (ZYGO NewView6200). The experimental results indicated that the grooves with ultra-precision nano textures can be machined successfully in ductile mode on tungsten carbide, and a

defect-free smooth surface can be obtained by the elliptical vibration cutting. Due to the restriction in dynamic response of vibration amplitude control, some corners cannot be machined sharply. Therefore, they are machined with slight roundness, and the peak-to-valley of sculpturing structures becomes relatively smaller than that of 0.530 μm in sinusoidal textured grooving.

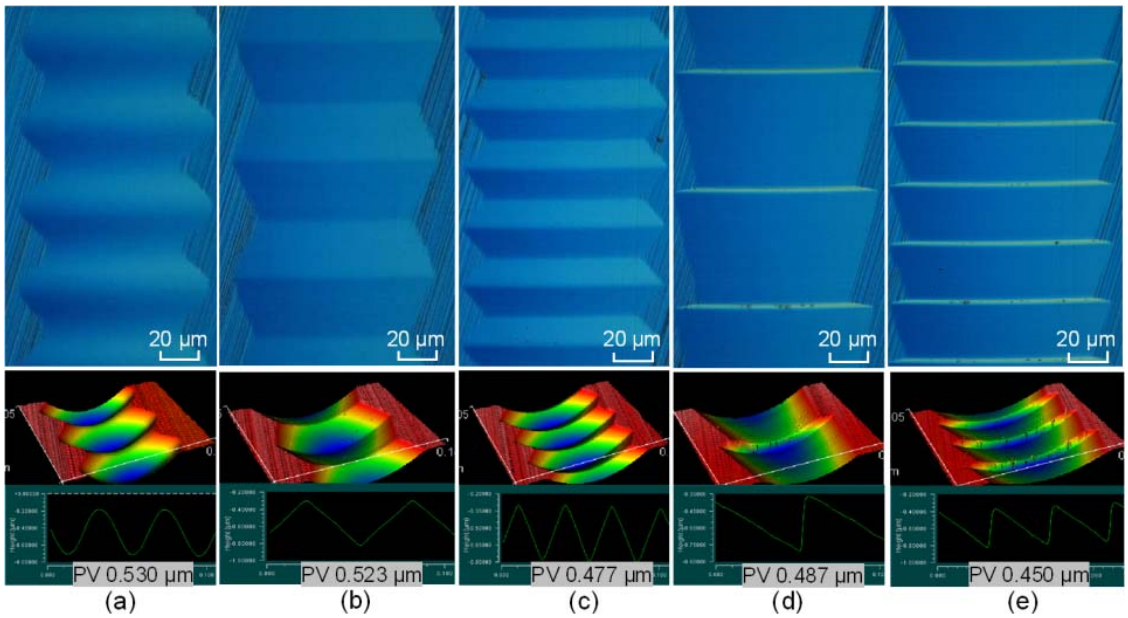

Fig. 2.19 Microphotographs of textured grooves: (a) sinusoidal (60 Hz), (b) ramp (42 Hz), (c) ramp (84 Hz), (d) zigzag (42 Hz) and (e) zigzag (84 Hz)

Figure 2.20 shows the photograph of dimples sculptured under Condition B and measured profiles. In this machining, the mean-to-peak amplitude in the depth of cut direction is controlled by sinusoidal wave pattern, which is changed from 0.5 $\mu m_{0\text{-}p}$ to 1 $\mu m_{0\text{-}p}$. The maximum depth of cut is, however, set to be about 0.2 μm, which is less than half the amplitude variation of 0.5 μm. Consequently, independent concave dimples with a maximum depth of about 0.2 μm were machined successfully in ductile mode on tungsten carbide. Note that these nano sculpturings cannot be attained by ordinary machining methods.

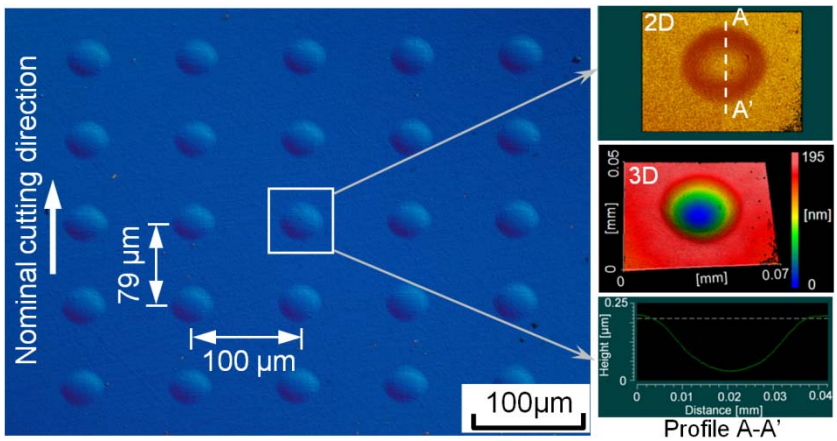

Fig. 2.20 Microphotograph of fabricated dimple structures and their measured profiles

2.5 Summary

Based on the grooving investigations, it is confirmed that practical ultra-precision machining of sintered tungsten carbide is not feasible by means of the ordinary cutting. However, elliptical vibration cutting can be used successfully to realize ductile mode machining. This chapter summarizes the appropriate conditions to efficiently apply elliptical vibration cutting to ductile machining tungsten carbide. The machinability of tungsten carbide depends on its grain size and binder phase. In order to attain better surface quality, smaller grain size and presence of the binder phase are advantageous to prevent fracture generation. In addition, the ductile mode machining can be realized when the maximum instantaneous uncut chip thickness (MIUCT) while cutting the finished surface is less than or equal to 4 nm. MIUCT is determined by vibration amplitude and cutting speed, hence those conditions are significantly important to realize defect-free ductile mode machining. Based on the aforementioned findings in the fundamental grooving experiments, nano-scale sculpturing of textured grooves and a dimple pattern were challenged. Experimental results verified the feasibility of practical ultra-precision machining of tungsten carbide in ductile mode by applying the elliptical vibration cutting technology.

Chapter 3

Investigation on influences of machining conditions on tool wear progression

3.1 Introduction

In Chapter 2, it was studied and clarified that elliptical vibration cutting (EVC) technology can be successfully applied to tungsten carbide machining in ductile mode. Application of the proposed amplitude control sculpturing method to tungsten carbide machining will be a notable step forward in molding industry. However, tungsten carbide is a typically hard and brittle material, therefore the surface quality is extremely deteriarated due to the excessive tool damage. Suzuki et al. [82, 83] indicated that the single crystal diamond (SCD) tool damage in tungsten carbide machining has been significant unlike hardened steel machining by applying EVC, and the cutting area was restricted to be extremely small. Moreover, Nath et al. [84] also carried out several experimental investigations on elliptical vibration cutting of sintered tungsten carbide, where machinability of tungsten carbide by using polycrystalline diamond (PCD) tools was investigated. Following this, the influence of the cutting parameters and tool radius on machined surface quality was further investigated [85]. Consequently, Nath et al. [86] concluded that restriction in the cutting area is improved successfully by using PCD tools and a surface with roughness of less than 30 nm Ra was attained at the beginning of cutting. However, surface roughness deteriorates significantly, which may not be acceptable in optical elements manufacturing. This fact indicates that further research contribution to extend the tool life of SCD is necessary to realize practical machining of tungsten carbide by applying the EVC technology.

As introduced in Chapter 2, material technology of tungsten carbide has been developed with better properties by modifying the material compositions and the grain size. Material property affects machining characteristics significantly. Further study on

tungsten carbide machining considering material technology may lead to significant tool life increase. Furthermore, the actual cutting distance in one vibration cycle becomes much longer than tool feed distance due to the unique elliptical vibration cutting process. It is assumed that the tool damage may be related to this cumulative cutting distance rather than the nominal cutting distance in the EVC. Moreover, Yuan et al. [104] indicated the combination of crystal planes had an important influence on SCD tool wear. Uddin et al. [105] confirmed that the orientations of diamond tool have significant effects on the tool wear propagation when precision cutting silicon. Zong et al. [106, 107] also achieved a conclusion that SCD tool with the crystal orientation of (100) in flank face and (110) in rake face can provide with the most excellent wear resistance by theoretical analyses and silicon cutting experiments. Therefore, it may be one of the practical and effective solutions to suppress the tool wear by adopting the optimum combination of crystal orientations in rake and flank faces in tungsten carbide machining by applying EVC technique.

In order to investigate the possibility to increase the tool life in tungsten carbide machining, comprehensive studies are carried out in this chapter. First of all, a series of fundamental planing tests are conducted on tungsten carbide materials with different binder content and grain sizes. The influence of material composition on the machining performance is investigated. In this research step, the mechanism of tool wear propagation and chip generation is also clarified in detail. And then, due to the specific cutting process of elliptical vibration cutting, the actual cutting distance in one vibration cycle becomes much longer than the tool feed distance in one vibration cycle. So, the influence of cumulative cutting distance on cutting performance is following studied. Finally, due to the strength of the cutting edge is directly associated with the crystal orientation of diamond material, the influence of crystal orientation of diamond tool on cutting performance is also clarified with a series of planing tests. The research outcomes presented in this chapter are also presented in the author's published papers [94-96].

3.2 Experimental conditions and experimental setup

Four kinds of workpieces with different binder materials and grain size are prepared for experimental investigations in planing. The material properties including catalog values of hardness and elastic modulus are listed in Table 3.1.

Table 3.1: Tungsten carbide materials used in planing experiments

No.	Average grain size [μm]	Binder phase	Hardness [GPa]	Elastic Modulus [GPa]
BL1	0.3	Binderless	25.48	675
BL2	0.5	Binderless	23.52	680
Co1	0.5	Co(≤10%wt)	19.60	560
Ni1	0.5	Ni(≤10%wt)	16.66	510

All of these workpieces are grounded and then lapped with fine abrasives to make a flat mirror surface and to remove the subsurface damage from the workpiece surfaces. SCD tools with a nose radius of 1 mm, a clearance angle of 10 deg and a negative rake angle of -20 deg are used in the planing experiemtns. The crystal orientation of the flank face is set to be (100), while that of the rake face is set to be (100) or (110). Those combinations are denoted as R(100)F(100) and R(110)F(100) in this chapter, where 'R' and 'F' represent the rake face and the flank face, respectively. Zong et al. [107] presented the detailed orientation combination of diamond tools, as shown in Fig. 3.1.

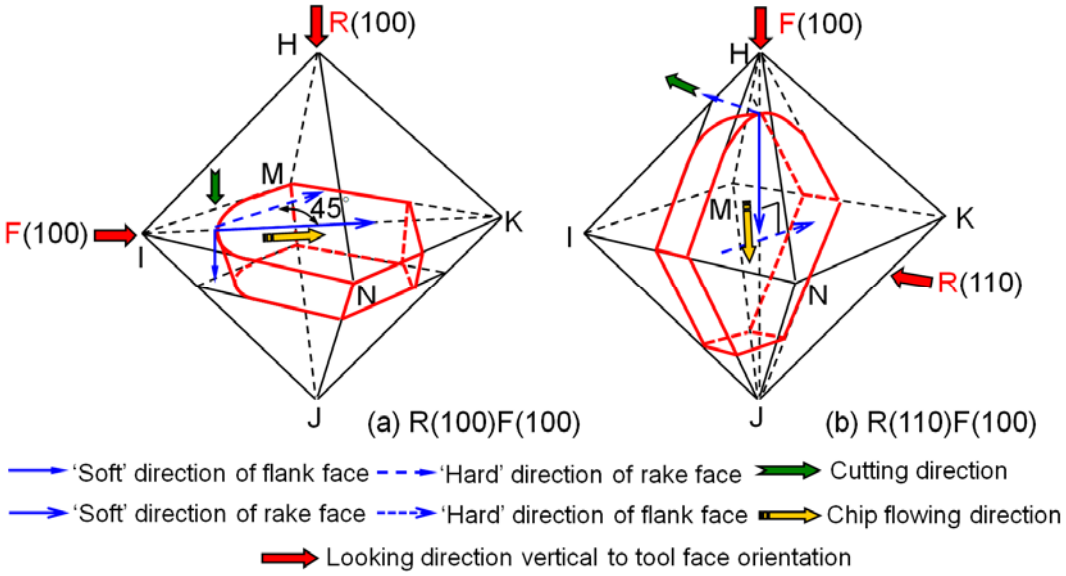

Fig. 3.1 Orientation combinations of single crystal diamond tool (a) R(1 0 0)F(1 0 0) and (b) R(1 1 0)F(1 0 0) [107]

Fig. 3.2 presents the experimental setup in planing experiments. It is similar to the experimental setup used in grooving experiments as introduced in Chapter 2. All experiments are performed on the ultra-precision machine tool ASP01UPX with a positioning resolution of 1 nm. The 2-DOF elliptical vibrator, which can generate arbitrary elliptical vibration at a frequency of about 36.2 kHz, was attached to the X axis table. The cutting feed and the pick feed are controlled by the motion of the X axis table and the Y axis table respectively. The depth of cut was linearly increased in each stroke, as illustrated in Fig. 3.2. Experimental conditions are summarized in Table 3.2.

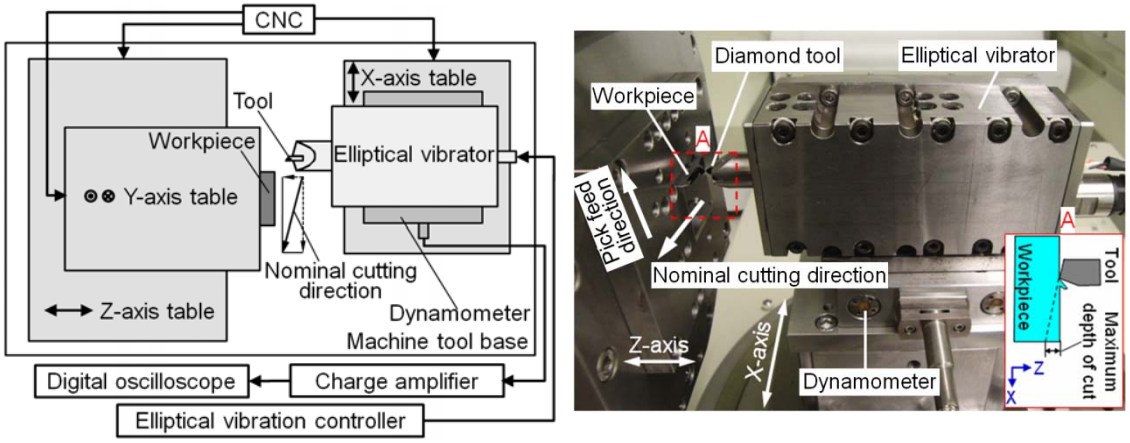

Fig. 3.2 Illustration and picture of experimental setup for planing

Table 3.2: Experimental conditions for planing experiments

Elliptical vibration conditions	Frequency [kHz]	36.2
	Amplitude in nominal cutting direction [$\mu m_{0\text{-}p}$]	2
	Amplitude in depth of cut direction [$\mu m_{0\text{-}p}$]	1
	Phase shift [deg]	90
Cutting conditions	Depth of cut [μm]	0- maximum 1.2
	Nominal cutting speed [mm/min]	125-1000
	Pick feed [μm]	5
	Cutting fluid (oil moistening)	Bluebe LB-10

3.3 Investigations on tool wear progression and machined surface quality

3.3.1 Influence of material compositions

In order to investigate the influence of binder material and grain size on the tool wear progression and the machined surface quality, planing of BL1, BL2, Co1 and Ni1 were conducted. Based on the grooving results in Chapter 2, amplitudes A_c-A_d of 2-1 $\mu m_{0\text{-}p}$ and a nominal cutting speed of 250 mm/min were adopted in following planing experiments. The depth of cut was linearly increased from 0 μm to the maximum 1.2 μm along the nominal cutting direction in each cutting pass. Figure 3.3 shows microphotographs of machined surfaces of BL1 and BL2 at a depth of cut of 1 μm. The nominal cutting distance is about 0.2 m, thus the cutting edge is considered to be still sharp and the influence of tool wear is negligible. The nominal cutting distance denotes the cumulative distance of the tool feed while machining. The pictures indicate that the surface quality in planing is identical to that in grooving introduced in Chapter 2.

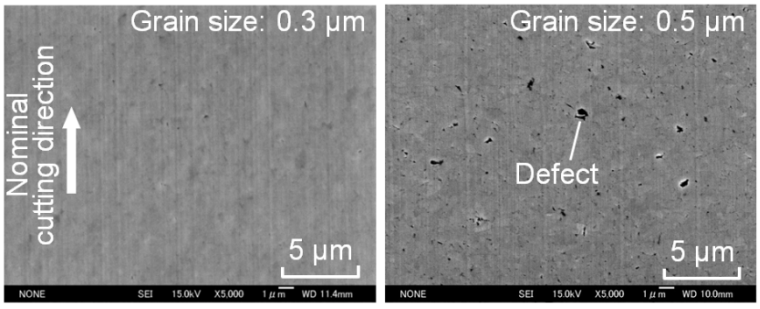

(a) Workpiece: BL1 (b) Workpiece: BL2

Fig. 3.3 Difference of surface qualities of BL1 and BL2 (depth of cut: 1 μm, nominal cutting distance: 0.2 m).

The microphotographs of the cutting edges after the planing experiments are shown in Fig. 3.4. The nominal cutting distance is about 4 m for all of the planing experiments. As also observed from the microphotographs, submicron-size chippings can be detected on the rake faces. On the other hand, excessive tool wear with a number of scratch marks is observed on the flank faces. Tool damage extents in BL1, Co1, and Ni1 seem to be almost the same, while that in BL2 is relatively small.

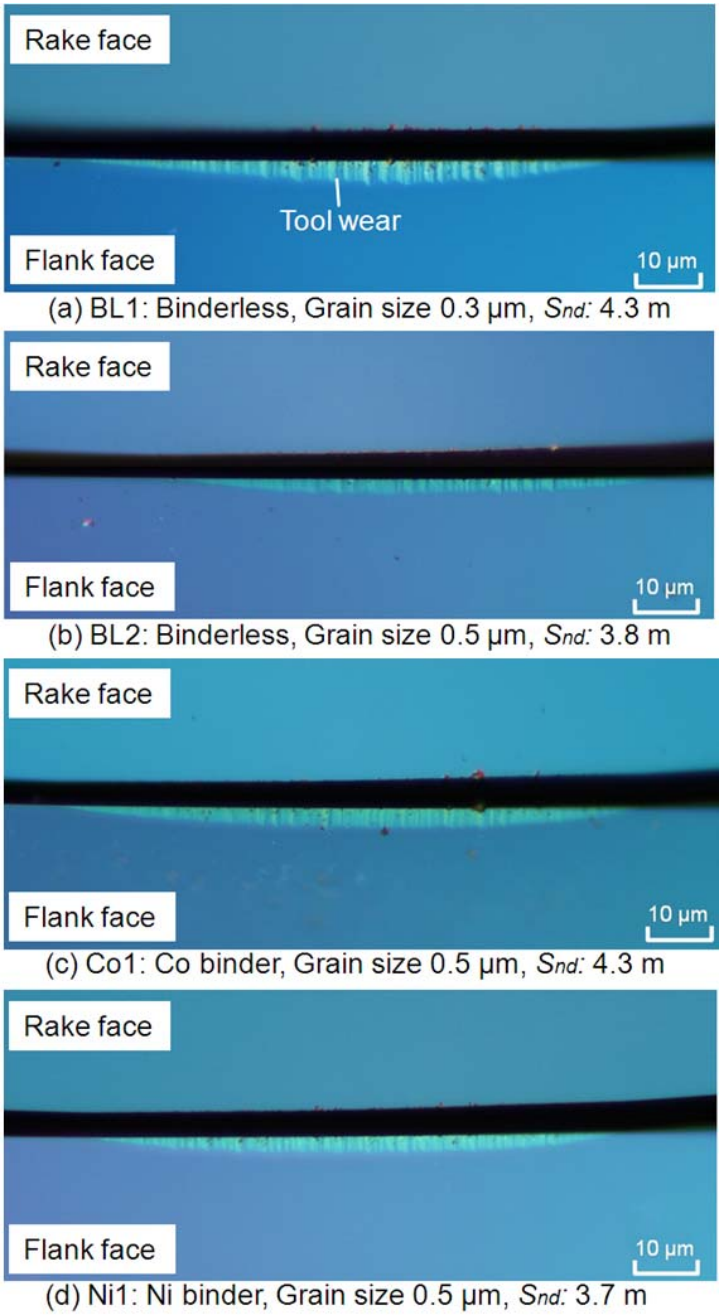

Fig. 3.4 Tool damages after the planing experiments (S_{nd}: nominal cutting distance)

The tool damage is considered to be due to the accumulation of small-scale chippings of the cutting edge and scratches. The hardness of single crystal diamond is relatively higher than that of tungsten carbide, while tungsten carbide is still an extremely hard material. Intermittent contact of the diamond tool with the hard particles in the elliptical vibration cycle may occasionally cause local stress concentration at the

cutting edge resulting in micro/nano chipping. Furthermore, diamond particles apart from the cutting edge may behave as extremely hard abrasive. These hard particles of the diamond can scratch the flank face side of the cutting edge and/or accelerate further chipping generation. Consequently, cumulative chipping and scratching on the flank face may develop into the damages shown in Fig. 3.4.

Figure 3.5 shows variations of measured specific cutting forces at a depth of cut of 1 μm with increase of the nominal cutting distance.

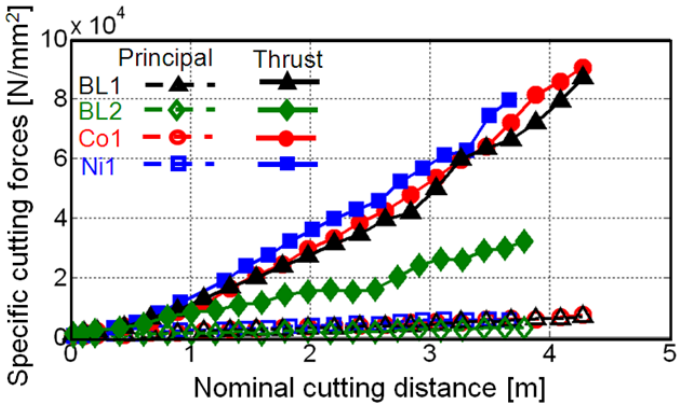

(a) Cutting force variation in planing of different workpieces

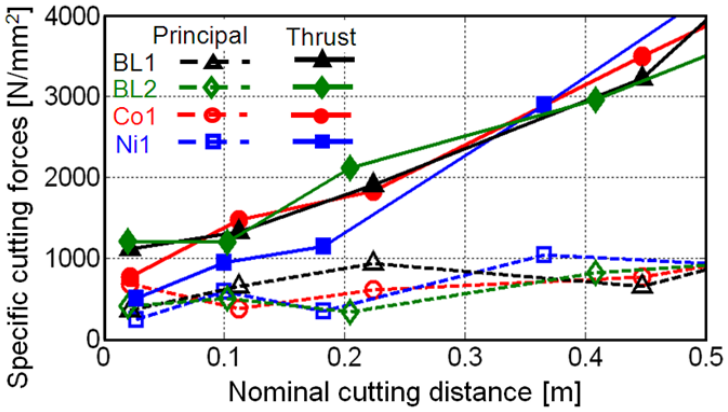

(b) Cutting force variation at the beginning of planing

Fig. 3.5 Cutting force variation in planing experiments (depth of cut: 0-1.2 μm, amplitudes: 2-1 $\mu m_{0\text{-}p}$, nominal cutting speed: 250 mm/min)

The specific cutting forces, especially thrust components, increase significantly. For instance, the thrust and principal components increased up to about 78 times and 20 times larger than the initial values observed in BL1. However, the smallest increase is

observed in machining of BL2. This cutting force increase is considered to be due to the tool damage on the flank face. Geometry deterioration of the flank face generally initiates a ploughing process, where large edge force generates due to the contact of the flank face to the workpiece. Measured force increases are in a good agreement with the observed tool damages shown in Fig. 3.4. Also from Fig. 3.5, it can be observed that there is no obvious difference in the cutting force variations in machining Co1 and Ni1 regardless of different binder phases. Compared with binderless BL2, Co1 and Ni1, tool damage is smaller in BL2. These facts indicate that the binder-containing materials accelerate development of tool wear due to their thermo chemical affinity to diamond. Compared with BL1 and BL2, the tool wear progressed faster in BL1. This may be due to higher hardness and toughness of finer grain materials.

In terms of tool life, BL2 shows the best performance among the investigated materials. The machined surface of BL2 was, however, filled with single-grain-size defects in the whole cutting process, see Fig. 3.3. Hence, BL2 is impracticable. Considering surface integrity, ductile mode machining can be attained just in BL1, Co1 and Ni1. According to the tool damage amount with respect to the nominal cutting distance, there seems to be not explicit difference in the cutting force and in the microscope observation. Hence, tool lives in planing of BL1, Co1 and Ni1 are almost identical.

Figure 3.6 shows variations of surface roughness measured along the pick feed direction.

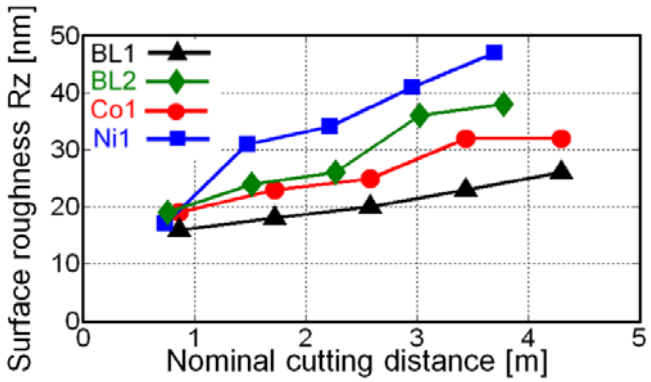

Fig. 3.6 Variations of surface roughness in planning

Better surface roughness can be attained in BL1 machining. Moreover, according to material properties, binderless tungsten carbide has the excellent mechanical, thermal and chemical properties, such as hardness and wear/heat resistance. Therefore, binderless tungsten carbide with the finest grain size BL1 is considered to be the best material for glass molding among the evaluated materials.

In order to investigate the chip formation mechanism in elliptical vibration cutting of tungsten carbide, chips were collected through a series of the planing experiments. Figure 3.7 shows SEM photographs of the chips collected during planing of BL1 and Co1 at the nominal cutting distance of 0.4 m. The continuous chips consisting of needle-type-like segments were observed in Co1, while thin chip segments were almost discontinuous in BL1. The thickness of the thin chip segments was less than about 200 nm. As the same chip formations were observed depending on the presence of binder material, the toughness of the material is considered to affect the continuity of the chip formation. The chip width agrees with the contact length of the cutting edge to the workpiece calculated from geometry. This fact indicates that ductile mode machining was attained successfully in both experiments.

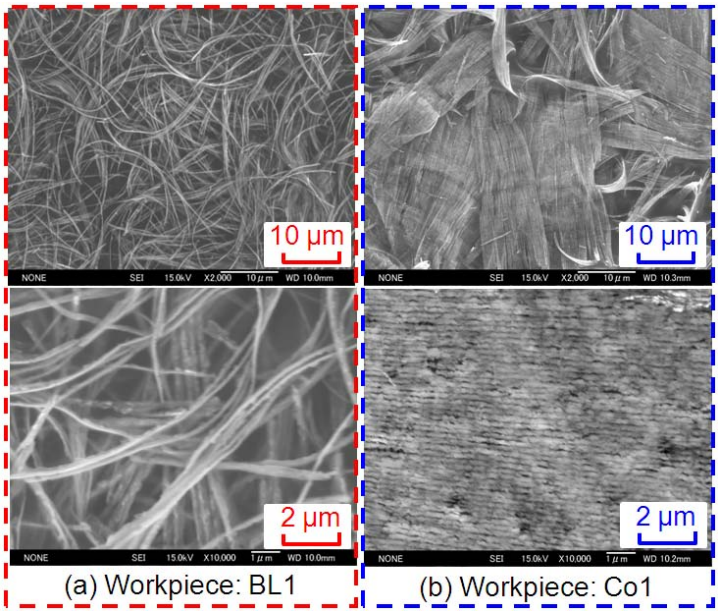

Fig. 3.7 SEM images of machined chips in elliptical vibration cutting

In the planing operation, the maximum uncut chip thickness (t_{max}) varies along the

cutting edge position, which is derived from the nose radius of the cutting tool (R), the maximum depth of cut (d_{max}) and the pick feed (f_p), as shown in Fig. 3.8. As R =1000 μm, d_{max}=1.2 μm and f_p=5 μm, t_{max} becomes 232 nm. The nominal cutting distance in one vibration cycle L_n is about 115 nm. As the thickness of the thin chip segments are near to t_{max} and L_n, each needle-type-like chip segment may be generated in each vibration cycle.

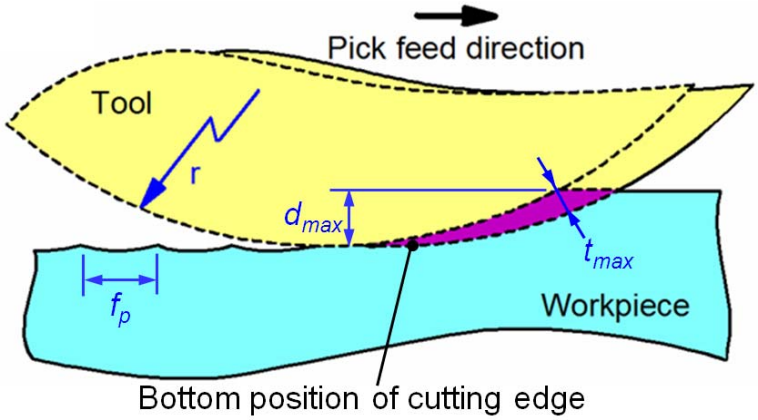

Fig. 3.8 Maximum uncut chip thickness in radial direction of tool edge

3.3.2 Influence of cumulative cutting distance

At first, the influence of the nominal cutting speed on tool life is investigated where planing experiments on BL1 are conducted. Machining performance in ordinary cutting was also compared. Crystal orientation of the tool was set to be R(100)F(100). Amplitudes A_c-A_d of 2-1 $\mu m_{0\text{-}p}$ were adopted in the elliptical vibration cutting. As the nominal cutting speeds are set to 125, 250 and 1000 mm/min, corresponding maximum instantaneous uncut chip thicknesses, which were presented in Chapter 2 as MIUCTs, are about 0.8, 3.2 and 25.1 nm, respectively. Figure 3.9 shows the variation of measured specific cutting forces at the depth of cut of 1 μm with the increase of nominal cutting distance.

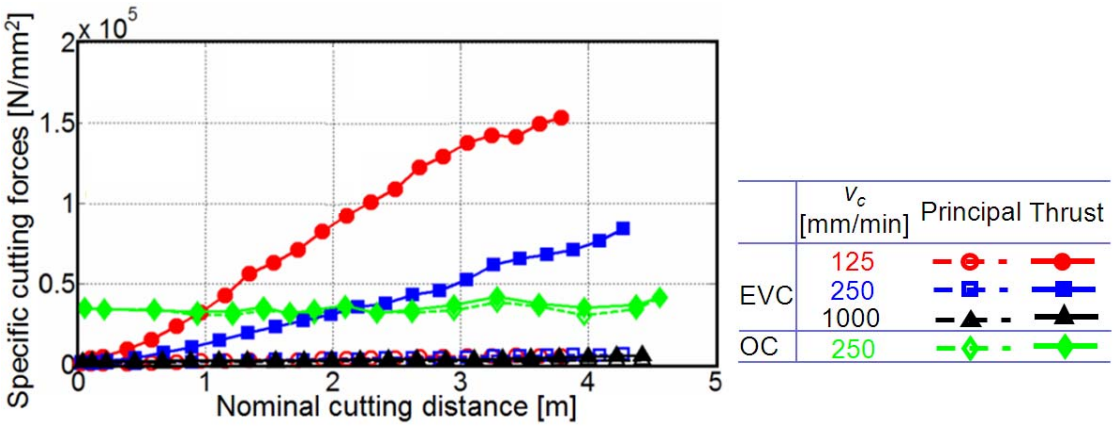

Fig. 3.9 Influence of nominal cutting distance on cutting forces (v_c: nominal cutting speed mm/min, OC: ordinary cutting, EVC: elliptical vibration cutting)

As shown in Fig. 3.9, the cutting force rapidly increases at lower cutting speed, while there is no explicit change of the cutting force in the ordinary cutting (OC) within the nominal cutting distance of 4.3 m. Note that the cutting force in the elliptical vibration cutting generally becomes small especially at a low nominal cutting speed due to thinner instantaneous uncut chip thickness in each elliptical vibration cycle. Comparing the results at the same nominal cutting speed of 250 mm/min, the thrust force in the elliptical vibration cutting becomes surprisingly larger than that in the OC at the nominal cutting distance of larger than 2.4 m. The experimental results indicate that the tool damage is large in EVC especially at low nominal cutting speed. The microphotographs of the cutting edges after the experiments are shown in Fig. 3.10. The flank wear becomes large in the elliptical vibration cutting especially at lower nominal cutting speed although the nominal cutting distances are almost the same. Thus, this result also supports the observation that the cutting force deteriorates. However, it is generally considered that the nominal cutting speed does not affect the tool life at such low speed condition in case of the ordinary cutting of tungsten carbide.

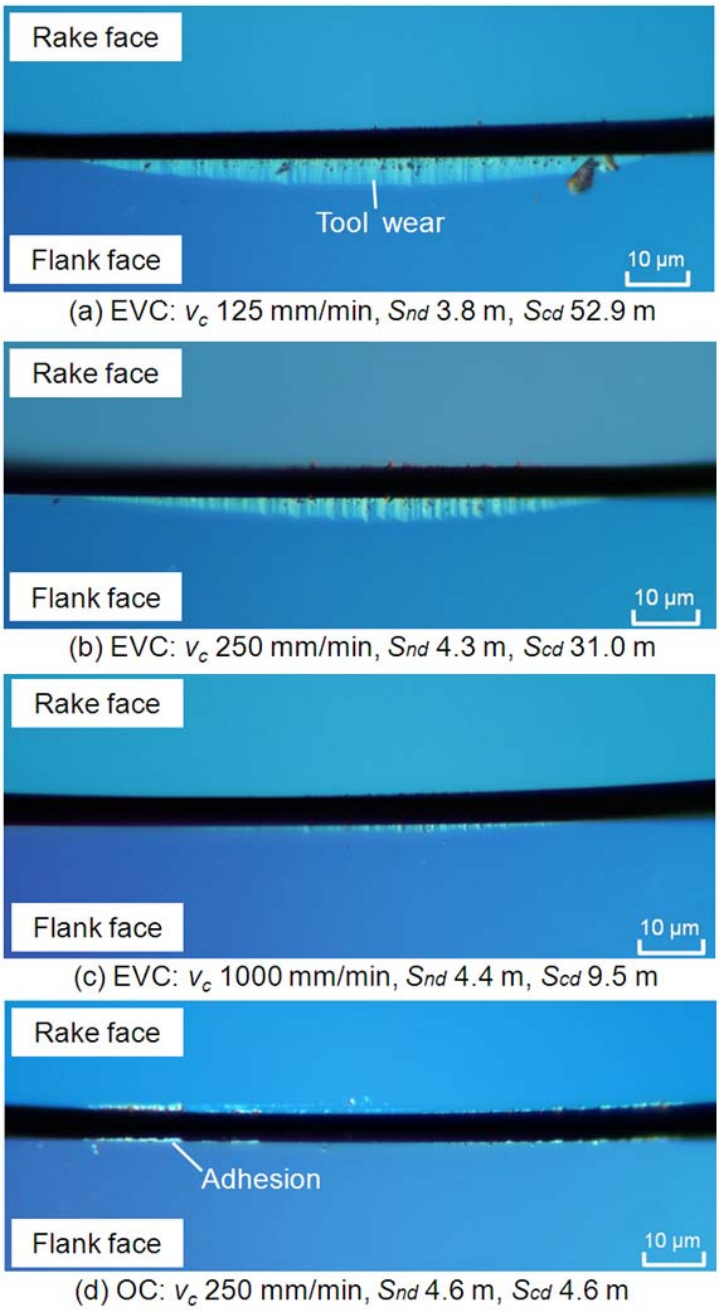

Fig. 3.10 Tool wear patterns with different nominal cutting speeds (v_c: nominal cutting speed, S_{nd}: nominal cutting distance, S_{cd}: cumulative cutting distance, OC: ordinary cutting, EVC: elliptical vibration cutting)

This interesting phenomena is considered to be related to the characteristics of the EVC process. In the EVC process, the actual cutting distance in one vibration cycle L_c becomes much longer than the tool feed distance in one vibration cycle L_n, as illustrated

in Fig. 3.11. The nominal cutting distance S_{nd} can be expressed as:

$$S_{nd} = L_n f \tau = v_c \tau , \tag{3-1}$$

where f is the vibration frequency, v_c is the nominal cutting speed and τ is the cutting time. The cumulative cutting distance S_{cd} can be formulated as following;

$$S_{cd} = L_c f \tau = L_c f \frac{S_{nd}}{v_c} . \tag{3-2}$$

Eq. (3-2) indicates that the cumulative cutting distance is inversely proportional to the nominal cutting speed, namely, the cumulative cutting distance S_{cd} with respect to a certain nominal cutting length S_{nd} becomes longer at a lower nominal cutting speed v_c and vice versa. The tool damage may be related to this cumulative cutting distance rather than the nominal cutting distance in the elliptical vibration cutting.

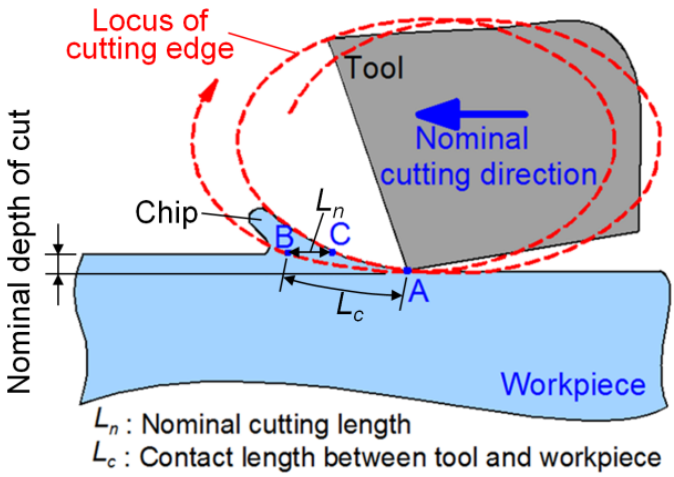

Fig. 3.11 Nominal cutting length and contact length in one vibration cycle

The cumulative cutting distance in the elliptical vibration cutting is calculated for each experiment. Since uncut chip thickness also distributes unevenly along the cutting edge direction as illustrated in Fig. 3.8, the cumulative cutting distance varies depending on cutting edge position. The nominal cutting distance also distributes depending on the cutting edge position due to the depth of cut change. In the present study, the maximum values in the distribution of the cumulative cutting distance along the cutting edge are defined as the cumulative cutting distance S_{cd} and the nominal cutting distance S_{nd}.

Considering the elliptical vibration motion and the depth of cut change

simultaneously, the distribution of the cumulative cutting distance is calculated. It should be noted that, unlike elliptical vibration cutting, the distribution of the cumulative cutting distance along the cutting edge position does not change depending on the cutting speed in ordinary cutting. Fig. 3.12 demonstrates the calculated distributions of the total cutting distance cumulated in one cutting feed stroke, where the cutting edge position is defined relatively from the bottom end. The calculated distributions are almost proportional to the cutting speed in the elliptical vibration cutting, and the distance becomes the maximum at a relative cutting edge position of about 20 μm, i.e., the middle position of used cutting edge. Meanwhile, in the ordinary cutting, the distance becomes the maximum at the bottom position of the cutting edge.

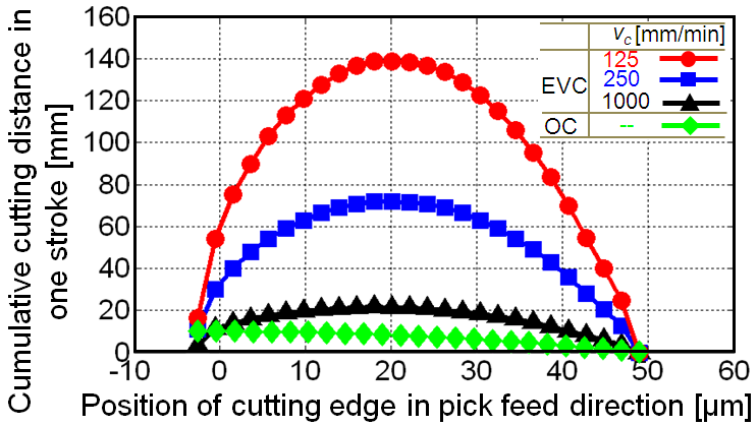

Fig. 3.12 Distribution of cumulative cutting distance along cutting edge (v_c: nominal cutting speed mm/min, OC: ordinary cutting, EVC: elliptical vibration cutting, feed length in nominal cutting direction: 10 mm, depth of cut: 0-1.2 μm, amplitudes: 2-1 $\mu m_{0\text{-}p}$)

The relationship between the specific cutting forces and the cumulative cutting distance is shown in Fig. 3.13. As shown in Fig. 3.13, the cumulative cutting distance becomes longer in the EVC especially at a lower nominal cutting speed even though the nominal cutting distances are almost identical. The experimental results of force variations with respect to the cumulative cutting distances show similarity in the EVC. This fact indicates that the cumulative cutting distance makes dominant contribution to the tool damage. Hence, higher nominal cutting speed leads to longer tool life in the EVC process.

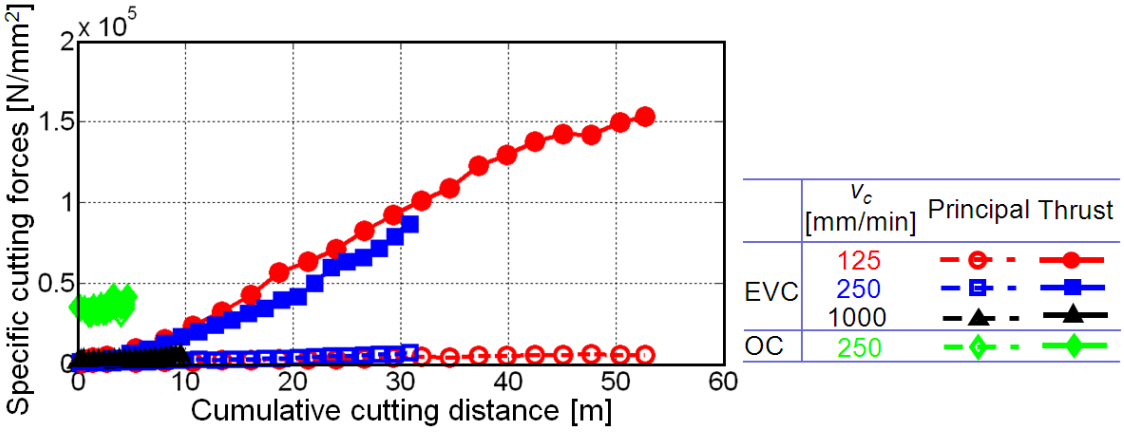

Fig. 3.13 Influence of cumulative cutting distance on cutting forces (v_c: nominal cutting speed mm/min, OC: ordinary cutting, EVC: elliptical vibration cutting)

Figure 3.14 shows scanning electron microscope (SEM) and atomic force microscope (AFM) images of the machined surface at the nominal cutting distance of 0.4 m. The surface machined at a higher nominal cutting speed is filled with single-grain-size defects as well as the grooving experiment. It should be noted that maximum instantaneous uncut chip thickness (MIUCT) is 25.1 nm in this nominal cutting speed, which is too large to achieve ductile mode machining.

Figure 3.15 shows SEM images of the collected chips at the same nominal cutting distance of 0.4 m. With increase of the nominal cutting speed, the chip formation becomes discontinuous. At the nominal cutting speed of 1000 mm/min, the surface of the chip segment is not smooth but asperous due to tungsten carbide grains. Hence, the nominal cutting speed needs to be set lower to attain better surface integrity though the tool life is long at a higher nominal cutting speed. Considering taking a balance of the tool life and surface integrity, the nominal cutting speed of 250 mm/min may be reasonable in practical use.

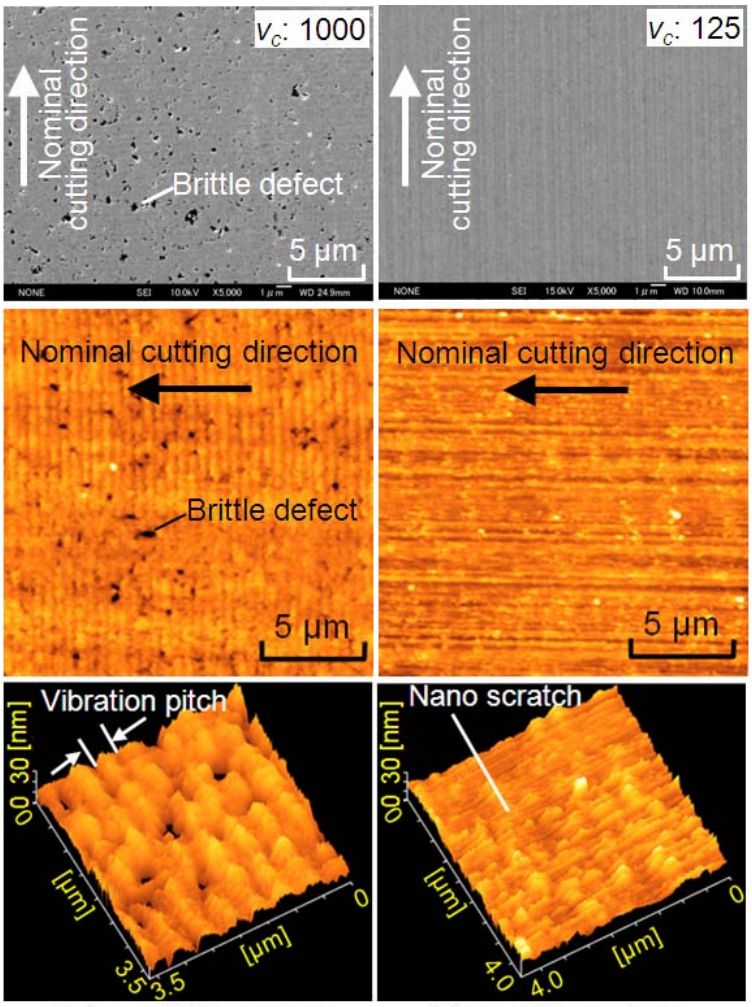

Fig. 3.14 SEM and AFM images of machined surfaces in elliptical vibration cutting (nominal cutting distance: 0.4 m, v_c: nominal cutting speed mm/min)

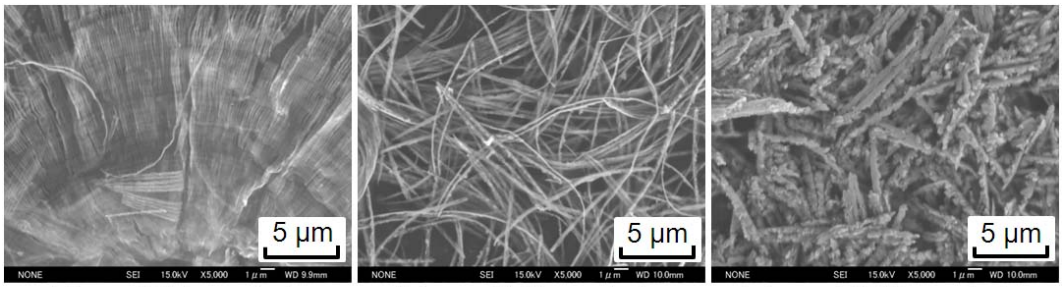

Fig. 3.15 SEM images of chip collected in elliptical vibration cutting

Figure 3.16 shows the machined surface and the collected chips in the EVC and

the OC at the same nominal cutting distance of 4.3 m.

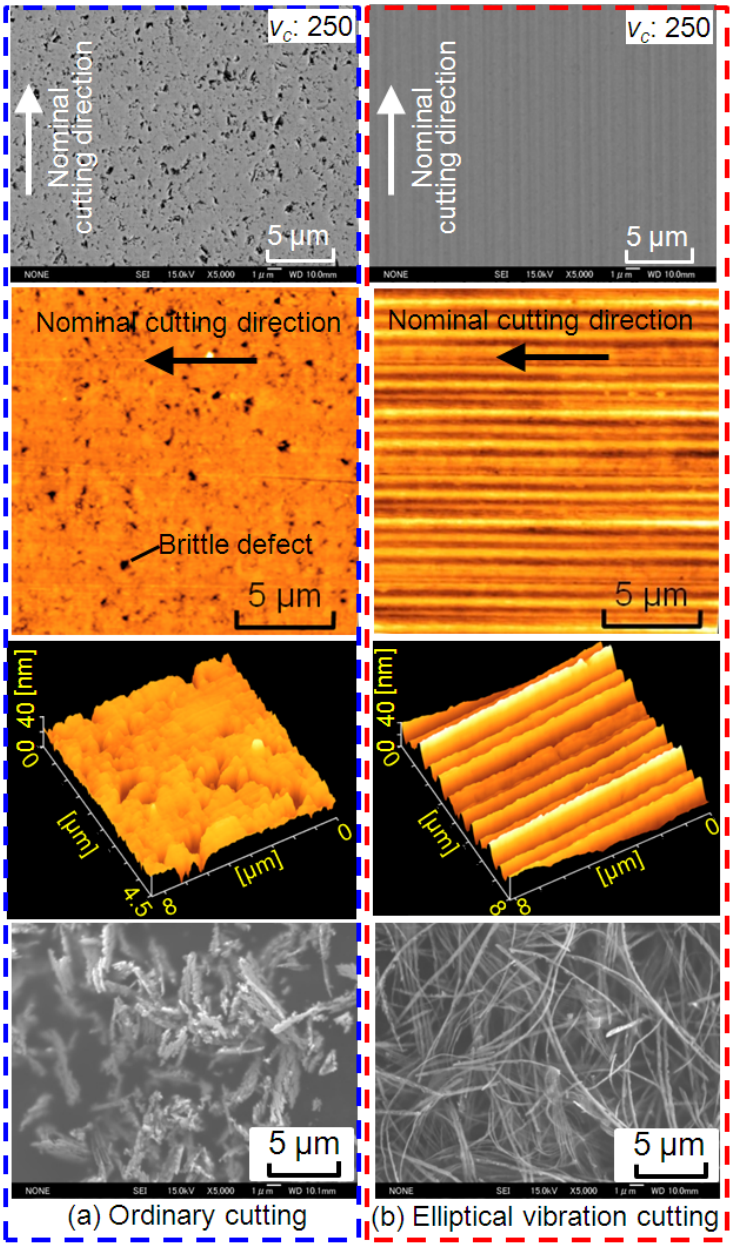

Fig. 3.16 Photographs of machined surface and chips formed in ordinary and elliptical vibration cutting (v_c: nominal cutting speed mm/min, nominal cutting distance: 4.3 m)

In the OC, generation of defects due to brittle fracture cannot be suppressed as well as the grooving experiment. The chip segment surface is also asperous, which is similar to that in the EVC at the nominal cutting speed of 1000 mm/min. Tool damage is surprisingly small, however adhesion is observed on the cutting edge in Fig. 3.10.

Fracture-free ductile mode machining can be attained in the EVC at the nominal cutting speed of 250 mm/min, while continuous scratch marks along the cutting direction can be observed clearly. This surface quality deterioration is due to the cutting edge geometry deterioration. Because of the long cumulative cutting distance heretofore described, the surface damage in the elliptical vibration becomes large as compared to the OC at the same nominal cutting distance.

3.3.3 Influence of crystal orientation of diamond tools

In order to investigate the influence of the tool crystal orientation on tool life, planing experiments of BL1 were carried out by use of tools with crystal orientations of R(100)F(100) and R(110)F(100). The amplitude in the nominal cutting/ depth of cut directions was set to 2/1 $\mu m_{0\text{-}p}$. The nominal cutting speed and the pick feed were set to be 250 mm/min and 5 μm, and the depth of cut was changed from 0 μm to 1.2 μm. Total nominal cutting distances are 4.3 m and 19.04 m respectively.

The tool damages in the planing experiments are compared in Fig. 3.17. By changing the crystal orientation from R(100)F(100) to R(110)F(100), flank wear decreases drastically while slightly larger chipping generates on the flank face at the same nominal cutting distance of 4.3 m. This fact indicates that R(110)F(100) is good at suppressing scratching damage on the flank face but poor in fracture toughness. The final nominal cutting distance in R(110)F(100) is 19.04 m, which is about 5 times longer than that in R(110)F(100), however the maximum flank wear width seems to be identical. Figure 3.18 shows variations of the measured specific cutting forces at the depth of cut of 1 μm in the EVC. Cutting force constants are increasing considerably slowly by using R(110)F(100). At the nominal cutting distance of 4 m, the thrust force of the tool with crystal orientation of R(110)F(100) is almost 15 times lower than that of R(100)F(100). This fact indicates that reduction of flank wear by use of tool with R(110)F(100) is significantly advantageous to decreases cutting force, which may result in better machining accuracy.

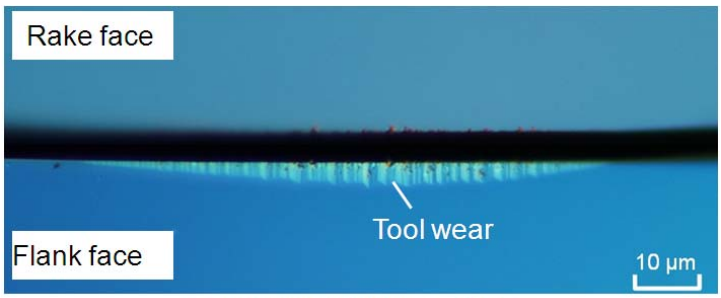

(a) R(100)F(100), S_{nd} 4.3 m

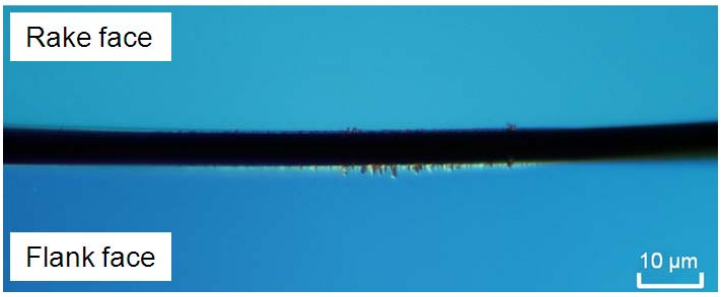

(b) R(110)F(100), S_{nd} 4.3 m

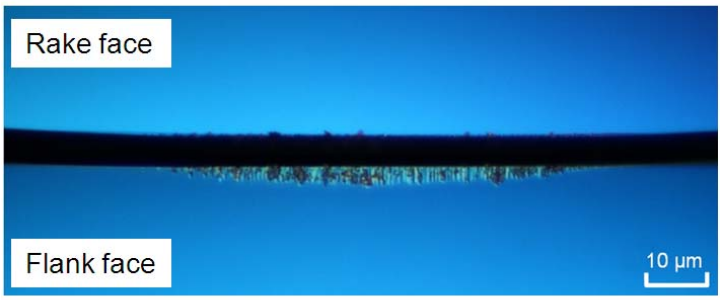

(c) R(110)F(100), S_{nd} 19.04 m

Fig. 3.17 Microphotographs of cutting edges with different crystal orientations (R: rake face, F: flank face, S_{nd}: nominal cutting distance)

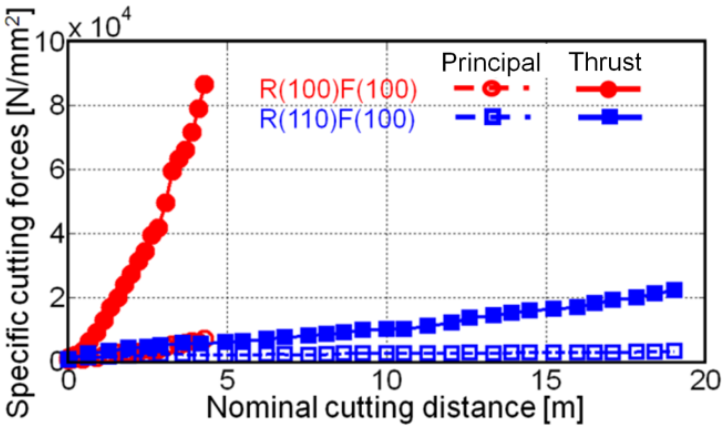

Fig. 3.18 Influence of crystal orientation on specific cutting force increase (workpiece: BL1, amplitudes: 2-1 $\mu m_{0\text{-}p}$, nominal cutting speed: 250 mm/min)

Figure 3.19 shows AFM images of machined surfaces and measured surface roughness along the pick feed direction. Surface quality and roughness are not distinctively different at the same cutting distance, and the surface roughness is less than 35 nm Rz within the nominal cutting distance of 4.3 m. Considering nature of less tool damage in R(110)F(100), crystal orientation of R(110)F(100) may be better to attain longer tool life in practical use. With increase of the nominal cutting distance to 19.04 m, the roughness increases almost linearly, however the maximum roughness is still less than 100 nm Rz.

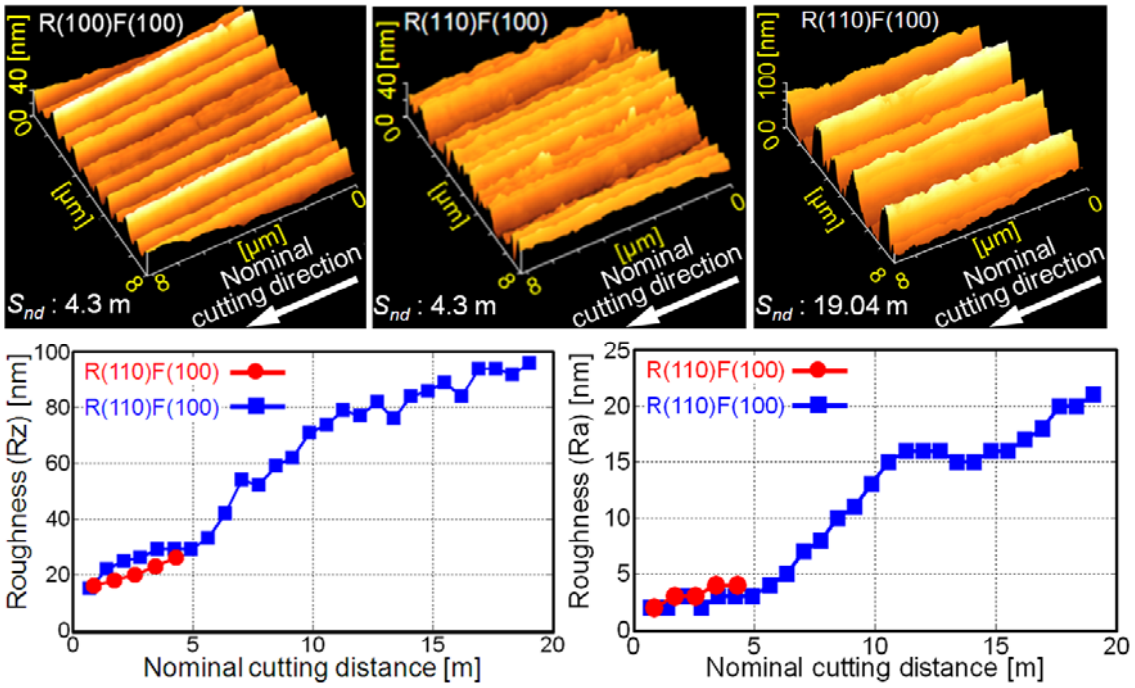

Fig. 3.19 AFM images of machined surfaces and roughness variation with increase of nominal cutting distance

3.3.4 Clarify features of tool wear and planing performance

Tool wear causes the cutting force to increase and thus the surface quality deteriorates. Hence, it is important to evaluate features of tool wear. Influence of material properties and cutting conditions on tool wear progress and cutting performance are analyzed in this section. The experimental results in planing and related material properties are summarized in Table 3.3. Tool wear amount is

represented by the maximum value of the observed flank wear width VB_{max}. Tool wear resistance A_e is an evaluation factor representing the strength of the cutting edge, which is defined and quantified by Zong et al. [107]. Note that diamond is an anisotropic material, thus the tensile strength of C-C bond on the topmost layer of the cutting edge varies depending on the crystal orientation. High tool wear resistance A_e is considered to be effective to suppress tool wear progress.

Table 3.3: Experimental results in planing

Material	v_c mm/min	H_m Gpa	S_{cd} m	S_{nd} m	K_t N/mm^2	Rz nm	VB_{max} μm	A_e GPa	Crystal orientation of diamond tool
BL1	125	25.48	52.9	3.8	153355	48	4.32	5.81	R(100)F(100)
	250		31.0	4.3	84180	26	3.60		
	1000		9.5	3.7	5745	22	1.44		
	250		31.0	4.3	5463	32	1.98	25.70	R(110)F(100)
			137.3	19.0	22160	96	2.88		
BL2	250	23.52	27.4	3.8	31981	38	2.16	5.81	R(100)F(100)
Co1	250	19.60	31.0	4.3	90191	32	2.88	5.81	R(100)F(100)
Ni1	250	16.66	26.7	3.7	79264	47	2.52	5.81	R(100)F(100)

v_c: Cutting speed [mm/min]; H_m: Hardness of workpiece material [GPa]; S_{cd}: Cumulative cutting distance [m]; S_{nd}: Nominal cutting distance [m]; K_t: Specific cutting force in thrust direction [N/mm^2]; Rz: Surface roughness [nm]; VB_{max}: Maximum flank wear width [μm]; A_e: Tool wear resistance [GPa].

As previously mentioned, tool damage is directly related to the cumulative cutting distance rather than the nominal cutting distance. Higher hardness and lower tool wear resistance are also considered to accelerate flank wear progress. Hence, the relationship between VB_{max} and $S_{cd} \cdot H_m / A_e$ are investigated from the experimental results in Table 3.3. Figure 3.20 shows a plot of VB_{max} against $S_{cd} \cdot H_m / A_e$ and its regression line, where flank wear VB_{max} proportionally increases with increase of $S_{cd} \cdot H_m / A_e$. From this fact, tool wear can be predicted roughly from the cumulative cutting distance, hardness of workpiece and tool wear resistance values by following Eq.

(3-3).

$$VB_{\max} = a_1(S_{cd} \cdot H_m / A_e) + a_0 , \quad (3\text{-}3)$$

where a_1=1.33e-8 [m] and a_0=1.29e-6 [m].

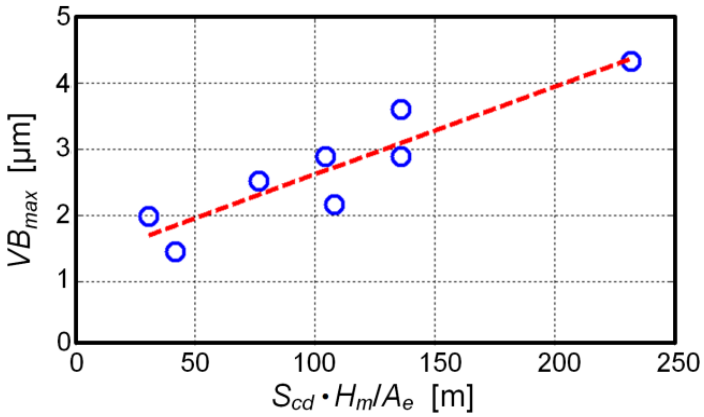

Fig. 3.20 Tendency of tool wear progression

It is also considered that the cutting force increase is mainly caused by the flank face contact to the workpiece. Hence, the cutting force, especially the thrust component, is strongly associated with the cutting edge deterioration due to edge force. In the present study, the thrust component of the specific cutting force K_t is modeled to be proportional to the maximum wear width VB_{max}. Furthermore, we found that the thrust force in R(110)F(100) is almost 4 times lower than that in R(100)F(100) for almost the same VB_{max}. This fact indicates that worn cutting edge geometry may be different depending on the crystal orientation of the tool and this nature affects the cutting force deterioration significantly. In order to compensate the influence of crystal orientation, a coefficient P is defined and introduced in the present research. The coefficient P represents the influence of tool geometry difference depending on the crystal orientation of the tool. From the relative ratio of the cutting forces measured at the same VB_{max}, the values of P are determined as 1 in R(100)F(100) and 1/4 in R(110)F(100). Figure 3.21 shows a plot of K_t against $P \cdot VB_{\max}$. The regression line of the experimental results, which is shown in Fig. 3.21, is expressed by following Eq. (3-4),

$$K_t = b_1(P \cdot VB_{\max}) + b_0 , \quad (3\text{-}4)$$

where b_1=3.56e7 [N/mm^3] and b_0=-2.16e4 [N/mm^2]. Based on Eqs. (3-3) and (3-4), the maximum flank wear VB_{max} and specific thrust force K_t are approximately predicted as a

function of the cumulative cutting distance S_{cd} and material properties.

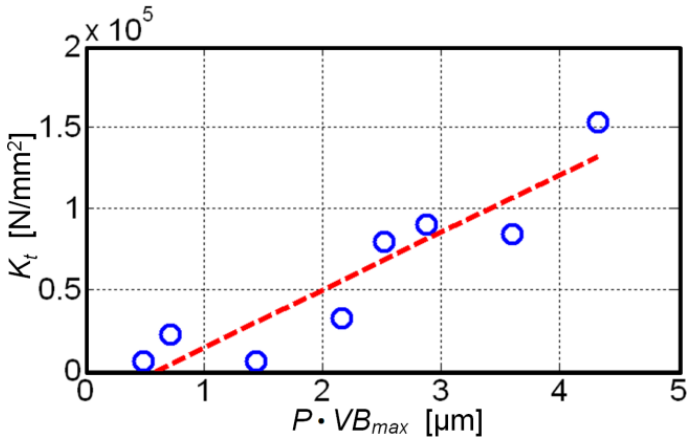

Fig. 3.21 Variation of specific cutting force in thrust direction with tool wear progression

As noted, the cumulative cutting distance has a significant influence on tool wear. Deterioration of the cutting edge causes less quality of the finished surface and increases the surface roughness. Hence, the influence of the cumulative cutting distance on surface roughness is investigated, as shown in Fig. 3.22. It can be confirmed that the maximum surface roughness *Rz* proportionally increases with the increase of the cumulative cutting distance S_{cd}. From this relation, it may be possible to predict surface roughness roughly especially when the cumulative cutting distance is long. Influences of material properties, such as hardness of the workpiece and tool's crystal orientation, on surface roughness were also explored, however strong relationship with surface roughness could not be found.

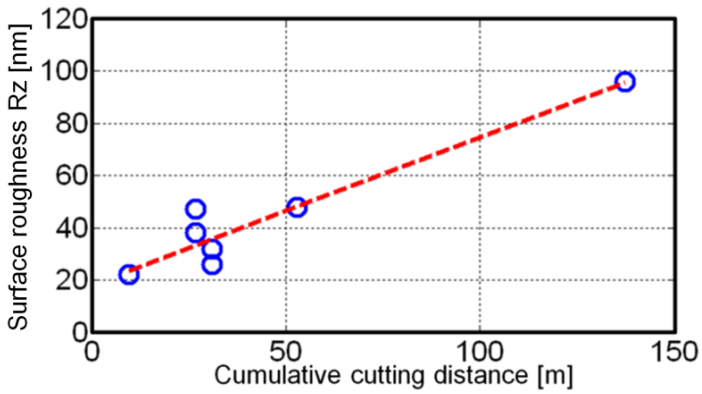

Fig. 3.22 Variation of surface roughness with cumulative cutting distance

3.4 Summary

Through fundamental planing experiments, an interesting nature of tungsten carbide machining is clarified. Smaller grain size and presence of the binder phase are advantageous to prevent fracture generation. However, these conditions are inversely disadvantageous to realize longer tool life. The tool wear progressed faster due to higher hardness and toughness of finer grain materials. The binder-containing materials accelerate the development of tool wear due to their thermo chemical affinity to diamond. Moreover, tool damage progress in EVC also has strong relation with the cumulative cutting distance and the crystal orientation of the tool. Thus, appropriate conditions need to be selected to make a good balance in the surface quality and the tool life. The conditions, which are considered not only to be comprehensively preferable for practical machining of tungsten carbide in ductile mode but also to satisfy reasonable machining efficiency, are summarized in Table 3.4. Based on the fundamental planing experiments, the feature of tool wear propagation is also evaluated. The maximum flank wear proportionally increases with increase of the cumulative cutting distance and the hardness of workpiece, and inversely proportional to the increase of tool wear resistance value. Due to the cutting force increase mainly caused by the flank face contact to the workpiece, the cutting force, especially the thrust component, is modeled to be proportional to the maximum flank wear. With the aforementioned achievements, the tool wear and specific thrust force can be approximately predicted as a function of the cumulative cutting distance and material properties in advance.

Table 3.4: Preferable conditions for tungsten carbide planing

Workpiece	Binderless with grain size of less than 0.3 μm Binder-containing with grain size of less than 0.5 μm
Cutting conditions	Nominal cutting speed: about 250 mm/min Maximum depth of cut: at least 1.2 μm
Vibration condition	Vibration amplitudes in nominal cutting and depth of cut directions: 2-1 $\mu m_{0\text{-}p}$
Tool	Crystal orientation: R(110)F(100)

Chapter 4

Analytical investigations on machinable part geometry and proposed command compensation method

4.1 Introduction

Micro/nano structured surfaces possess unique and interesting functions. Hence, application technologies of functional surfaces with micro/nano structures have been fascinating research topics in the last few decades. Considering widespread use of textured surfaces applications and their mass production, manufacturing technology of functional surfaces for a variety of materials, especially for steel materials, is greatly required. Steel is a typical material that is widely used for mechanical elements and molding. However, Paul et al. [54] found that in ferrous material machining chemical affinity of materials triggers extreme chemical reaction of single crystal diamond (SCD) tools. Because of this chemical nature, conventional diamond cutting is not applicable to machining of steel due to rapid tool wear and surface deterioration [108]. Instead of diamond cutting, Brinksmeier et al. [109] successfully applied ultra-precision grinding and abrasive polishing to fabrication of ultra-precision dies and molds made of hardened steel, while it is extremely difficult to fabricate sophisticated micro/nano-scale structures especially with sharp edges by grinding/polishing. These restrictions in conventional machining methods in fact define the bottleneck of practical use of hardened steel with functional surfaces.

For the last few decades, ultrasonic vibration cutting technology has been successfully applied to difficult-to-cut materials machining by use of diamond tools [60]. In particular, elliptical vibration cutting (EVC) technology [61] is considered as a potential candidate for the functional surface fabrication on steel materials. With the development of ultrasonic elliptical vibration cutting devices [75], Shamoto and Moriwaki [77] verified the feasibility of steel material machining by use of SCD tools. Based on successful cutting performance of EVC, Suzuki et al. [62] explored further possibilities of

functional surface machining on difficult-to-cut materials by applying EVC, and proposed a unique micro/nano sculpturing method. In this proposed method, amplitude of the elliptical vibration is actively controlled during machining. Because of this amplitude control, the depth of cut can be changed rapidly without fast tool servo (FTS) but as being controlled by the conventional FTS technology. Fundamental machining performance was investigated through primitive sculpturing experiments, and simple micro/nano textured patterns were machined successfully on workpieces made of hardened steel and tungsten carbide [62, 94-96], as introduced in Chapert 1 and Chapter 2. On the other hand, the proposed amplitude control machining method imposes several restrictions in machinable part geometry, such as height variation range, curvature, and slope angle. These restrictions are directly associated with not only the performance of elliptical vibration equipment but also EVC conditions, whereas theoretical investigations on restrictions in machinable part geometry have not been conducted enough [62, 110, 111]. Hence, it is sometimes difficult to estimate the feasibility of functional surface machining by the proposed method in advance. Moreover, tool geometry also imposes a limit on the machinable part geometry, such as the flank/rake face contact to the target shape and the tool radius restriction on the sharpness of concave part geometry. In addition, the envelope of the cutting edge trajectory is superimposed as a textured surface in this method. As this envelope shape differs from the reference command shape for vibration amplitude control, reference command shape may need to be compensated based on the target shape geometry and EVC conditions for accurate machining.

In order to clarify restrictions in machinable part geometry, theoretical investigations are conducted in this chapter. According to the vibration conditions and the tool geometry, restrictions in machinable part geometry are clarified and formulated by considering the kinematic model of EVC. Subsequently, a compensation method of vibration amplitude command for highly-accurate machining is proposed. Through theoretical simulations, the proposed compensation method is evaluated. The research works studied in this chapter are also presented in the author's published papers [110, 111].

4.2 Amplitude control sculpturing method

The principle of amplitude control sculpturing method was briefly introduced in Chapter 2. In this section, this method is investigated in detail.

Figure 4.1 shows a schematic illustration of the EVC process. A part of elliptical vibration trajectory is superimposed on the machined surface in each vibration, resulting in regular undulation on the finished surface, as shown in Fig. 4.1.

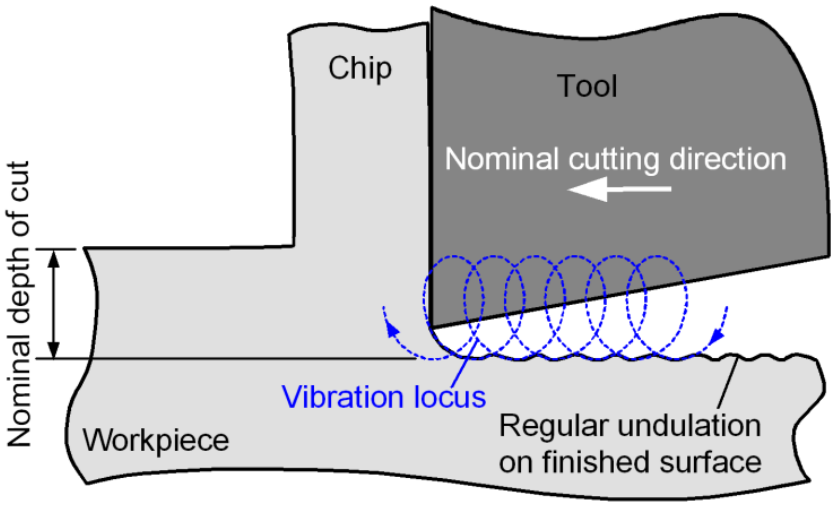

Fig. 4.1 Schematic illustration of elliptical vibration cutting

In order to decrease the undulation amplitude and to obtain better surface roughness, a low nominal cutting speed condition is generally applied. In contrast to general EVC, Guo and Ehmann [112] proposed to apply this unique nature of undulation generation onto surface texturing, and they developed a texturing method by utilizing EVC process [113], where by applying relatively higher nominal cutting speed with constant elliptical vibration amplitude, large undulation is superimposed in each vibration as a texture. As the nominal cutting speed is relatively high, machining efficiency is also better as compared with that in general EVC. However, only simple and regular structure can be fabricated in the nominal cutting direction by this method. On the other hand, Suzuki et al. [62] have proposed another texturing method, where the vibration amplitude is actively controlled at relatively low nominal cutting speed.

Figure 4.2 demonstrates the proposed amplitude control sculpturing method, where the vibration amplitude in the depth of cut direction is actively controlled in the EVC process. The trajectory of the cutting edge, then, changes dynamically, and its envelope is transferred to the finished surface. By controlling the amplitude ultra-precisely at high speed, arbitrary ultra-precision sculpturing of difficult-to-cut materials can be achieved efficiently without using the conventional FTS technology. In addition, the nominal cutting speed is low so that the surface roughness becomes significantly small. In other words, the elliptical vibration cutting technology is already equipped with a FTS function by itself. Hence, arbitrary micro/nano texturing with high efficiency can be available on steel materials.

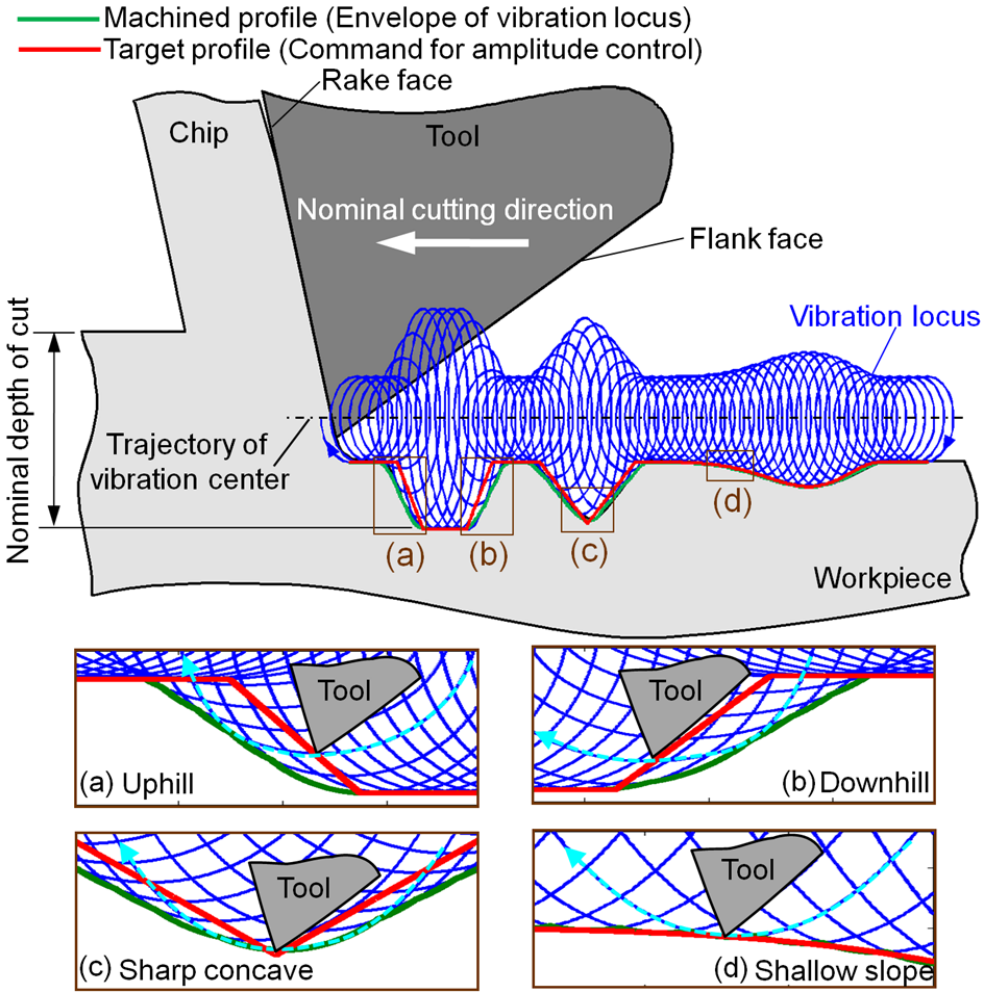

Fig. 4.2 Amplitude control sculpturing in elliptical vibration cutting

However, the proposed amplitude control sculpturing method imposes several restrictions in machinable part geometry due to the nature of the EVC's specific process. In Fig. 4.2, the vibration trajectory is described by applying the vibration amplitude command in the depth of cut direction, which corresponds to the target profile of the machining surface. For simplification, the vibration amplitude control system is assumed as being able to respond quickly to the input amplitude command without time delay in this paper. The envelope of the vibration trajectory is considered to become a resultant surface geometry ignoring elastic recovery of the workpiece and roundness of the cutting edge. As shown in Fig. 4.2, the depth of cut can be controlled within the maximum value of mean-to-peak amplitude in the depth of cut direction. The shape of the vibration amplitude command roughly agrees with the resultant envelope of the vibration trajectory when the slope of the target profile is shallow, as shown in Fig. 4.2 (d). However, the amplitude command and the resultant envelope do not fully correspond to each other especially at the portions with steep slopes and sharp corners, as shown in Fig. 4.2 (a-c). It should be noted that general cutting using FTS technology never causes this error. The aforementioned disagreement in the vibration amplitude command and the trajectory envelope and restrictions in machinable part geometry are due to the existence of finite amplitude in the nominal cutting direction. In addition, tool geometry also imposes a limit on the machinable part geometry. For instance, the flank face contact to the workpiece in downhill machining needs to be avoided. The nominal rake angle should be large in general, while it decreases relatively in uphill machining, which may result in a large cutting force and deterioration in machining quality. According to the vibration conditions and the tool geometry, restrictions in machinable part geometry are clarified and formulated by considering the kinematic model of EVC in Section 4.3. Then, the compensation method of the vibration amplitude command for modifying the envelope shape of the vibration trajectory is presented in Section 4.4.

4.3 Restrictions in curvature and slope of the target profile

4.3.1 Influence of vibration conditions

In the EVC process, the tool is vibrated at an angular frequency ω and fed at a

nominal cutting speed v_c in x-z plane. Then, the trajectory of the tool can be expressed as follows:

$$x_e = A_c \cos(\omega\tau) + v_c\tau, \quad z_e = A_d \cos(\omega\tau + \varphi), \tag{4-1}$$

where x_e and z_e denote x, z components of a relative position between the tool and the workpiece. x axis and z axis are defined to be parallel to the nominal cutting direction and the depth of cut direction, respectively. A_c and A_d are mean-to-peak amplitudes in the both directions. φ is a phase shift of the vibration, which is typically set to be -90 deg. In the numerical simulations of this chapter, φ is fixed to -90 deg. τ is the time during the elliptical vibration process. The target profile is also defined in x-z plane. Considering the practical applications of the proposed amplitude control sculpturing method, the target profile is expressed in the form of explicit functions, implicit functions, or a set of discrete coordinate data. For simplification, an explicit function is adopted as the target profile in the present research. Hence, z component of a position on the target profile z_{tar} is expressed as an explicit function of x component of the position x_{tar} in the nominal cutting direction, as follows:

$$z_{tar} = f(x_{tar}). \tag{4-2}$$

Then, the curvature of the target profile C_{tar} can be calculated by:

$$C_{tar} = \frac{d^2 z_{tar}}{dx_{tar}^2}\left[1 + \left(\frac{dz_{tar}}{dx_{tar}}\right)^2\right]^{-3/2}. \tag{4-3}$$

C_{tar} is negative on the convex profile but positive on the concave profile. Meanwhile, the curvature of the vibration locus C_e can be derived from Eq. (4-1).

$$\begin{aligned} C_e &= \left(\frac{dx_e}{d\tau}\frac{d^2 z_e}{d\tau^2} - \frac{dz_e}{d\tau}\frac{d^2 x_e}{d\tau^2}\right)\left[\left(\frac{dx_e}{d\tau}\right)^2 + \left(\frac{dz_e}{d\tau}\right)^2\right]^{-3/2} \\ &= \frac{\omega^3 A_c A_d[\sin(\omega\tau)\cos(\omega\tau+\varphi) - \sin(\omega\tau+\varphi)\cos(\omega\tau)] - v_c\omega^2 A_d \cos(\omega\tau+\varphi)}{\{\omega^2[A_c^2 \sin^2(\omega\tau) + A_d^2 \sin^2(\omega\tau+\varphi)] - v_c[2\omega A_c \sin(\omega\tau) + v_c]\}^{3/2}}. \end{aligned} \tag{4-4}$$

The curvature radius can be obtained from curvature, as follows:

$$\begin{cases} CR_{tar} = 1/C_{tar} \\ CR_e = 1/C_e \end{cases}, \tag{4-5}$$

where CR_{tar} is the curvature radius of the target profile and CR_e is the curvature radius of the vibration locus.

The finite curvature radius of the vibration locus yields a curvature restriction in the target profile. Figure 4.2 illustrates a target profile and a part of the corresponding tool

trajectory. It assumes that at the moment of the tool being tangential to the target profile, the position on the vibration locus $\mathrm{P}_e(x_e, z_e)$ is identical with the position on the target profile $\mathrm{P}_{tar}(x_{tar}, z_{tar})$. The phase of the elliptical vibration at the tangential moment is defined as $\varepsilon(=\omega\tau)$. Then, the following equations are given based on Eq. (4-1):

$$x_{tar}=x_e=A_c\cos(\varepsilon)+v_c\,\varepsilon/\omega\,,\quad z_{tar}=z_e=A_d\cos(\varepsilon+\varphi). \tag{4-6}$$

C_e is always positive on the vibration locus. Because of this nature, in terms of the curvature, there is no restriction in convex structures machining by the proposed method. On the other hand, for concave structures machining, as shown in Fig. 4.3, the curvature restriction needs to be taken into account. At the tangential moment, the curvature radius of the vibration locus needs to be smaller than or equal to that of the target profile. Hence, the following equation needs to be satisfied at the tangential moment $\tau=\varepsilon/\omega$ at least to ensure the target profile being machinable in practical.

$$CR_{tar}(x_{tar})\geq CR_e(\tau). \tag{4-7}$$

With the satisfaction of Eq. (4-7), the target profile is machinable according to the curvature restriction, as illustrated in Fig. 4.3 (a).

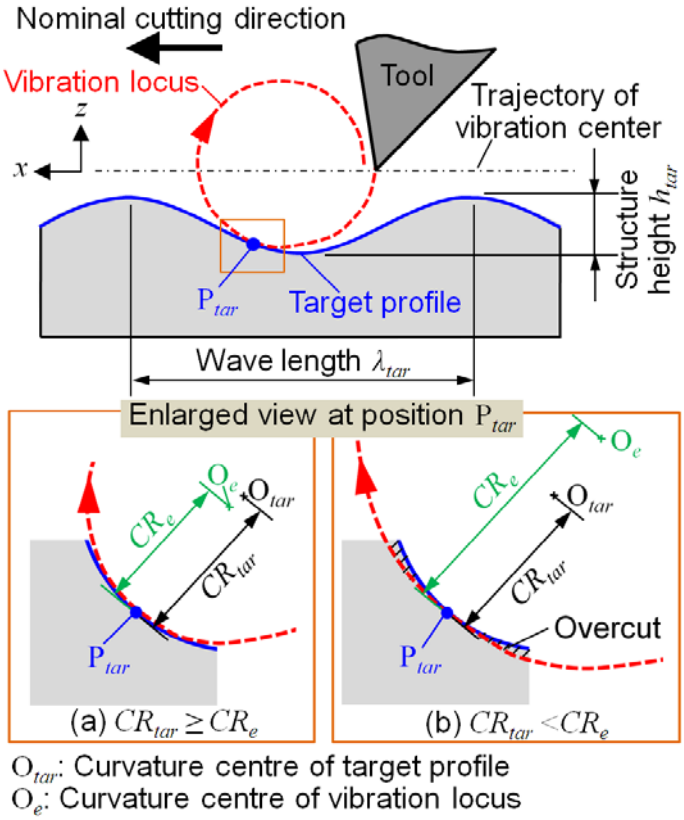

Fig. 4.3 Influence of vibration conditions on machinable part geometry

On the other hand, see Fig. 4.3 (b), with the curvature radius $CR_e(\tau)$ larger than $CR_{tar}(x_{tar})$ at target position P_{tar}, a redundant overcut of the workpiece occurs. In order to ensure the feasibility of the target profile machining by the proposed sculpturing method, the curvatures need to be calculated and compared for any position $\mathrm{P}_{tar}(x_{tar}, z_{tar})$ on the target profile. $CR_{tar}(x_{tar})$ can be derived from Eqs. (4-3) and (4-5) easily. With the phase ε and the corresponding amplitude conditions, $CR_e(\tau)$ can be calculated by Eqs. (4-4) and (4-5). Calculation of the phase ε and the corresponding amplitude conditions in arbitrary target profiles is formulated in Section 4.4 about the vibration command compensation.

In order to explore the influence of the curvature restriction on vibration conditions and machinable part geometry, a sinusoidal structure machining is taken as an example. Along the nominal cutting direction, the function of the target profile is defined as:

$$z_{tar}=\frac{h_{tar}}{2}\sin\left(\frac{2\pi x_{tar}}{\lambda_{tar}}\right), \tag{4-8}$$

where λ_{tar} and h_{tar} are the wave length and the structure height of the target profile, as shown in Fig. 4.3. In this simulation, the target structure is assumed to be machined with an amplitude command at a reference frequency f_{ac} of 100 Hz. The nominal cutting speed v_c can be expressed as a function of the wave length λ_{tar} of the target profile:

$$v_c=\lambda_{tar}f_{ac}. \tag{4-9}$$

As the target profile is sinusoidal, the curvature radius of the concave portion becomes the smallest at the bottom of the profile. Hence, the curvature radius at the bottom profile defines the criterion for determining machinable or not, i.e., $\varepsilon=3\pi/2$ and A_d is the maximum. According to Eq. (4-7), the constraint in the curvature radius is obtained as follows:

$$\frac{{\lambda_{tar}}^2}{2h_{tar}\pi^2}\geq\frac{\left[\omega^2\left({A_c}^2+{A_d}^2\right)+\lambda_{tar}f_{ac}\left(2\omega A_c-\lambda_{tar}f_{ac}\right)\right]^{3/2}}{\omega^2 A_d\left(\omega A_c+\lambda_{tar}f_{ac}\right)}. \tag{4-10}$$

Assuming elliptical vibration conditions and a nominal cutting speed, restrictions of the wave length and the structure height are calculated numerically by Eq. (4-10). Figure 4.4 demonstrates the calculated relationship between the minimum wave length

and the structure height, where the maximum mean-to-peak amplitudes in the depth of cut direction max(A_d) of 0.5, 1, and 2 μm are adopted. Mean-to-peak amplitude in the cutting direction A_c is set to be constant and equal to max(A_d). For instance, in order to machine the structure with a height of 1 μm by max(A_d) of 2 μm, the wave length needs to be longer than 6.3 μm. In the proposed sculpturing method, the maximum structure height needs to be lower than the maximum mean-to-peak amplitude in the depth of cut direction. Although smaller vibration amplitude is advantageous to machine a portion with a small curvature radius, the maximum structure height is essentially restricted.

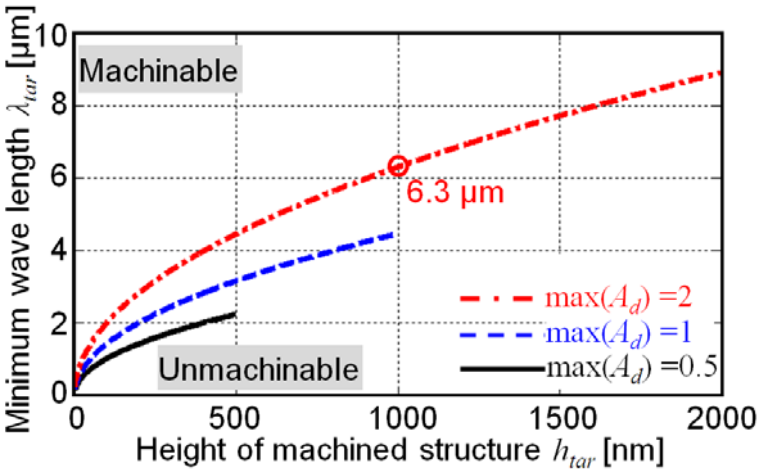

Fig. 4.4 Minimum wave length of machinable part geometry restricted by vibration amplitude conditions.

4.3.2 Influence of tool geometry

Furthermore, cutting tool geometry, i.e., the rake angle and the clearance angle, also restricts the slope of target part geometry in the nominal cutting direction. As shown in Fig. 4.5 (a), the actual rake angle defined by relative motions of the tool and the workpiece decreases in uphill machining, while avoidance of the flank face contact to the finished surface is important especially in downhill machining as shown in Fig. 4.5 (b). In order to prevent the rake/flank faces contact to the finished surface of the machined structure, the rake angle α and the clearance angle γ of the cutting edge need to satisfy the following equations at least:

$$\alpha > \max(\theta_1) - \pi/2 \tag{4-11}$$

$$\gamma > -\min(\theta_2), \tag{4-12}$$

where θ_1 is the slope angle of the target profile and θ_2 is the critical entrance angle in each vibration cycle, which can be numerically calculated by the vibration conditions [74]. θ_1 and θ_2 can be expressed as the following equations:

$$\theta_1 = \tan^{-1}\left(\frac{dz_{tar}}{dx_{tar}}\right) \tag{4-13}$$

$$\theta_2 = \tan^{-1}\left(\frac{dz_e}{d\tau} \Big/ \frac{dx_e}{d\tau}\Big|_{\tau=\tau_s}\right) = \tan^{-1}\left(\frac{A_d\omega\sin(\omega\tau_s+\varphi)}{A_c\omega\sin(\omega\tau_s)-v_c}\right), \tag{4-14}$$

where τ_s is the time when the tool starts to cut the workpiece in each vibration cycle. At the moment of $\tau=\tau_s$, tool trajectories at the present and the previous vibration cycles intersect each other.

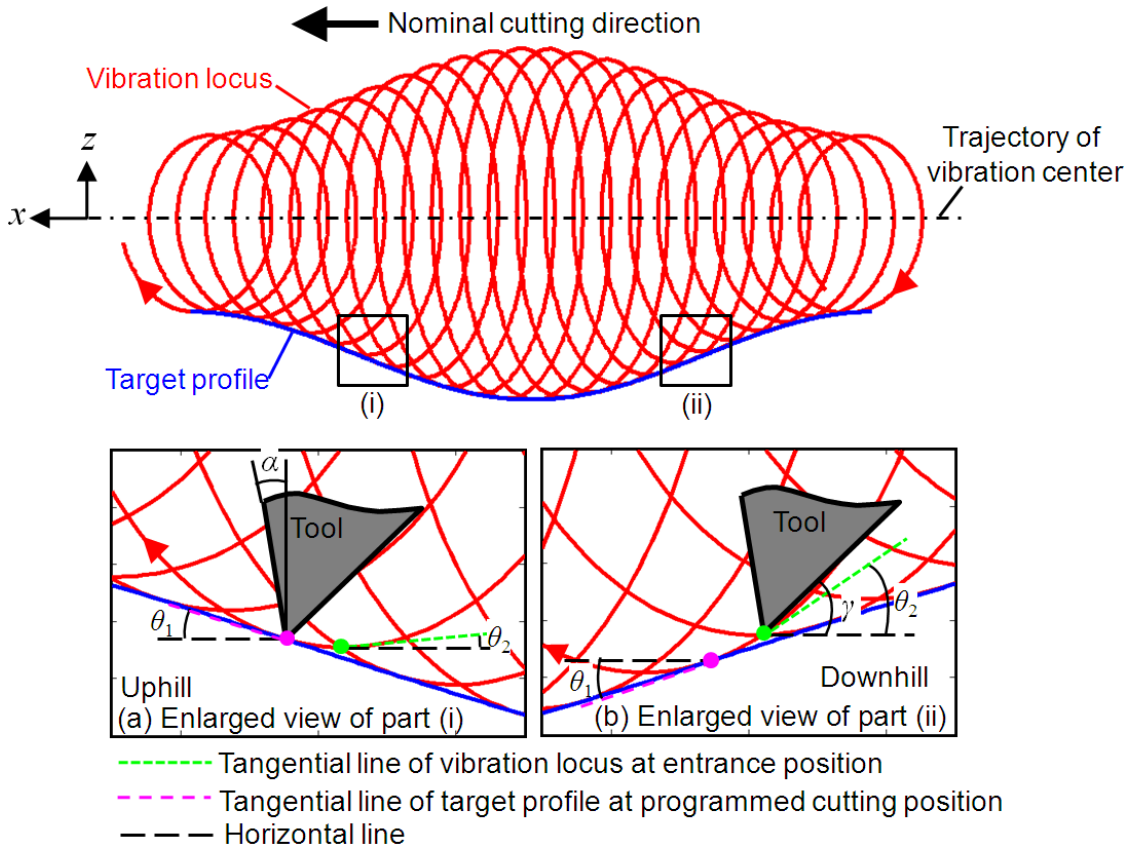

Fig. 4.5 Illustration of machinable part geometry restricted by cutting tool geometry

It should be noted that the critical entrance angle θ_2 is, in general, slightly smaller than the slope angle θ_1. In order to satisfy Eq. (4-12), the clearance angle γ needs to be larger than the negative value of the slope angle $-\theta_1$. However, a too large clearance

angle deteriorates fracture toughness of tools due to a small wedge angle. Hence, the clearance angle should be small in general. According to the practical experience, SCD tool with a rake angle of 0 deg and a clearance angle of 40 deg was available for hardened steel machining without chipping occurrence. With this tool, the structure with the maximum slope angle of around 30 deg or 35 deg may be machined avoiding the critical contact between the rake/flank faces and the machined structure.

Finally, it should be noted that the tool radius restricts the sharpness of a concave part geometry in the nominal pick feed direction, which is defined to be parallel to y axis. The curvature radius of the concave part geometry always needs to be larger than the nose radius R of the cutting tool. Hence, in order to contour the target profile using the tool with a constant nose radius, the following equation needs to be satisfied.

$$CR_{tarf} \geq R, \tag{4-15}$$

where CR_{tarf} is the curvature radius of the concave target profile in y-z plane.

Sinusoidal structure machining is also adopted to investigate the restriction of tool radius in the pick feed direction. z component of the target profile z_{tarf} is defined as a function of y component y_{tarf} in the nominal pick feed direction:

$$z_{tarf} = \frac{h_{tarf}}{2} \sin\left(\frac{2\pi y_{tarf}}{\lambda_{tarf}}\right), \tag{4-16}$$

where λ_{tarf} and h_{tarf} are the wave length and the structure height, respectively, as shown in Fig. 4.6.

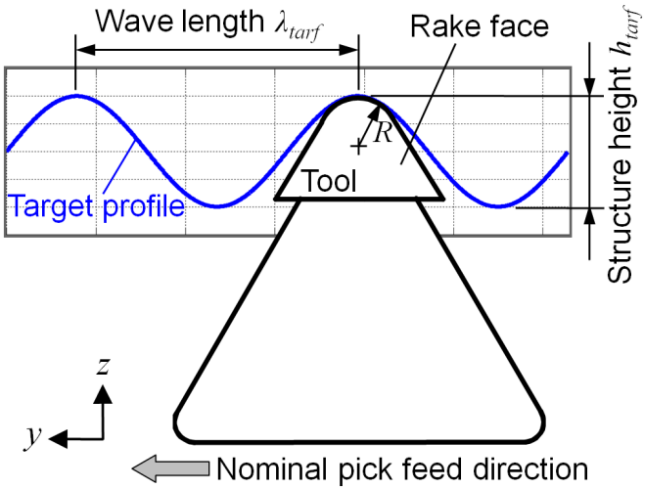

Fig. 4.6 Restriction of tool radius in nominal pick feed direction

Based on Eqs. (4-15) and (4-16), the influence of the tool radius on the machinable part geometry in the nominal pick feed direction can be expressed as:

$$\frac{\lambda_{tarf}^{2}}{2h_{tarf}\pi^{2}} \geq R. \tag{4-17}$$

With a different tool nose radius, the minimum wave length plotted against the structure height can be obtained by solving Eq. (4-17) as shown in Fig. 4.7. For instance, in order to machine a sinusoidal structure with a height of 0.5 μm, the minimum wave length is about 10 μm with a nose radius of 10 μm. A small nose radius is advantageous to machine dense patterns with a small wave length, while the pick feed needs to be small to achieve better surface roughness. Small pick feed may increase the cumulative cutting distance, resulting in longer machining time and tool wear. Hence, it may be preferable to select a large nose radius within allowable range to satisfy the curvature restriction, surface roughness, machining efficiency, and tool life simultaneously.

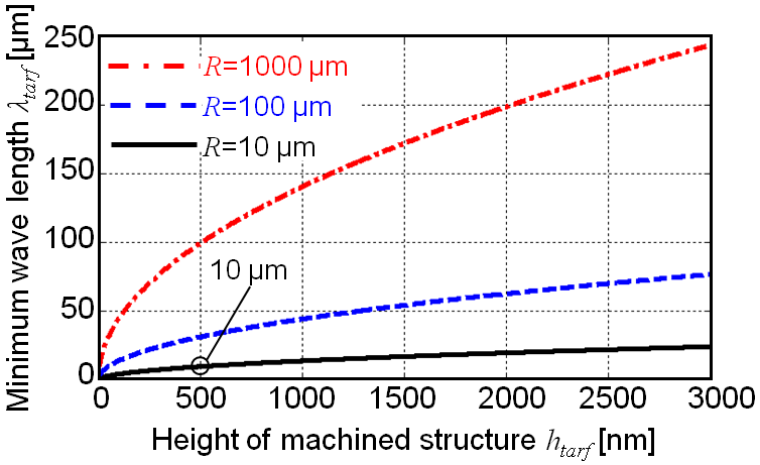

Fig. 4.7 Minimum wave length of machinable part geometry restricted by tool nose radius

4.4 Compensation of amplitude control command

4.4.1 Machining error generation

As introduced in Section 4.2, with the amplitude in the depth of cut direction being identical with the target profile, a shallow structure can be machined almost accurately

in the proposed nano sculpturing method. However, as the tool vibrates not only in the depth of cut direction but also in the nominal cutting direction, the envelope of the cutting edge trajectory becomes disagreeable with respect to the target profile. This disagreement causes serious machining accuracy deterioration especially when the slope of the target profile becomes steep. Figure 4.8 shows a schematic illustration of the machining error generation, where the amplitude in the depth of cut direction agrees with the target profile in the amplitude control sculpturing method. As the target profile traces the bottom of each tool vibration, the workpiece is overcut resulting in machining accuracy deterioration.

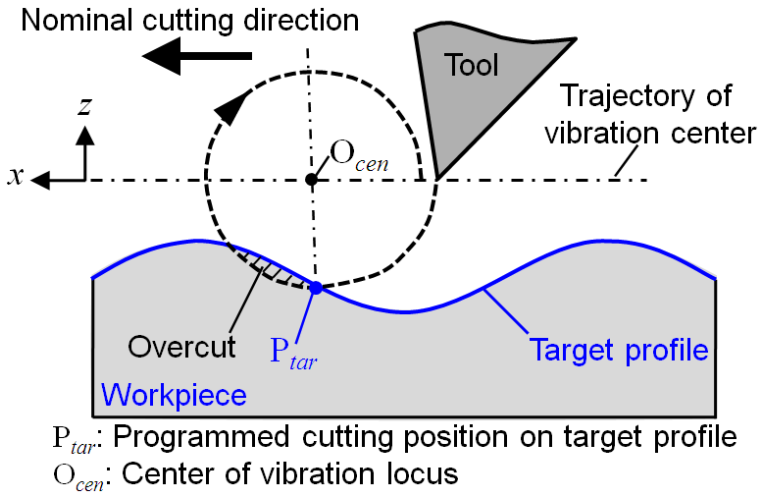

Fig. 4.8 Illustration of the machining error generation

The amount of the machining error is quantitatively investigated. Figure 4.9 shows a verifying target profile of the sine sweep structure, where the structure height is 1 μm and the wave length is decreased from 31.62 μm to 6.75 μm. Note that the tool is fed toward the right in Fig. 4.9. The mean-to-peak amplitude in the depth of cut direction varies sinusoidally in 1-2 μm to machine this structure, while the mean-to-peak amplitude in the nominal cutting direction is fixed to 2 μm. The wave length of the verifying target profile is larger than the machinable minimum wave length, i.e., 6.3 μm with a structure height of 1 μm, as shown in Fig. 4.4. In other words, the target shape is machinable by considering the restrictions of vibration conditions. The profile of the

target shape can be defined by the following equations:

$$z_{tar}=\begin{cases} 0 & (x_{tar}<0,\ 77.4<x_{tar}) \\ \frac{1}{2}\left(1-\cos\left(0.002\pi x_{tar}{}^2\right)\right) & (0\leq x_{tar}\leq 77.4) \end{cases}. \tag{4-18}$$

Then, the slope angle of the target profile can also be obtained as Fig. 4.9 shows.

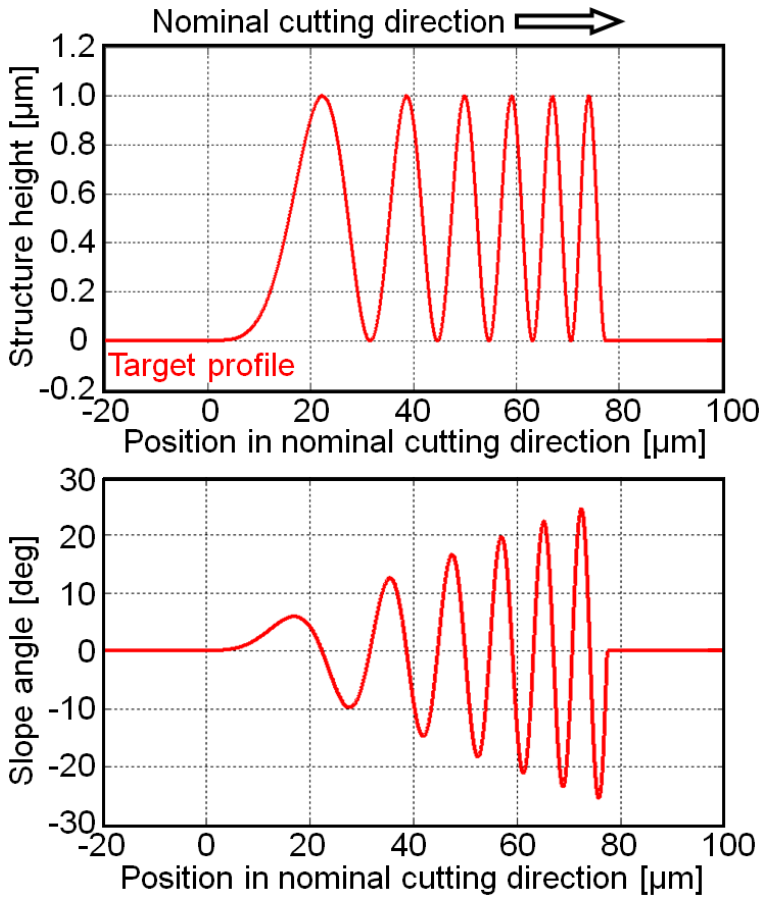

Fig. 4.9 Profile and slope angle of designed target shape

Figure 4.10 demonstrates the cutting edge trajectory and the simulated machining error, i.e., form deviation, in the target shape machining. It should be noted that the elliptical vibration frequency is assumed as 36.2 kHz, and the undulation due to each vibration is negligible small. However, a nonnegligible error between the amplitude command (target shape) and the machined geometry (envelope of vibration locus) is generated. The machining error increases up to 0.235 μm as the wave length decreases, as shown in Fig. 4.10. This simulation process confirms that the envelope of

the cutting edge trajectory becomes shallow with respect to the command wave especially when the ratio of structure height to wave length becomes larger. This overcut causes serious machining accuracy deterioration.

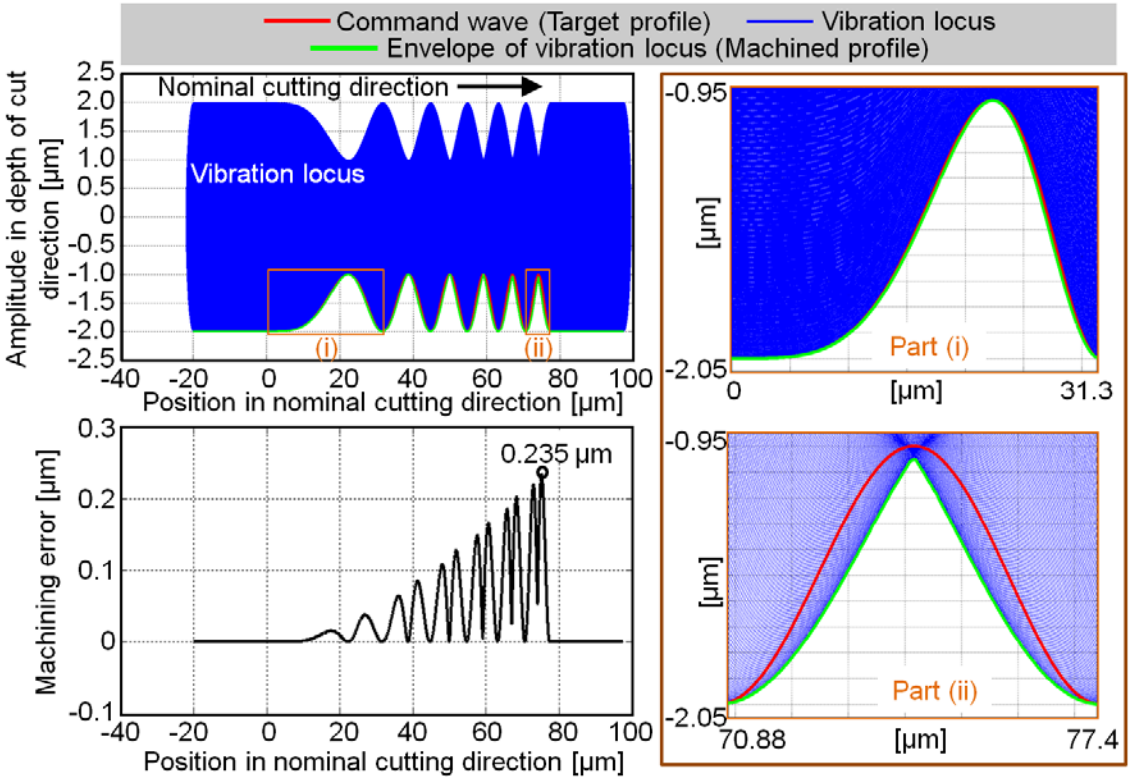

Fig. 4.10 Cutting edge trajectory and machining error generation with different ratio of structure height to wave length

4.4.2 Principal of proposed command compensation method

In order to cancel out this machining error, the amplitude command in the depth of cut direction needs to be modified. Figure 4.11 shows a schematic illustration explaining concept of the command compensation method. In each vibration cycle, the vibration locus is controlled to be tangential to the target profile. $O_{cen}(x_{cen}, z_{cen})$ is considered as the center position of the vibration locus in machining target position $P_{tar}(x_{tar}, z_{tar})$. Then, the elliptical vibration vector is obtained as following:

$$\vec{E}=P_{tar}-O_{cen}=(A_c\cos(\varepsilon), A_d\cos(\varepsilon+\varphi)), \quad (4\text{-}19)$$

where ε is the phase of elliptical vibration at the tangential moment, as defined in

Section 4.3. The unit tangential vector $\overrightarrow{t_{tar}}$ of the target profile can be calculated by:

$$\overrightarrow{t_{tar}}=\left(\cos\left(\tan^{-1}\frac{dz_{tar}}{dx_{tar}}\right),\sin\left(\tan^{-1}\frac{dz_{tar}}{dx_{tar}}\right)\right). \tag{4-20}$$

As the tool path with elliptical vibration is expressed in Eq. (4-1), the tangential direction $\vec{t}_e$ (unit vector) of the vibration locus is also formulated by:

$$\vec{t}_e=\left(\cos\left(\tan^{-1}\frac{dz_e}{dx_e}\right),\sin\left(\tan^{-1}\frac{dz_e}{dx_e}\right)\right), \tag{4-21}$$

where the ratio of dz_e/dx_e can be given by:

$$\frac{dz_e}{dx_e}=\frac{dz_e/d\tau}{dx_e/d\tau}=\frac{A_d\omega\sin(\omega\tau+\varphi)}{A_c\omega\sin(\omega\tau)-v_c}. \tag{4-22}$$

The vector $\vec{t}_e$ needs to be parallel to the vector $\overrightarrow{t_{tar}}$ at the intersection position, i.e., position P_{tar}. Therefore, the following equations need to be satisfied at the tangential moment.

$$\overrightarrow{t_{tar}}=\vec{t}_e,\ \mathrm{P}_{tar}=\mathrm{P}_e. \tag{4-23}$$

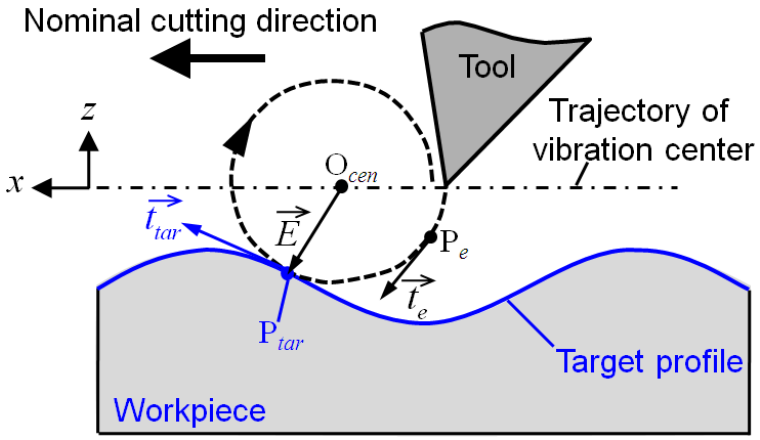

Fig. 4.11 Proposed command compensation method

Considering Eqs. (4-20, 4-21, 4-22 and 4-23), a compensated command for amplitude control can be calculated. Figure 4.12 shows the flow chart for determining the compensated reference data for amplitude control. The compensation is processed in a discrete domain, and the counter of discrete data n is defined, e.g., the n-th target position is defined as $\mathrm{P}_{tar,n}(x_{tar,n},\ z_{tar,n})$. Firstly, initial values of the vibration center position $\mathrm{O}_{cen,n}(x_{cen,n},\ z_{cen,n})$ and the vibration amplitudes $A_{c,n}$ and $A_{d,n}$ are given. Assuming

$z_{tar,n}=z_{e,n}$, the elliptical vibration phase ε is calculated. With the obtained ε, tangential vectors $\overrightarrow{t_{tar,n}}$ and $\overrightarrow{t_{e,n}}$ are compared. Modifying the amplitudes $A_{c,n}$ and $A_{d,n}$, optimal amplitudes satisfying $\overrightarrow{t_{tar,n}} = \overrightarrow{t_{e,n}}$ are computationally calculated at the target position $\mathrm{P}_{tar,n}(x_{tar,n},\ z_{tar,n})$. From the obtained phase and amplitudes, the corresponding vibration center position $\mathrm{O}_{cen,n}(x_{cen,n},\ z_{cen,n})$ and process time $\tau_n(=x_{cen,n}/v_c)$ are updated. Finally, by means of interpolation of obtained amplitudes and process time, the compensated reference data for amplitude control are determined.

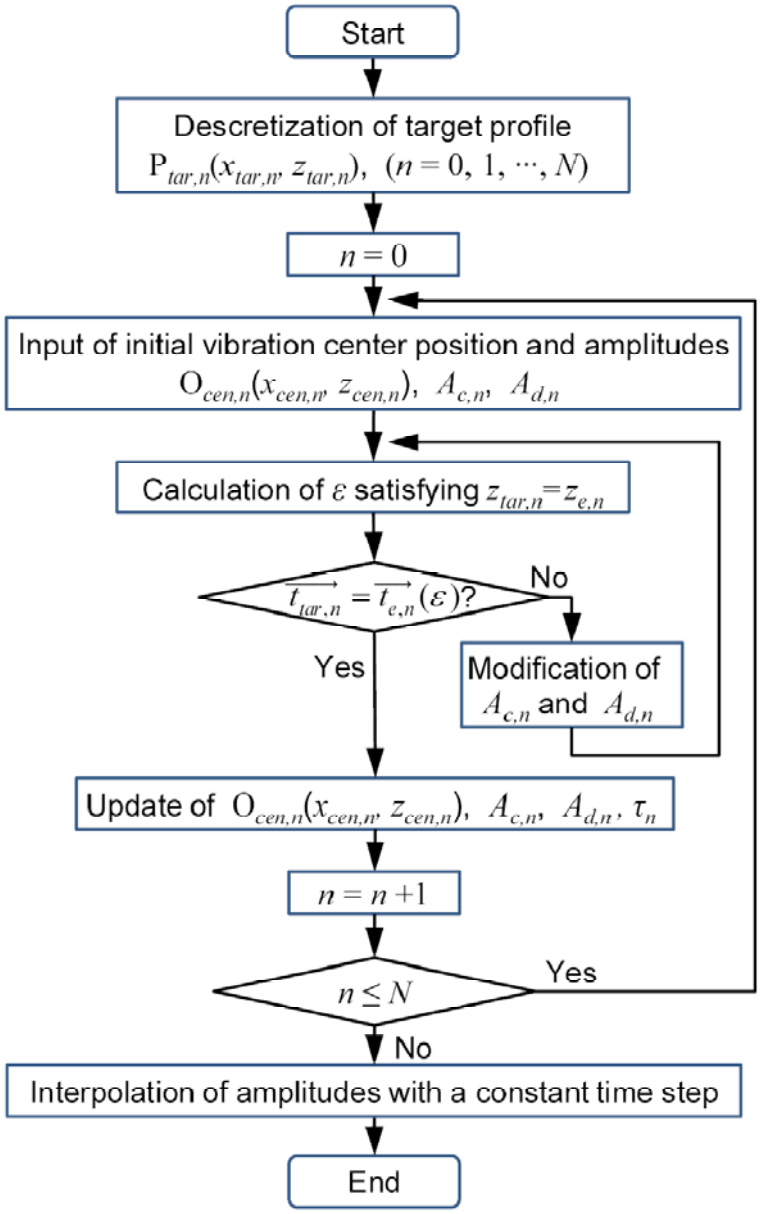

Fig. 4.12 Flow chart of amplitude command compensation

Fig. 4.13 demonstrates each calculation step. A sinusoidal structure machining with a structure height of 1 μm and a wave length of 10 μm is taken as an example. The amplitude in the cutting direction keeps in a stable value of 2 $\mu m_{0\text{-}p}$ and the maximum amplitude in the depth of cut direction is also 2 $\mu m_{0\text{-}p}$.

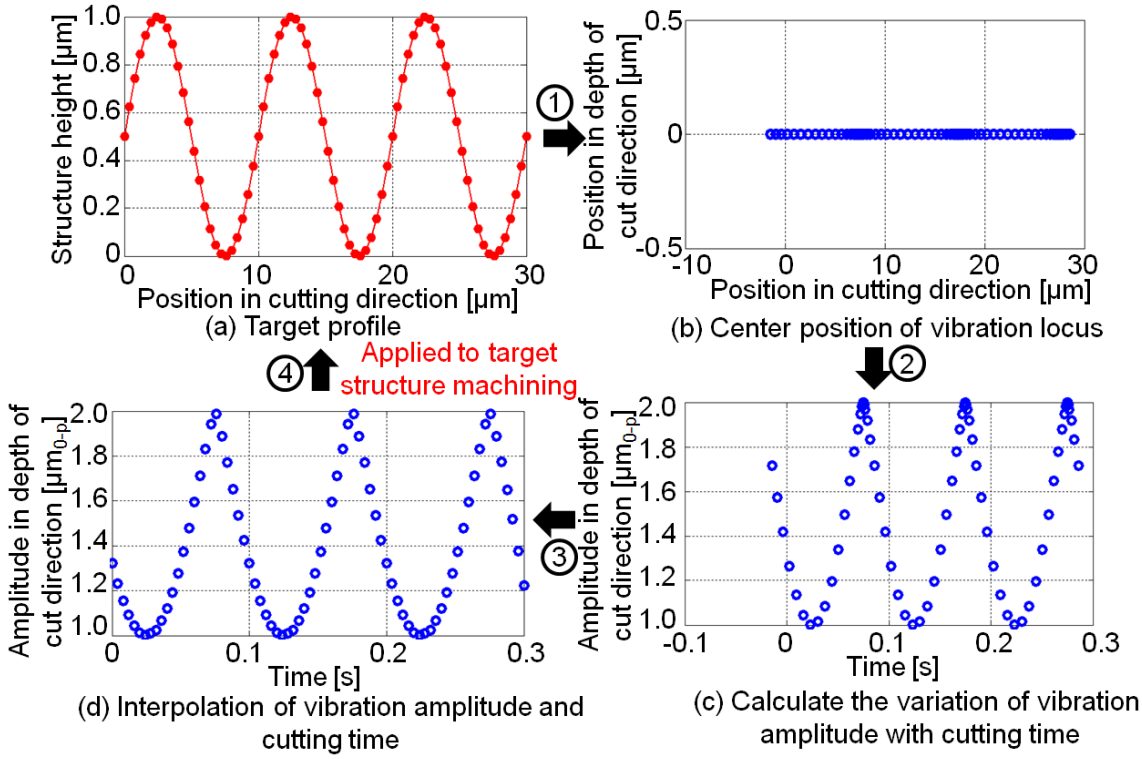

Fig. 4.13 Simulation process in indicating the center position of vibration locus and the compensated vibration amplitude in the depth of cut direction

With the proposed command compensation method, Figure 4.14 demonstrates a compensated vibration locus in machining of the same target profile as illustrated in Fig. 4.9. As comparing with the simulated results without amplitude compensation in Fig. 4.10, the envelope of the tool trajectory is accurately identical with the ideal target profile by applying the proposed command compensation method.

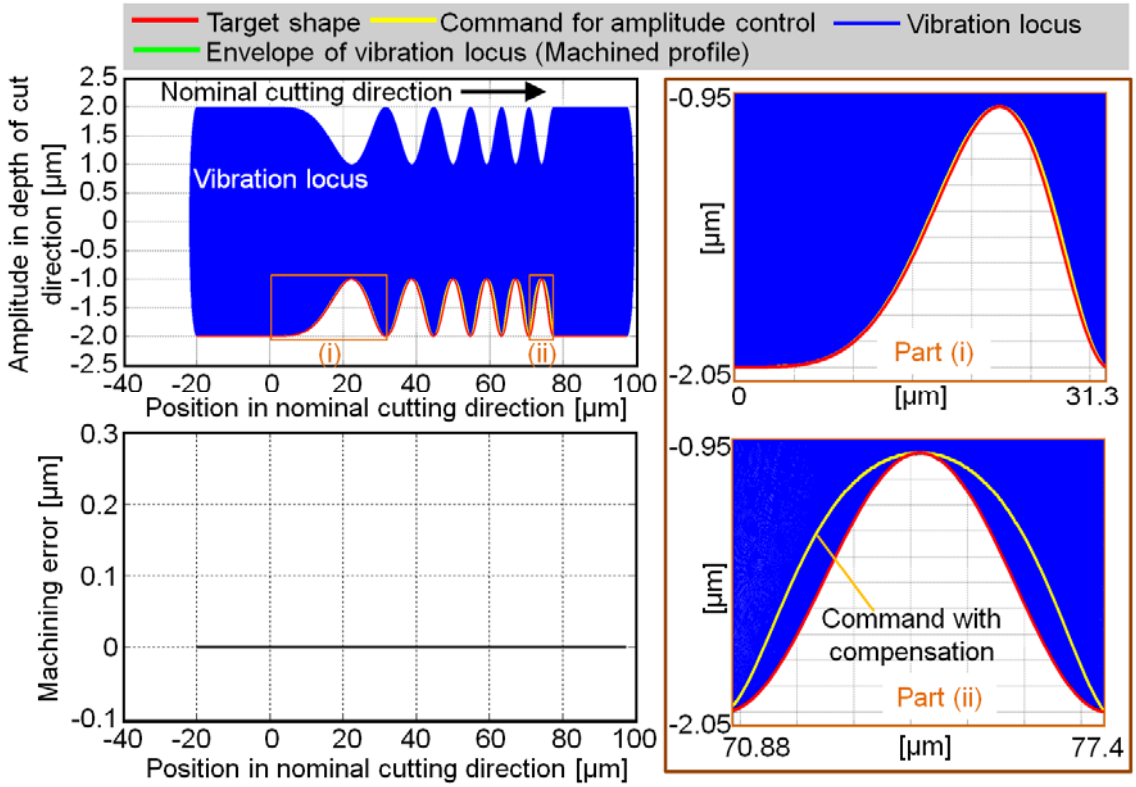

Fig. 4.14 Cutting edge trajectory with proposed command compensation method

4.5 Summary

In this chapter, machining performance of the amplitude control sculpturing technology at micro/nano scale was investigated by utilizing elliptical vibration cutting. A series of analytical investigations were conducted to investigate the machinable part geometry essentially restricted by vibration conditions and tool geometry. As the tool vibrates not only in the depth of cut direction but also in the cutting direction, the envelope of the cutting edge trajectory becomes disagreeable with respect to the target profile. This disagreement causes serious machining accuracy deterioration especially when the ratio of structure height to wave length becomes large. Therefore, a command compensation method for decreasing the machining error, which is caused by the disagreement of the amplitude command shape and the envelope of the cutting edge trajectory, was proposed. A verifying target profile of the sine sweep structure was assumed, where the structure height is 1 μm and the wave length is decreased from 31.62 μm to 6.75 μm. Without the command compensation, the maximum machining error increases up to 0.235 μm. As a comparison, the envelope of the tool trajectory is

accurately identical with the ideal target profile by applying the proposed command compensation method. Based on the simulation analysis, it was confirmed that the proposed compensation method can be untilled for improving the machining accuracy significantly.

Chapter 5

Highly-accurate micro/nano structure fabrication

5.1 Introduction

In order to clarify the restrictions in machinable part geometry by applying the proposed amplitude control sculpturing method, theoretical investigations are conducted in Chapter 4. Subsequently, a compensation method of vibration amplitude command for highly-accurate machining is also proposed. To verify the feasibility of aforementioned results obtained in theoretical investigations, experimental investigations are conducted in this chapter. Hardened steel is adopted as the workpiece material in the experimental verifications. Through a series of experimental investigations, machining performance of the amplitude control sculpturing method is investigated. Accurate nano sculpturing was also verified by applying the amplitude control commands with trapezoidal, sinusoidal, zigzag, and ramp waves. In order to verify the feasibility of highly-accurate micro/nano structure fabrication, the proposed sculpturing method is finally applied to the machining of a sophisticated three-dimensional grid surface. The research results presented in this chapter are also presented in the author's published papers [110, 111]. With the detailed theoretical and experimental analysis of the proposed sculpturing method, it is expected to be guidance for the future applications of the steel and tungsten carbide sculpturing.

5.2 Experimental setup

Figure 5.1 illustrates the elliptical vibrator and the high-speed amplitude control system. The vibrator can be actuated by exciting PZT actuators that are sandwiched with metal cylindrical parts. As a result, a two-degree-of-freedom (2-DOF) elliptical vibration can conveniently be obtained at the diamond tool tip at a frequency of about 36.2 kHz. The gain of the amplifier can be controlled by external input in the developed system, and thus the exciting voltage supplied to the actuator is changed. The

amplitude is, consequently, controlled by the external input as shown in Fig. 5.1. Mean-to-peak vibration amplitudes can be controlled arbitrarily within 0-2 μm.

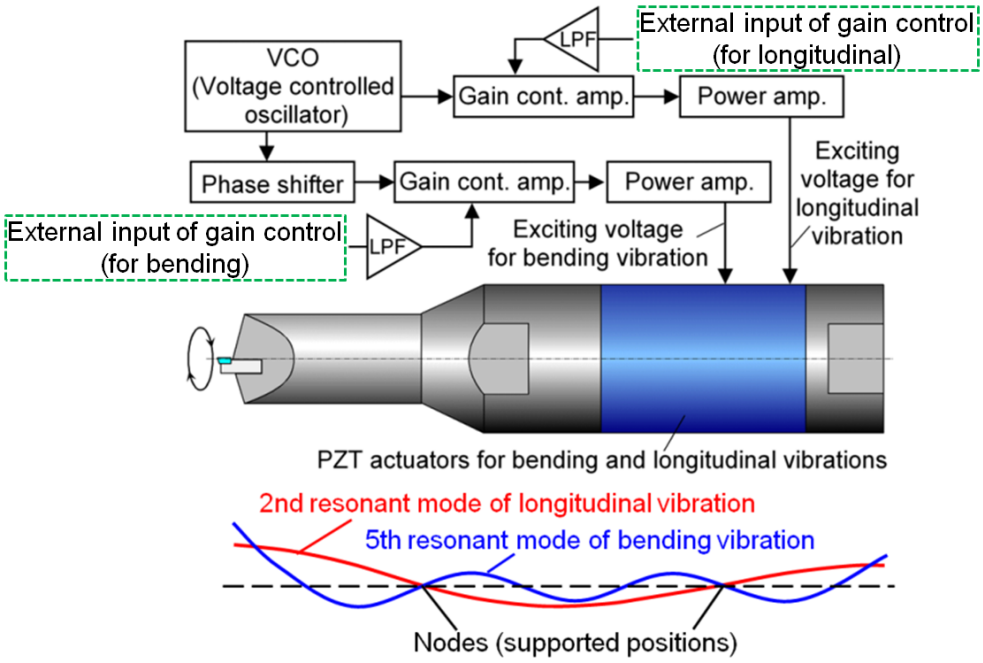

Fig. 5.1 Two-degree-of-freedom elliptical vibration tool with external input [62]

In the developed system, measured frequency response of amplitude control is shown in Fig. 5.2 [62].

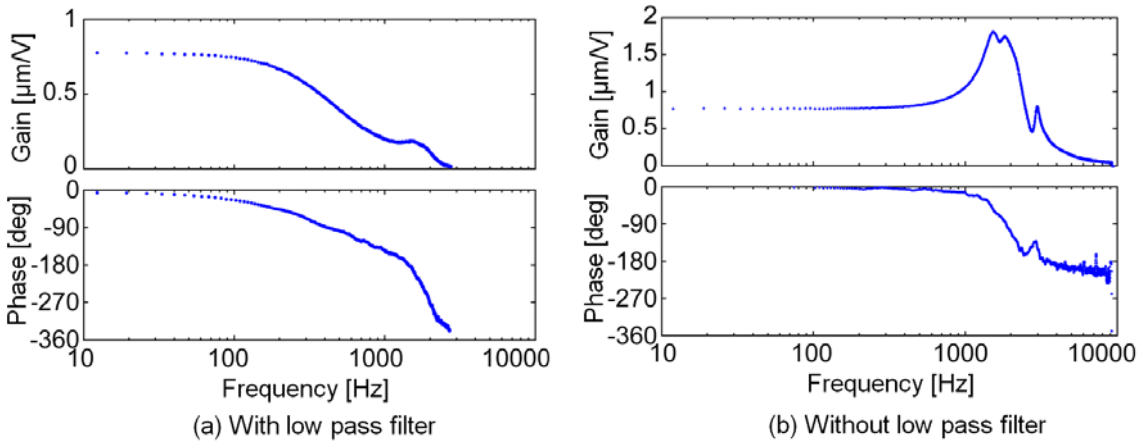

Fig. 5.2 Frequency response of amplitude control [62]

When the external input is supplied without passing through the low pass filter (LPF), dynamic gain is enlarged at a frequency of about 1.5 kHz as compared with static gain. In order to suppress this high dynamic gain, a second-order LPF is placed in the practical system, which is still able to control the vibration amplitude within a frequency bandwidth of about 300 Hz. This frequency bandwidth is relatively narrow as compared with that of conventional FTS. However, it might not be a big problem due to the relatively low nominal cutting speed in elliptical vibration cutting (EVC) technology.

The proposed amplitude control sculpturing method is applied to texture surface machining, where the vibration amplitude is controlled in synchronization with the planing motion of an ultra-precision machine tool. Figure 5.3 shows the experimental setup. The ultra-precision machine tool, ASP01UPX made by Nachi-Fujikoshi Corp., is used. The 2-DOF elliptical vibrator was attached to the X axis table. The vibration amplitude in the depth of cut direction along the Z axis is controlled in synchronization with the cutting feed motion in the X axis. The X feed position is detected by using an external optical sensor (Keyence FU-10) in each stroke, and a high-speed real-time control system (dSPACE) outputs the vibration amplitude command in synchronization with the X axis feed.

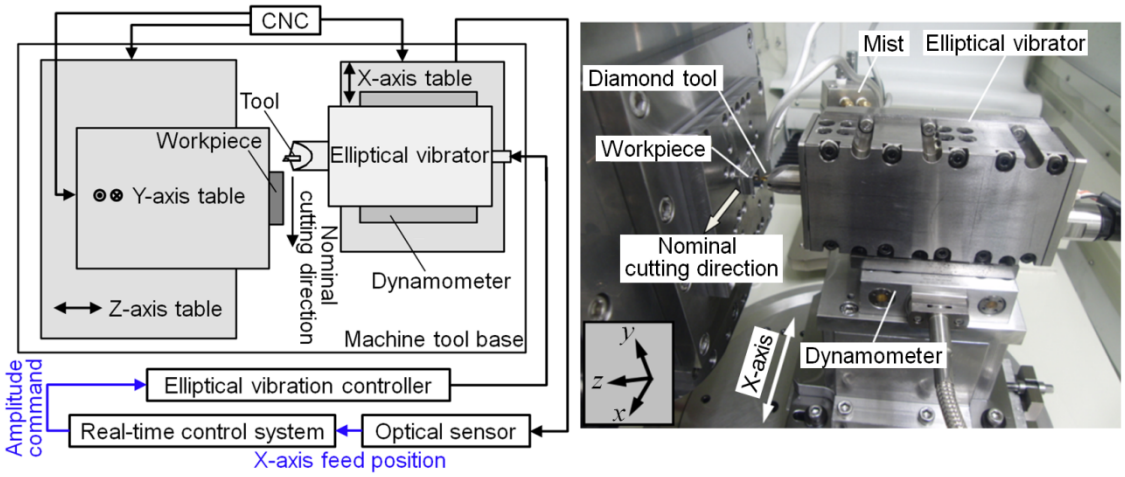

Fig. 5.3 Illustration and view of experimental setup in micro/nano structure machining

5.3 Investigation of machining accuracy

In order to investigate machining accuracy on hardened steel (JIS: SUS420J2, UTS≥540 MPa, HRC53) by the proposed sculpturing method, nano structures were machined with trapezoidal amplitude command waves at 100 Hz. A structure height of trapezoidal command was controlled to change a depth of cut from 1 nm to 20 nm, and a pitch of the trapezoidal structures was set to be 7 μm. The machine tool is simply controlled to machine a plane surface in xy plane with a pick feed of 5 μm at a constant feed speed of 42 mm/min. The vibration amplitude in the depth of cut direction along Z axis is controlled in synchronization with the cutting feed in X axis. Then, the trapezoidal structures perpendicular to X axis were machined. Fig. 5.4 shows the experimental results. The machining surface was measured by using atomic force microscope (AFM). As shown in Fig. 5.4, nano structures with a designed structure height of 1 nm are marginally distinctive from the machined hardened steel surface.

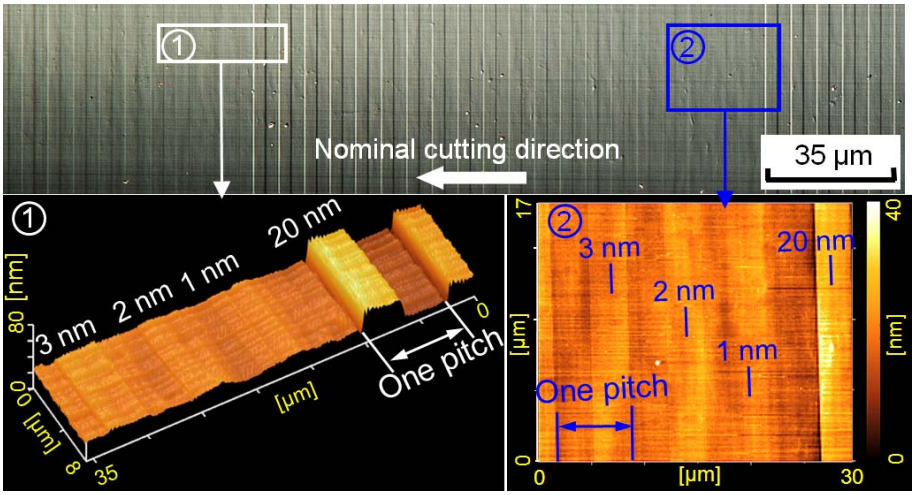

Fig. 5.4 Optical Nomarski microphotograph and AFM images of machined trapezoidal structures

Machining accuracy of trapezoidal steps was investigated from the measured geometry. In order to distinguish machining error due to the machine tool motion control, average machining height was analyzed. Note that the motion error of the machine tool is not negligible in single-nano scale. Figure 5.5 shows relationships between step

height commands and measured step heights. The error bar indicates standard deviation (±1σ) of the measured heights, which represents height variation. From the measured results, the nano structure with a machining accuracy of about ±1 nm can be machined in the depth of cut direction.

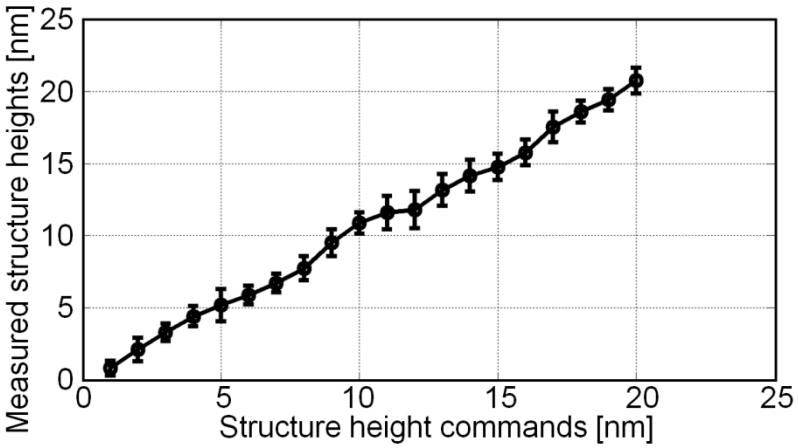

Fig. 5.5 Measured structure heights

5.4 Verification of amplitude compensation method

The proposed command compensation method was subsequently applied to the target shape machining as illustrated in Fig. 4.9 of Chapter 4. Experimental conditions are summarized in Table 5.1.

Table 5.1: Experiment conditions for target shape machining

Cutting conditions	Nominal cutting speed [mm/min]	6
	Pick feed [μm]	5
	Maximum depth of cut [μm]	5
	Cutting fluid	Oil mist (PS-FM-A)
Vibration conditions	Frequency [kHz]	36.2
	Phase shift [deg]	-90
	Amplitude in depth of cut direction [$\mu m_{0\text{-}p}$]	1-2
	Amplitude in nominal cutting direction [$\mu m_{0\text{-}p}$]	2
Tool	Material	Single crystal diamond
	Nose radius [mm]	1
	Rake angle [deg]	0
	Clearance angle [deg]	30
Workpiece	Hardened steel	SUS420J2 (HRC53)

The maximum slope angle of the target profile is calculated as 25.44 deg. Based on the cutting and vibration conditions, the maximum absolute value of the entrance angle is obtained as 25.48 deg, which is slightly larger than the maximum slope angle 25.44 deg of target profile. Based on Eqs. (4-11) and (4-12) in Chapter 4, the clearance angle and the rake angle of the cutting tool need to be larger than 25.48 deg and -64.56 deg, respectively. Hence, a tool with a clearance angle of 30 deg and a rake angle of 0 deg was utilized here to prevent the rake/flank face contact to the machined target shape.

The machined surfaces were subsequently measured by using an atomic force microscope (AFM). Figure 5.6 (a) shows the machining result without the command compensation, where the target and the measured profiles and machining error are presented. The overcut causes serious machining accuracy deterioration especially when the ratio of structure height to wave length becomes large. Due to the overcut, smooth target shape is deteriorated into the serrated wave as well as that simulated in Fig. 4.10 of Chapter 4. On the other hand, Fig. 5.6 (b) shows the target structure machined by the proposed command compensation method. The total machining error is decreased significantly from 242.5 $nm_{p\text{-}v}$ to 22.4 $nm_{p\text{-}v}$. Through the experimental verifications, it was confirmed that the proposed command compensation method is useful to prevent the machining accuracy deterioration due to the overcut. Even though the proposed command compensation method was applied for target structure machining, there still is a maximum machining error of 22.4 $nm_{p\text{-}v}$. The tool edge deterioration is assumed as one of the factors causing machining error generation in nano scale machining.

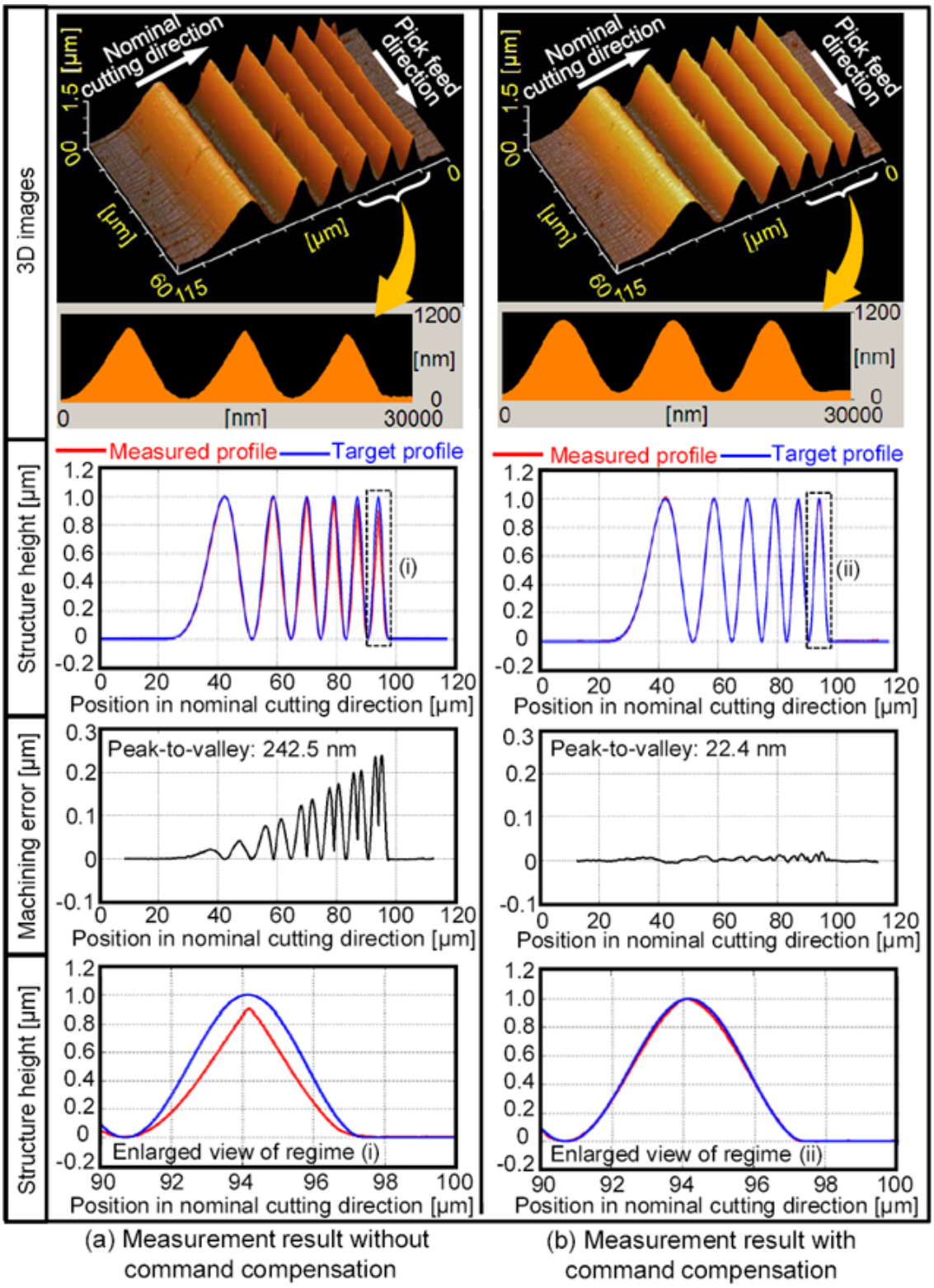

Fig. 5.6 Experimental machining of target structure (a) without/ (b) with command compensation

Regarding the proposed sculpturing process, the tool edge is assumed to be perfectly sharp. However, the tool edge radius of single crystal dianmond tools is usually in tens of nanometers or more than that. For example, part of the used tool edge is measured by the AFM after the experiments. In advance of the measurement, the diamond tool is cleaned with acetone carefully. Subsequently, the tool is vertically placed beneath the AFM probe, as shown in Fig. 5.7. Figure 5.8 shows a measurement result of the used cutting edge, where the edge radius r is about 180 nm. As the edge radius of the tool is considered to be slightly larger than that of brand-new tool, this less sharpness may have a certain influence on the machining accuracy deterioration in nano scale machining.

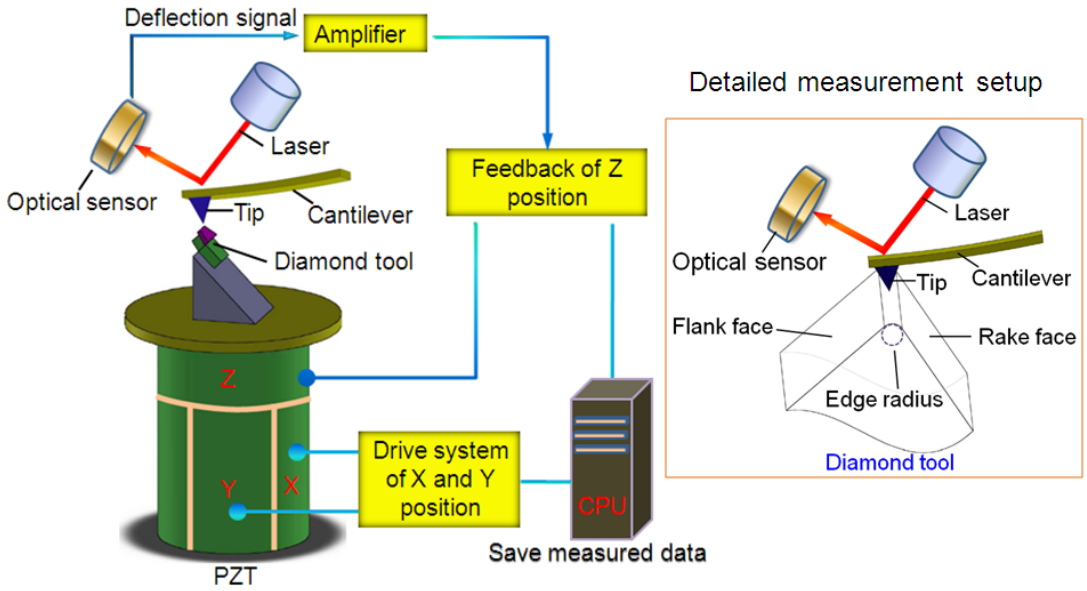

Fig. 5.7 Schematic diagram of the measurement method to obtain tool edge radius

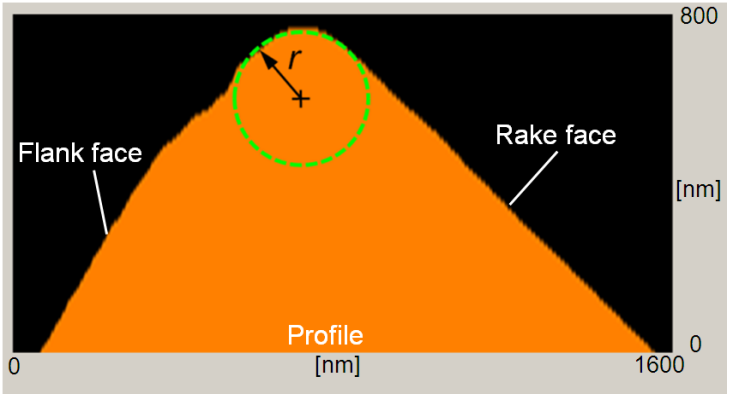

Fig.5.8 Geometry of used tool edge measured by AFM

Figure 5.9 illustrates a kinematic model of the surface generation considering a round tool edge. Although the cutting tool is controlled to move through the compensated profile of A-B-C-D-E, the envelope of the round tool edge, which generates the finished surface profile, passes along A-B'-C-D'-E, resulting in a machining error generation as shown in Fig. 5.9. Moreover, elastic deformation of the machined structure may enhance the machining accuracy deterioration.

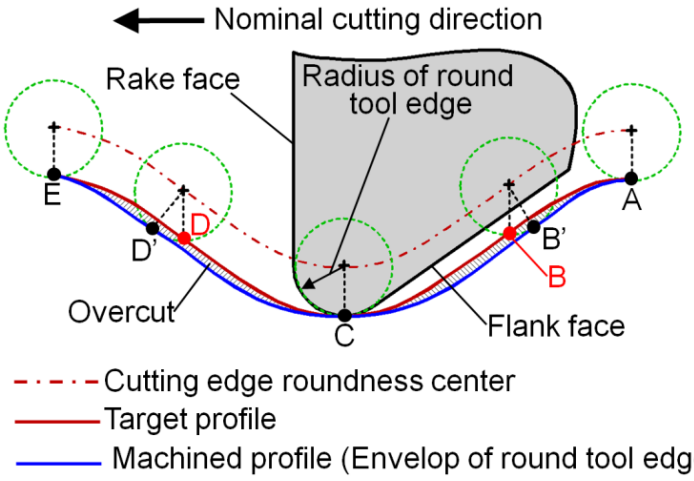

Fig. 5.9 Illustration of surface generation considering the round tool edge

5.5 Verification of tool geometry restriction on machinable part geometry

In what follows, the restriction of tool geometry on machinable part geometry is also evaluated. In this section, machining error caused by the interference between the tool flank face and the machined target shape is investigated. As introduced in Section 5.4, the maximum critical entrance angle θ_2 is calculated as 25.48 deg when sculpturing the target profile. Meanwhile, a tool with a clearance angle of 15 deg and a rake angle of 0 deg was utilized here to investigate the flank face contact to the target shape. Figure 5.10 shows the simulated trajectory of the tool flank face and the machining error. Due to insufficient clearance angle, large machining error between the target shape and the machined geometry is generated. The maximum machining error increases up to 279 nm with increase of the slope angle of target profile, as shown in Fig. 5.10. The interference between the flank face and machined structure may cause not only serious machining accuracy deterioration but also tool damage.

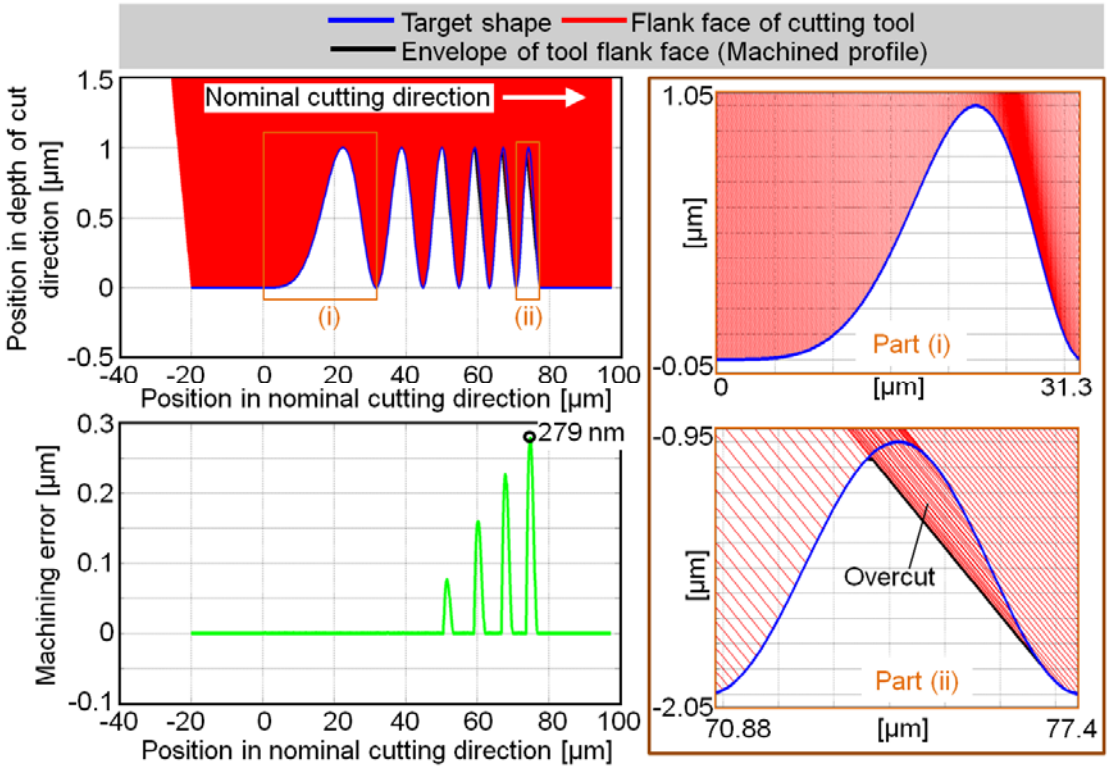

Fig. 5.10 Trajectory of flank face and machining error generation due to flank face contact to the target shape

The target profile is machined with the proposed command compensation method. The machined surfaces were subsequently measured by using an atomic force microscope (AFM) as shown in Fig. 5.11. The evaluated position is from 65 μm to 77.4 μm in the nominal cutting direction as shown in Figure 5.10. It seems that the machined shape is almost identical with the simulated envelop of tool flank face, which also verifies the flank face contact to the target shape.

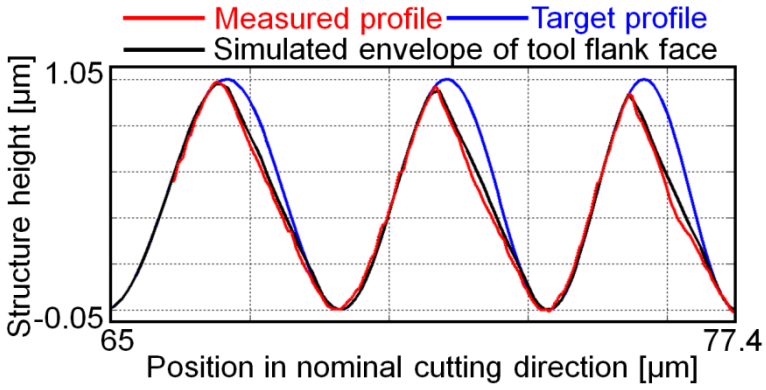

Fig. 5.11 Comparison of measurement result with simulated result

Figure 5.12 shows the machining results with the clearance angle of 15 deg and 30 deg, where the target and the measured profiles and machining error are presented.

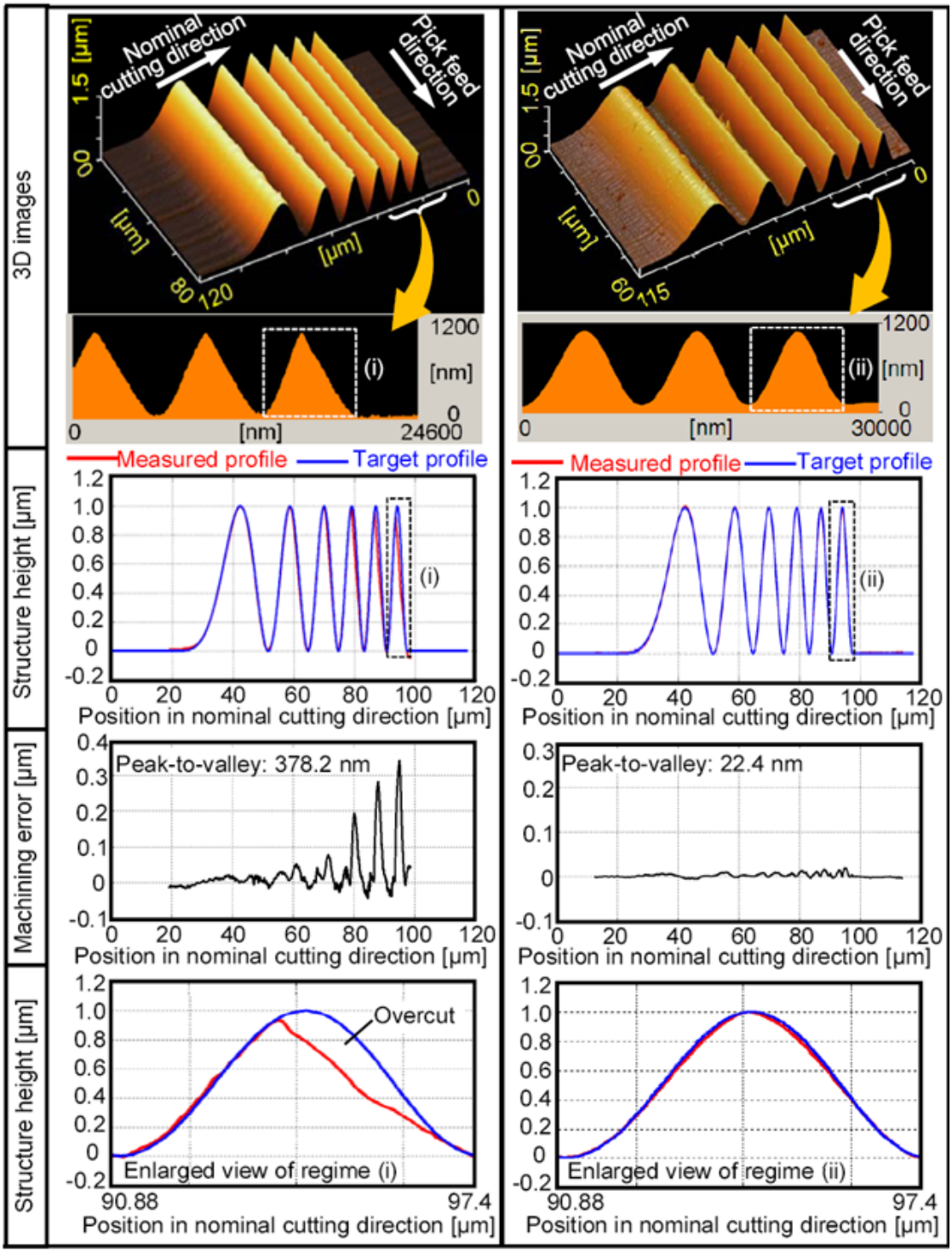

(a) Measurement result with interference (clearance angle: 15°)

(b) Measurement result without interference (clearance angle: 30°)

Fig. 5.12 Machine error generation caused by flank face contact to the finished surface

The overcut causes serious machining accuracy deterioration when the slope angle of target profile becomes large as shown in Fig. 5.12 (a). Due to the overcut, smooth target shape is deteriorated into the serrated wave as well as that simulated in Fig. 5.10. On the other hand, Fig. 5.12 (b) shows the target structure machined by the diamond tool with a clearance angle of 30 deg. The maximum machining error is about 378.2 nm_{p-v} when the flank face contacts to the target profile.

As compared with the simulated value in Fig. 5.10, the maximum machining error becomes larger in the experimental verification. Because of the contact between the flank face and the machined structure, large edge force may generate in the cutting process. The geometry of fabricated structure may be deteriorated due to this increase of the cutting forces. Consequently, the plastic deformation of the fabricated structure may increase the machining error. Through the experimental verifications, it was confirmed that the avoidance of flank face contact to the machined structure is much important in micro/nano structure machining.

After the experiments, the tool wear was observed by using an optical microscope. The optical micrographs of tool edge after the experiments were shown in Fig. 5.13.

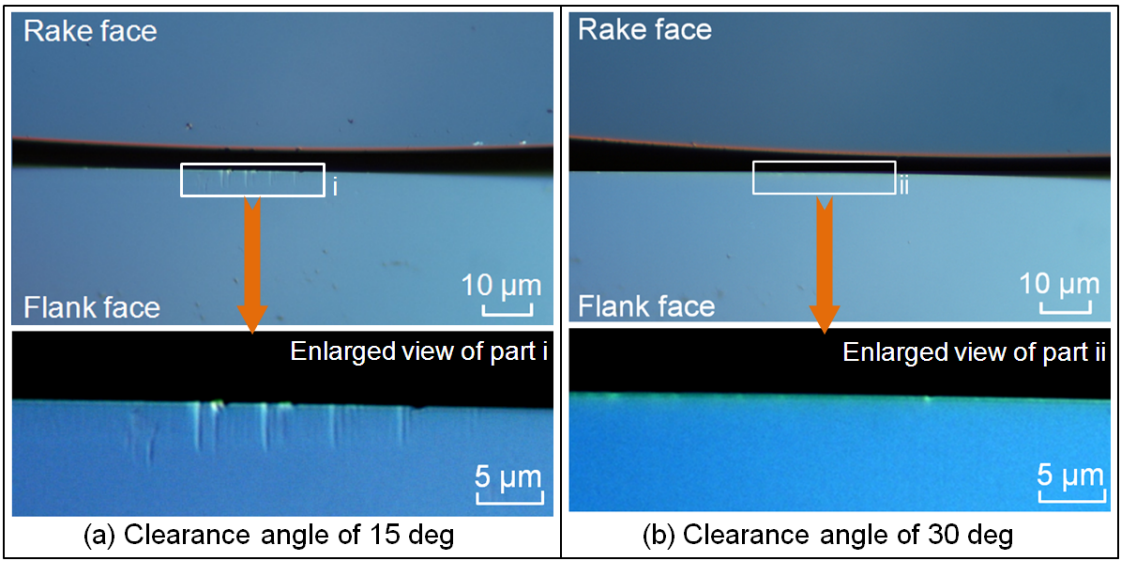

(a) Clearance angle of 15 deg (b) Clearance angle of 30 deg

Fig. 5.13 Optical micrographs of tool edge (a) with/ (b) without flank face contact with target shape

It should be noted that the scratching mark on the flank face is obvious on the flank face when interference occurs between the tool flank face and the target shape. The flank face contact enhances the ploughing process, resulting in the increase of friction force and adhesion between the workpiece and the diamond tool. And thus, the thermo-chemical wear may become more serious. On the other hand, no obvious scratching was observed in the SCD tool with a clearance angle of 30 deg.

5.6 Applications of elliptical vibration sculpturing method

5.6.1 Feasibility of nano structure machining

Several nano patterns were machined with a steady amplitude commands at 100 Hz in this section. In order to avoid the flank face contact to the workpiece surface, the slope of amplitude change in elliptical vibration cutting needs to be less than the clearance angle of the cutting edge at least. Fig. 5.14 shows a trapezoidal structures machined by the amplitude corresponding to 25 nm structure height with a pitch value of 2 μm. The fabricated patterns were measured by using the atomic force microscope and the optical microscope, respectively. As the slope of the trapezoidal structure was kept to 30 deg, the tool with a clearance angle of 40 deg was utilized here. In what follows, textured grooves with a 20 nm structure height were also sculptured on a hardened steel workpiece, and feasibility of nano structure sculpturing was investigated.

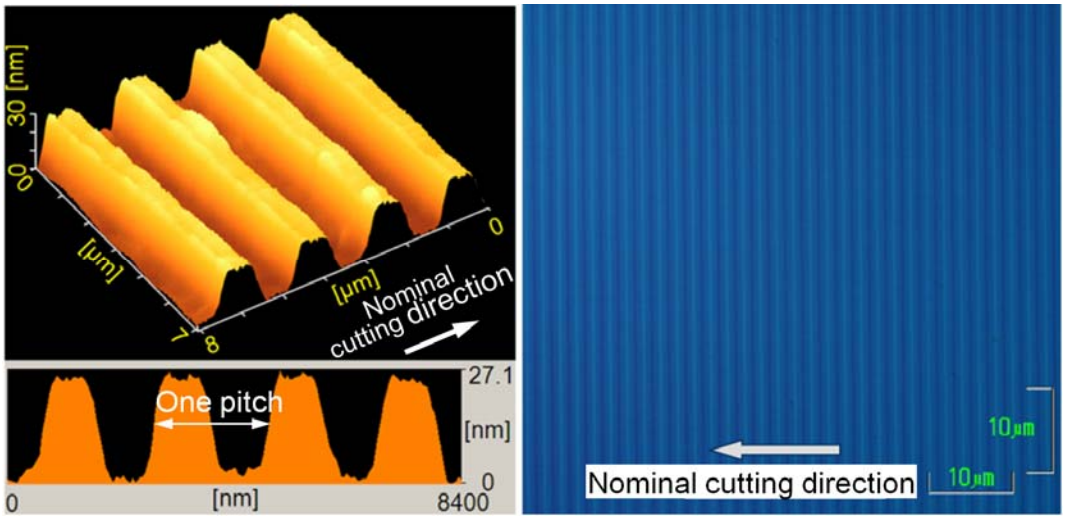

Fig. 5.14 Trapezoidal structures with structural height of 25 nm and pitch of 2 μm

Figure 5.15 shows several textured grooves with different patterns, i.e., sinusoidal, zigzag and ramp waves, with a steady amplitude command at 100 Hz. The fabricated patterns were measured by using the atomic force microscope and the scanning electron microscope, respectively. Experimental conditions are summarized in Table 5.2.

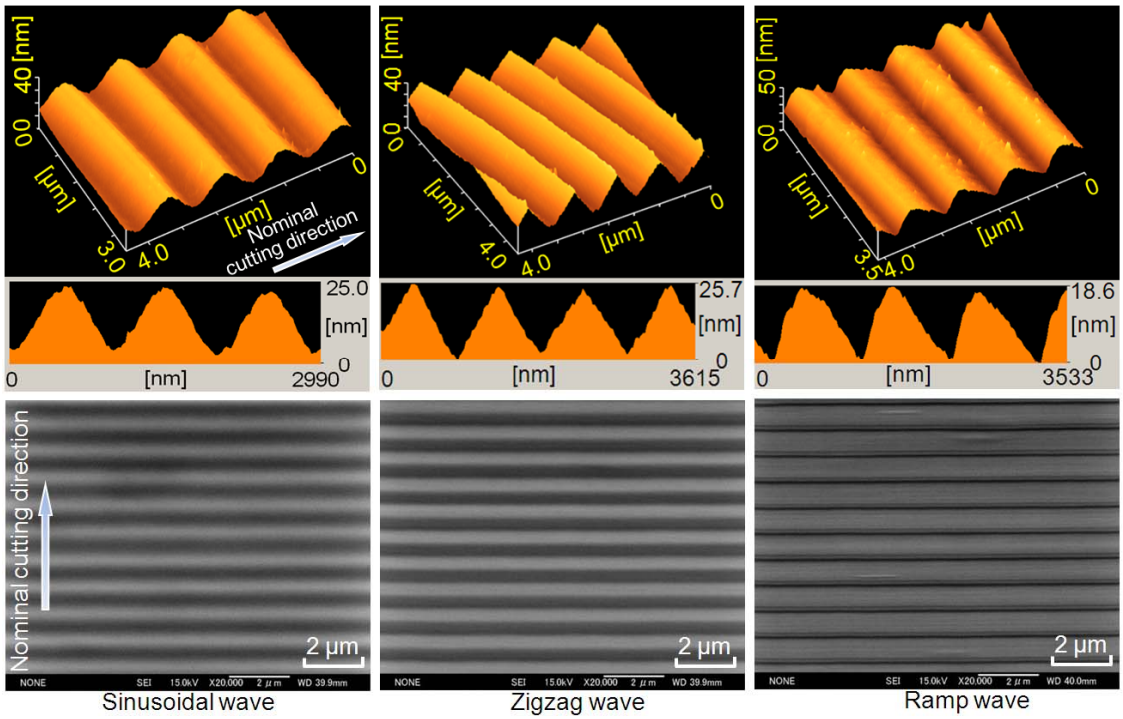

Fig. 5.15 Nano structures with structural height of 20 nm and wave length of 1 μm

Table 5.2: Experiment conditions for nano textured grooves machining

Cutting conditions	Nominal cutting speed [mm/min] Maximum depth of cut [μm] Cutting fluid	6 3 Oil mist (PS-FM-A)
Vibration conditions	Frequency [kHz] Phase shift [deg] Amplitude in depth of cut direction [$\mu m_{0\text{-}p}$] Amplitude in nominal cutting direction [$\mu m_{0\text{-}p}$]	36.2 -90 0.48-0.5 0.5
Tool	Material Nose radius [mm] Rake angle [deg] Clearance angle [deg]	Single crystal diamond 1 0 10
Workpiece	Hardened steel	SUS420J2 (HRC53)

The slope angles of the target profiles are less than 3.6 deg, which is smaller than the clearance angle of 10 deg. Hence, the slopes of the structures are theoretically machinable. However, note that the amplitude command is not compensated here since the ratio of the structure height to the wave length is significantly small. The measured sectional profiles along the nominal cutting direction verify surprising machining accuracy, where nano patterns with about a 20 nm structure height are machined accurately. Surprisingly, this structure height is generally in the same order of the surface roughness or less than that achieved by conventional ultra-precision cutting. Hence, this fact indicates that nano-structure can be machinable by applying the proposed sculpturing method.

5.6.2 Feasibility of three-dimensional structure machining

In the previous research, some micro/nano structures have been successfully fabricated on hardened steel by applying the proposed amplitude control sculpturing method [62]. For example, sinusoidal commands to control the vibration amplitude were input to the elliptical vibration control system during machining and the phase of the sinusoidal commands was changed by 180 degrees in every cutting feed, so that hexagonal dimple patterns can be sculptured based on vibration conditions, cutting conditions and tool geometries. Table 5.3 summarizes the experimental conditions.

Table 5.3: Experiment conditions for hexagonal dimple pattern fabrication

Cutting conditions	Nominal cutting speed [mm/min]	650
	Maximum depth of cut [μm]	5
	Pick feed [μm]	31
Vibration conditions	Frequency of elliptical vibration [kHz]	36.2
	Frequency of amplitude oscillation [Hz]	100
	Phase shift [deg]	90
	Amplitude in depth of cut direction [$\mu m_{0\text{-}p}$]	0.88-1.64
	Amplitude in nominal cutting direction [$\mu m_{0\text{-}p}$]	2
Tool	Material	Single crystal diamond
	Nose radius [mm]	1
	Rake angle [deg]	0
	Clearance angle [deg]	10
Workpiece	Hardened steel	SUS420J2 (HRC53)

Fig. 5.16 shows the optical microphotographs and a cross section profile of the fabricated hexagonal dimple patterns. The hexagonal dimple patterns with a measured dimple depth of 0.65 μm and a side length of 36.14 μm.

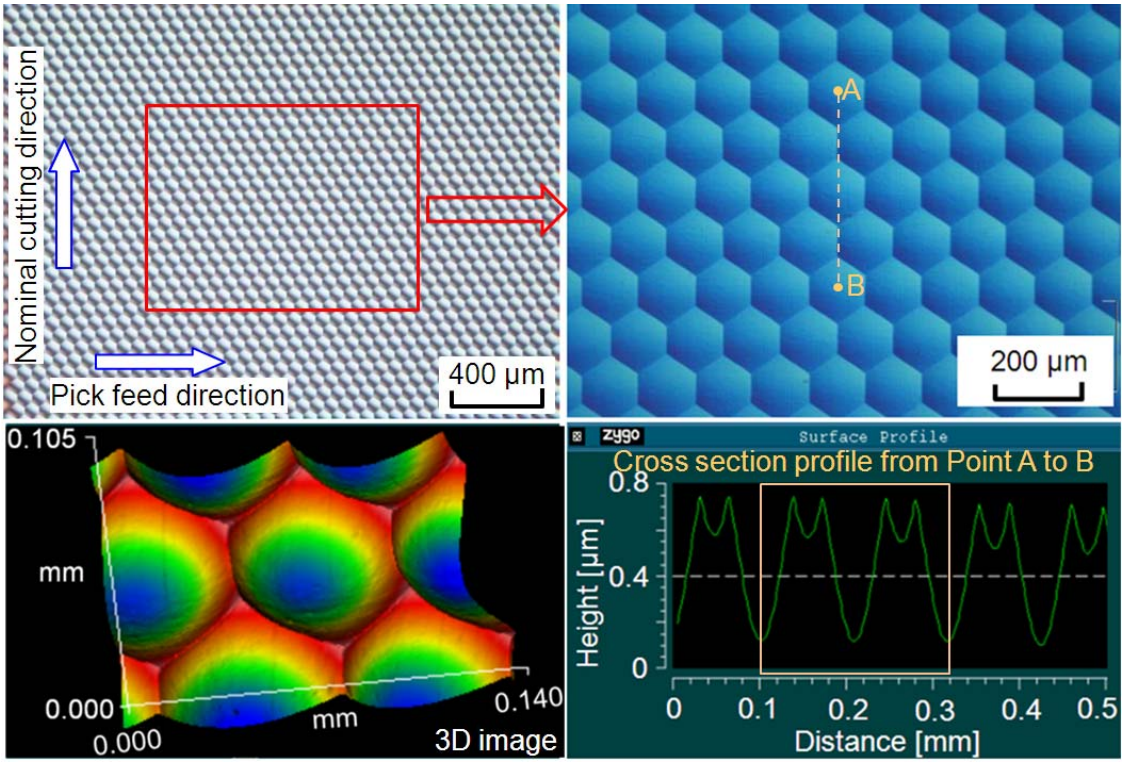

Fig. 5.16 Microphotographs of sculptured hexagonal dimples

In order to investigate the feasibility of practical application, the proposed machining method was applied to a sophisticated three-dimensional micro/nano structure sculpturing. Figure 5.17 shows the target machining geometry, i.e., an angle grid surface.

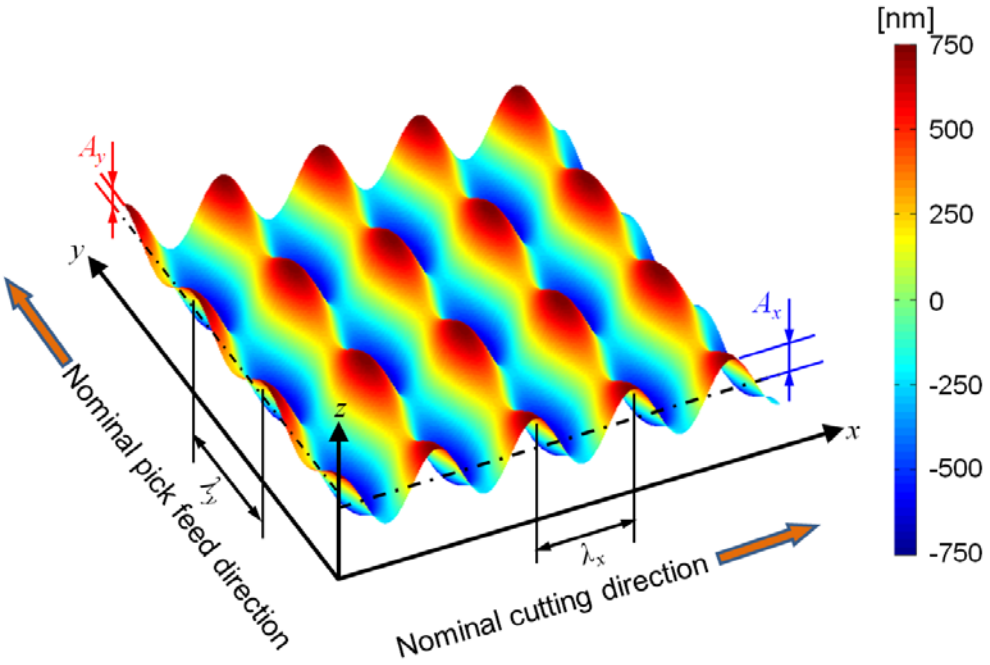

Fig. 5.17 Schematic of the angle grid surface

The height of the arbitrary position on the angle grid surface can be given by Eq. (5-1), which is presented by Gao et al. [114]:

$$z=A_x\sin(2\pi x/\lambda_x)+A_y\sin(2\pi y/\lambda_y), \quad (5\text{-}1)$$

where A_x and A_y are amplitudes of the sine functions in the x direction and the y direction, respectively. λ_x and λ_y are the corresponding wave lengths. By applying the proposed amplitude control sculpturing method, several grid surfaces with different geometry parameters are introduced.

Considering the restrictions of the tool radius in machinable part geometry, see Fig. 4.7 in Chapter 4, sculpturing of an angle grid structure approaching the limitation of machinable part geometry is challenged. A SCD tool with a nose radius of 1 mm, a rake angle of 0 deg and a clearance angle of 10 deg, was used. When the target amplitude is set to be A_x=A_y=0.5 μm, the wave length was set to be λ_x=λ_x=150 μm from the restrictions of tool nose radius in the nominal pick feed direction. The sinusoidal structure is machined by the amplitude control sculpturing method with a sinusoidal amplitude command at 100 Hz in the nominal cutting direction. The nominal cutting speed is set to be 900 mm/min. As the ratio of the structure height to the wave length is

much small, the amplitude command is not compensated here. On the other hand, the height position along the nominal pick feed direction was controlled by utilizing positioning of the ultra-precision machine tool. A pick feed is set to be 3 μm. Fig. 5.18 shows a microphotograph and a profile of the machined angle grid surface measured by optical microscopes (Nikon MM-40 and ZYGO NewView6200). It was confirmed that the periodic micro/nano structure with smooth surface is obtained on the hardened steel workpiece.

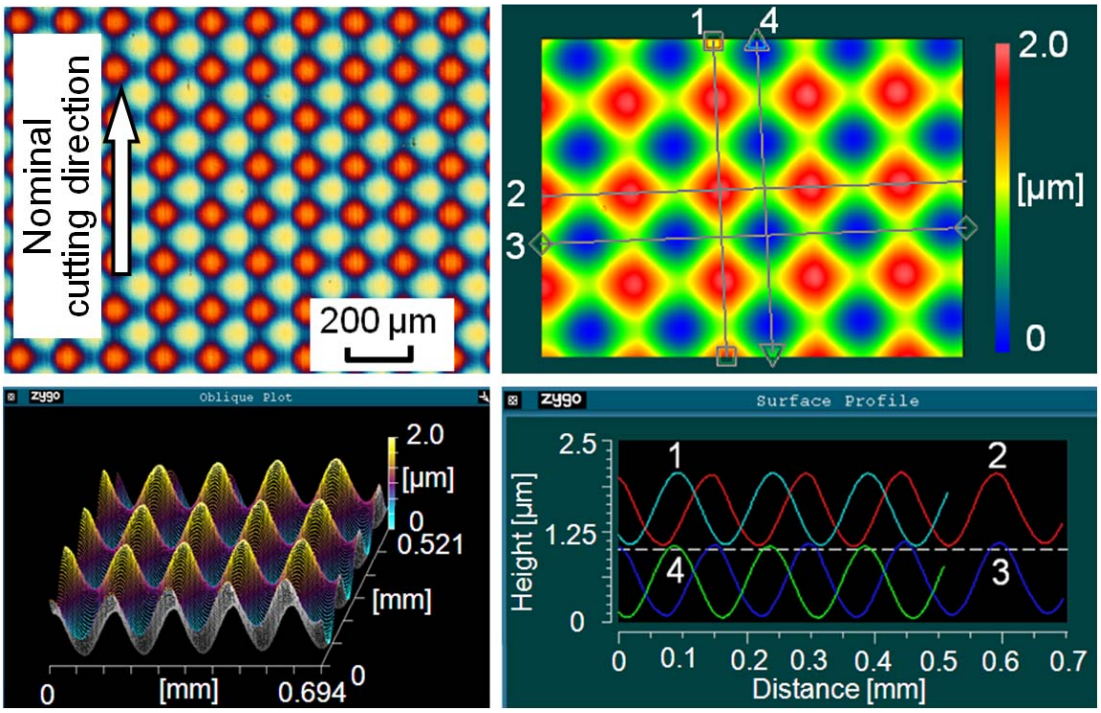

Fig. 5.18 Machined angle grid surface with the structure height of 1 μm and the wave length of 150 μm

Figure 5.19 shows a comparison of the simulated and the experimental results. It was confirmed that machined height and the wave length along the nominal cutting direction and nominal pick feed direction correspond accurately to the theoretical values.

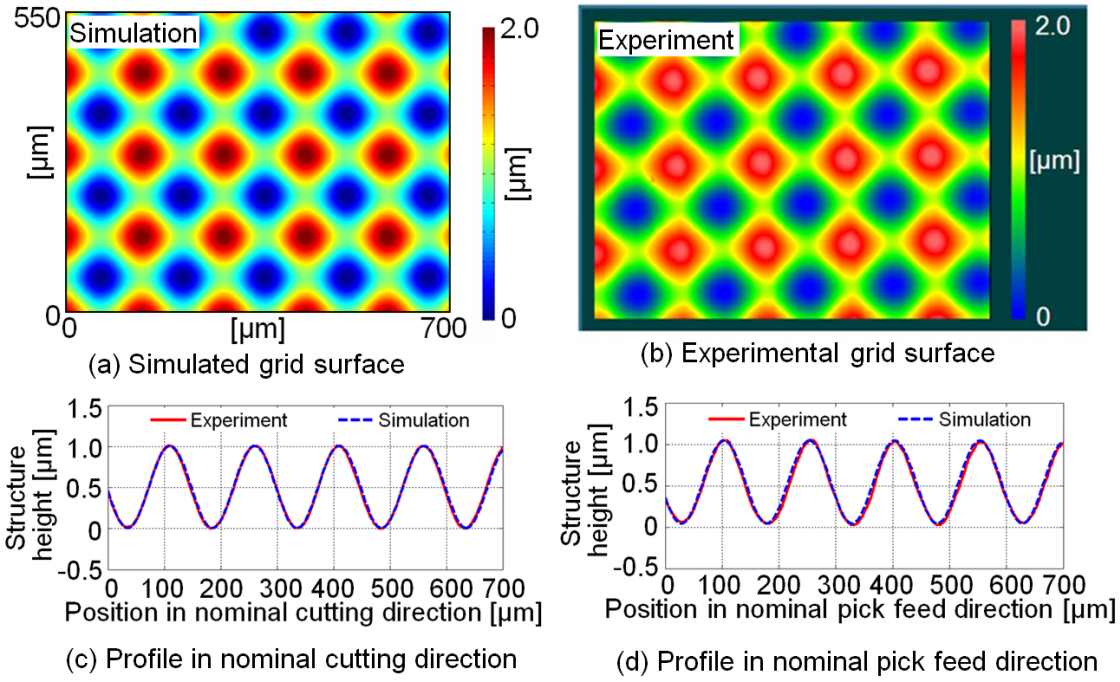

(a) Simulated grid surface

(b) Experimental grid surface

(c) Profile in nominal cutting direction

(d) Profile in nominal pick feed direction

Figure 5.19 Comparison of simulation and experimental result

Furthermore, considering the restrictions of the vibration conditions and the tool radius in machinable part geometry see Fig. 4.4 and Fig. 4.7 in Chapter 4, sculpturing of an angle grid structure approaching the limitation of machinable part geometry is also challenged. The structure height and wave length are 1 µm and 10 µm in the nominal cutting direction, while they are set to 0.5 µm and 15 µm in the nominal pick feed direction, respectively. The proposed command compensation method is utilized here. A SCD tool with a nominal nose radius of 10 µm, a rake angle of 0 deg and a clearance angle of 20 deg, was used. The sinusoidal structure is machined with an amplitude command at 100 Hz in the cutting direction. The cutting speed is set to be 60 mm/min, and then the maximum absolute value of the critical entrance angle is 17.96 deg, which is smaller than the clearance angle of cutting tool. Moreover, the height position along the nominal pick feed direction was also controlled by amplitude control command synchronously. The ultra-precision machine tool generates just a simple planing motion with the pick feed of 1.25 µm. The mean-to-peak vibration amplitude is fixed to 2 $\mu m_{0\text{-}p}$ in the nominal cutting direction, while varied within 0.5 to 2 $\mu m_{0\text{-}p}$ in the depth of cut direction.

Figure 5.20 (a) shows the machining results without command compensation. The atomic force microscope was used for the measurement of machined surface profiles. Due to the overcut error, the target shape is deteriorated into a serrated shape in the nominal cutting direction. On the other hand, Fig. 5.20 (b) shows the target structure machined by the proposed command compensation method. The machining accuracy in the nominal cutting direction is improved obviously.

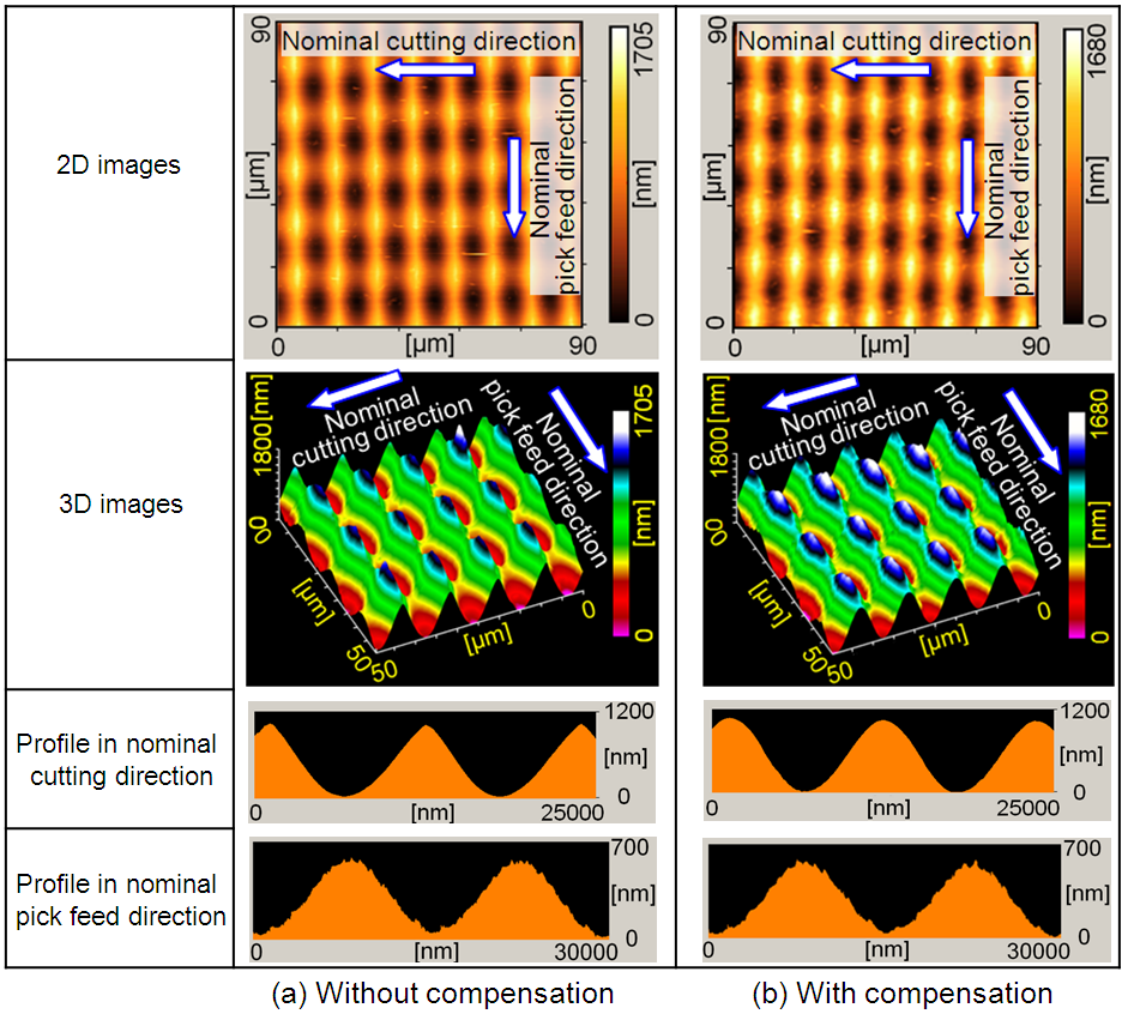

Fig. 5.20 Angle grid structure machining (a) without / (b) with command compensation in nominal cutting direction

Figure 5.21 (a) shows the profile and error components without the command compensation in the nominal cutting direction. There is a maximum machining error of

114.1 nm_{p-v} between the target profile and the measured profile. As a comparison, Figure 5.21 (b) shows the measured results with command compensation. The maximum machining error is decreased significantly to 22.6 nm_{p-v}.

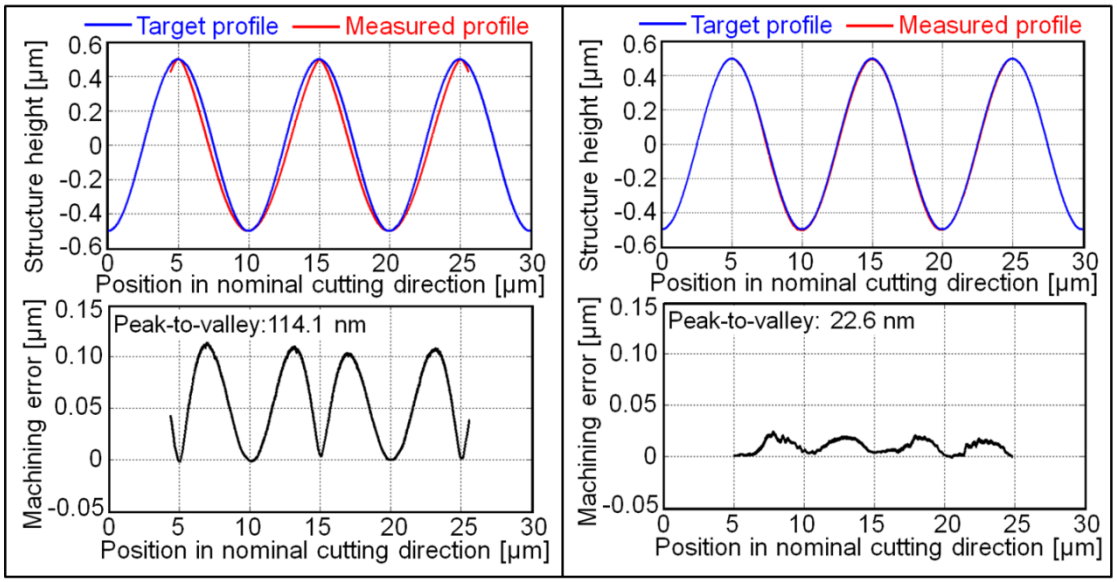

(a) Without compensation (b) With compensation

Fig. 5.21 Profile of machined structure and measured machining error in nominal cutting direction (a) without / (b) with command compensation

The machining accuracy in the nominal pick feed direction is also discussed. The influence of the cutting tool profile error on the machining accuracy along the nominal pick feed direction is not negligible in general. When the cutting edge profile is not exactly circular, machining with an assumption of the circular tool profile causes machining profile error. This problem is deeply associated with the ultra-precision manufacturing technology of SCD tools. Nowadays, SCD tools can be fabricated with accurate cutting edge profiles, whose profile error is, for instance, less than 50 nm [115]. With these tools, the machining profile error along the nominal pick feed direction can be decreased into around several tens of nanometers or less. If there is an error between the assumed and actual radius values, more error in the machining profile may be generated. In addition, when chipping or local shape deterioration generates on the cutting edge, the deteriorated profile of the cutting edge may be copied on the

workpiece surface, where a small scratch line may appear along the nominal cutting direction. This type of profile error causes surface roughness deteriorations.

Figure 5.22 shows the measured profile and the estimated machining profile in the nominal pick feed direction assuming a nose radius of 10 μm. The nose radius is small in the machining experiment, thus the feed marks are clearly observed in both profiles. Considering only the nose radius and the pick feed, theoretical roughness is calculated as about 20 nm. On the other hand, a larger feed mark can be observed in the measured profile, which may be due to the cutting edge profile error. Comparing the machining profile with the target profile, machining error along the pick feed direction is calculated. Figure 5.23 shows the error component of the machined profile along the nominal pick feed direction. The total machining error is about 88 $nm_{p\text{-}v}$. Local profile deviation by the spikes is considered to be due to the aforementioned feed marks. Through the experimental verifications, feasibility of accurate three-dimensional structure machining in nano scale is confirmed by applying the proposed amplitude control sculpturing method with command compensation.

This grid surface of 6 mm (nominal cutting direction) x 0.3 mm (nominal pick feed direction) was machined at about 40 min. As the machining area is small, total machining time might seem to be long. However, the machining pattern is significantly dense, and thus machining efficiency of the proposed machining method is considered not to be low. This machining performance is compared with those of other possible machining methods. The same micro structure can be fabricated on the steel materials by combining the elliptical vibration cutting technology and other ultra-precision positioning mechanisms. In case of utilizing just the positioning function of the ultra-precision machine tool [116], an extremely longer machining time is required due to extremely low dynamic response of the position control. Meanwhile, similar performance may be attained by utilizing fast tool servo (FTS) technology. It is, however, considered to be not advantageous to combine the elliptical vibration tool with the conventional FTS, because both devices already have a function of changing the depth of cut quickly [62]. In addition, in order to attain accurate machining, depth of cut control command needs to be compensated and the restriction in machinable part geometry

needs to be considered in the same way as proposed in Chapter 4.

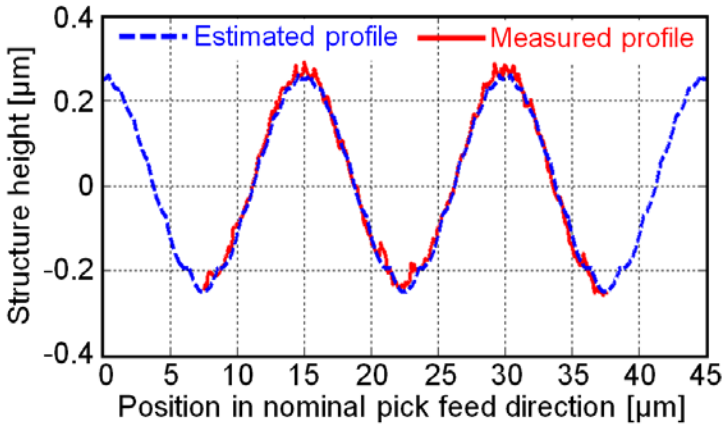

Fig. 5.22 Comparison of measured and estimated profiles in nominal pick feed direction

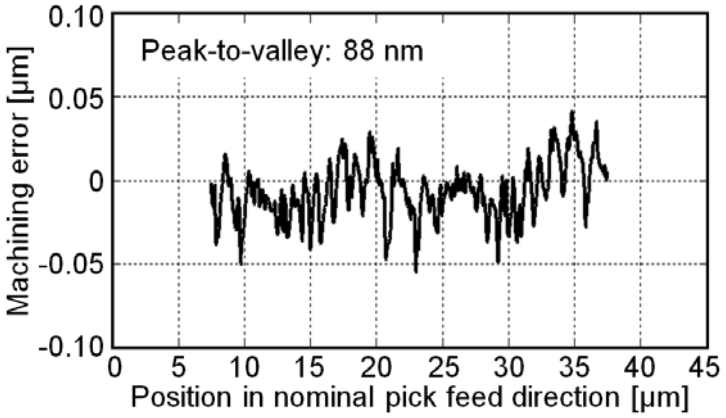

Fig. 5.23 Measured machining error in nominal pick feed direction

5.7 Summary

This chapter clarifies the feasibility of the highly-accurate micro/nano structure fabrication by applying the proposed amplitude control sculpturing method combining with the proposed command compensation method. Firstly, the machining accuracy of the proposed amplitude control sculpturing method was experimentally investigated. It is confirmed that nano structures can be machined with surprisingly high accuracy of about ±1 nm in the depth of cut direction. Then the proposed command compensation method was experimentally verified for decreasing the machining error efficiently. The target sine sweep structure introduced in Chapter 4 was fabricated. Without the

command compensation, the overcut causes serious machining accuracy deterioration and a maximum machining error of 242.5 nm_{p-v} was generated. On the other hand, it was confirmed that the proposed command compensation method improves the machining accuracy significantly and the machining error is decreased from 242.5 nm_{p-v} to 22.4 nm_{p-v}. Moreover, machining accuracy deterioration due to flank face contact with target shape is verified by the theoretical analyses and the experimental investigations. Following that, the proposed sculpturing method is applied to the fabrication of nano-textured structures. Nano patterns with about 20 nm structure height and 1 μm wave length can be machined accurately by applying the proposed sculpturing method. Finally, based on the clarified restrictions in machinable part geometry, feasibility of three-dimensional micro/nano structure machining on hardened steel workpiece is explored experimentally, and machining accuracy in nano scale is evaluated.

Chapter 6

Conclusions

Structured surfaces with sophisticated micro/nano structures can provide advanced and useful functions for various industrial applications. For mass production of these functional devices, hardened steel and tungsten carbide are heavily demanded in molding industry. However, conventional diamond cutting is not applicable to steel materials and tungsten carbide machining due to extreme tool wear and brittle fracture generations in the workpiece. To overcome this problem, elliptical vibration cutting technology (EVC) has been invented and applied to these difficult-to-cut materials machining successfully. Furthermore, utilizing the specific cutting process of EVC, a unique micro/nano sculpturing method for difficult-to-cut materials has been proposed. Based on these former studies, I challenged to develop further advanced machining technology for structured surface fabrication on steel and tungsten carbide.

This thesis mainly consists of two research topics. The first one is studied by grooving and planing investigations with the aim of achieving ductile machining of tungsten carbide and extending tool life by applying EVC technology. The second one is studied by theoretical formulations and experimental investigations in order to clarify the restrictions in machinable part geometry and improve the machining accuracy by applying the proposed amplitude control sculpturing method in EVC. The main contributions and findings are summarized as follows:

In Chapter 1, the background, motivation and objectives of this research were described.

Chapter 2 mainly clarified a criterion to indicate how to obtain ductile machining of tungsten carbide by applying EVC. The mechanism of ductile machining of tungsten carbide by applying EVC was clarified firstly. In the EVC process, the tool cuts the surface that is finished in the previous vibration cycle. Thus, the actual uncut chip, i.e., instantaneous uncut chip thickness, becomes extremely thin. Based on this process,

the actual cutting thickness becomes smaller than the critical value for ductile machining. In what follows, the influence of vibration and cutting conditions on the surface quality is investigated in an empirical manner. And then, the influence of material compositions on the machined surface quality is also investigated. An important criterion is clarified to indicate how to obtain ductile machining of tungsten carbide, i.e., grain size is equal to or less than 0.5 μm, binder material is helpful to suppress brittle crack propagation, and maximum instantaneous uncut chip thickness (MIUCT) is equal to or less than 4 nm. Based on these fundamental results, ultra-precision textured grooves and a dimple pattern are subsequently fabricated on tungsten carbide in ductile mode by applying the amplitude control sculpturing method in EVC.

Chapter 3 carries out the comprehensive study on tool life and surface integrity in elliptical vibration cutting of tungsten carbide for practical applications. It was clarified that finer grain size and presence of the binder material are advantageous to prevent fracture generation on the finished surface. However, these conditions are inversely disadvantageous to realize longer tool life. The tool wear progressed faster due to higher hardness and toughness of finer grain materials. The binder materials also accelerate the tool wear development due to their thermo-chemical affinity to diamond. Moreover, due to the specific cutting process with elliptical vibration, the tool damage progress has a strong relation with the cumulative cutting distance. Furthermore, the diamond tool with crystal orientation of R(110)F(100) is significantly advantageous to decrease the cutting force due to the reduction of flank wear. With increase of the nominal cutting distance to 19.04 m, the maximum roughness is still less than 100 nm Rz by using R(110)F(100). Based on the above-mentioned results, prediction models of the tool wear, cutting force, and surface roughness are developed. As a result, appropriate conditions can be selected to make a good balance in the surface quality and the tool life. Namely, mean-to-peak amplitudes A_c-A_d of 2-1 $\mu m_{0\text{-}p}$, a nominal cutting speed of 250 mm/min and a depth of cut less than 1.2 μm are approprite, which can satisfy not only ductile mode machining but also reasonable machining efficiency when machining the binderless tungsten carbide with the grain size of 0.3 μm.

Chapter 4 investigated the proposed amplitude control sculpturing method in detail.

According to the vibration conditions and the tool geometry, restrictions in machinable part geometry are clarified and formulated by considering the kinematic model of EVC. For concave structure machining, the curvature radius of the vibration locus needs to be smaller than or equal to that of the target profile at the tangential position on the target shape. The clearance angle of cutting tool also should be larger than the critical entrance angle in the EVC process, while avoidance of the rake face contact to the target structure is important especially in uphill machining. Furthermore, the tool radius restricts the sharpness of a concave part geometry in the nominal pick feed direction. The curvature radius of the concave part geometry always needs to be larger than the tool radius. Moreover, due to the existence of a finite amplitude in the nominal cutting direction, the proposed amplitude control machining method imposes a machining error between the amplitude command and the envelope of the tool trajectory especially at portions with steep slopes and sharp corners. In order to cancel out this machining error, the amplitude command in the depth of cut direction is compensated. In the proposed compensation method, the vibration locus is controlled to be tangential to the target profile in each vibration cycle. A verifying target profile of the sine sweep structure was assumed, where the structure height is 1 μm and the wave length is decreased from 31.62 μm to 6.75 μm. Without the command compensation, the maximum machining error increases up to 0.235 μm in the simulation process. As a comparison, the envelope of the tool trajectory is accurately identical with the ideal target profile by applying the proposed command compensation method. The machining error is decreased into 0 μm in the simulation process.

Chapter 5 clarifies the highly-accurate micro/nano structure fabrication by experimental investigations. It is confirmed that nano structures can be fabricated with a machining accuracy of about ±1 nm in the depth of cut direction. Then, the target sine sweep structure introduced in Chapter 4 was machined in the experimental verification. Without the command compensation, the overcut caused serious machining accuracy deterioration, where a maximum machining error of 242.5 $nm_{p\text{-}v}$ was generated. On the other hand, it was confirmed that the proposed command compensation method improves the machining accuracy significantly and the maximum machining error was

decreased from 242.5 nm_{p-v} to 22.4 nm_{p-v}. Furthermore, the restriction of tool geometry, especially the clearance angle, on the machinable part geometry is also evaluated by comparing the theoretical analyses and the experimental results. The contact between the tool flank face and the target shape resulted in significant deterioration of the machining accuracy, where a maximum machining error of about 378.2 nm_{p-v} was generated in the machining of the target sine sweep structure introduced in Chapter 4. In what follows, accurate nano sculpturing with a structure height of 20 nm and wave length of 1 μm was attained by applying the amplitude control commands with sinusoidal, zigzag, and ramp waves. Finally, a sophisticated 3D micro/nano structure, i.e., a sinusoidal grid surface, was subsequently carried out on a hardened steel workpiece. Without the command compensation, there is a maximum machining error of 114.1 nm_{p-v} between the target profile and the measured profile in the depth of cut direction. Meanwhile, the maximum machining error is decreased significantly to 22.6 nm_{p-v} with the command compensation. The experimental results verified the feasibility of efficient and accurate micro/nano machining by the proposed sculpturing method with the proposed command compensation.

Based on these researches in the thesis, the appropriate conditions for ductile mode machining, tool life and machining performances can be estimated for the machining of tungsten carbide by applying EVC technology in advance. Moreover, considering the amplitude control sculpturing method in EVC, we can determine the machinable part geometry and guarantee the machining accuracy in advance. Hence, this study is significantly advantageous to promote the industrial application of EVC technology, which can achieve micro/nano-scale structures fabrication on difficult-to-cut materials efficiently, which is impossible for other cutting technologies.

References

[1] C.J. Evans, J.B. Bryan. "Structured", "Textured" or "Engineered" surfaces. CIRP Annals - Manufacturing Technology, 48(2): 541-556 (1999).

[2] http://news.xinhuanet.com/foto/2013-06/18/c_124873123_6.htm. (In Chinese)

[3] L. Li, A.Y. Yi. Design and fabrication of a freeform microlens array for a compact large-field-of-view compound-eye camera. Applied Optics, 51(2): 1843-1852 (2012).

[4] R. Reichle, C. Pruss, C. Gessenhardt, C. Schulz, W. Osten. Diffractive/refractive (hybrid) UV-imaging system for minimally invasive metrology: design, performance, and application experiments. Applied Optics, 51(12): 1982-1996 (2012).

[5] H.P. D.Shieh, Y.P. Huang, K.W. Chien. Micro-optics Components for liquid crystal displays applications. The 24th International Display Research Conference, Korea, 56-58 (2004).

[6] L. Sun, S. Jin, S. Cen. Free-form microlens for illumination applications. Applied Optics, 48(29): 5520-5527 (2009).

[7] W.T. Xie, Y.J. Dai, R.Z. Wang, K. Sumathy. Concentrated solar energy applications using Fresnel lenses: A review. Renewable and Sustainable Energy Reviews,15(6): 2588-2606 (2011).

[8] H. Suzuki, M. Okada, Y. Yamagata, S. Morita, T. Higuchi. Precision grinding of structured ceramic molds by diamond wheel trued with alloy metal. Annals of the CIRP, 61(1): 283-286 (2012).

[9] P.R. Lewis, C.W. McCutchen. Experimental evidence for weeping lubrication in mammalian joints. Nature, 184: 1285 (1959).

[10] H. Miyoshi, T. Adachi, J. Ju, S.M. Lee, D.J. Cho, J.S. Ko, G. Uchida, Y. Yamagata. Characteristics of motility-based filtering of adherent cells on microgrooved surfaces. Biomaterials, 33: 395-401 (2012)

[11] S. Henry, D.V. McAllister, M.G. Allen, M.R. Prausnitz. Microfabricated micro-needles: a novel approach to transdermal drug delivery. Journal of Pharmaceutical Sciences, 87(10): 922-925 (1998).

[12] http://www.rolith.com/applications/self-cleaning

[13] M. Callies, Y. Chen, F. Marty, A. Pepin, D. Quere. Microfabricated textured surfaces for super-hydrophobicity investigations. Microelectronics Engineering, 78-79: 100-105 (2005).

[14] J. Bico, C. Marzolin, D. Quéré. Pearl drops. Europhysics Letters, 47: 220-226 (1999).

[15] R.M. Wu, H.F. Li, Z.R. Zheng, X. Liu. Freeform lens arrays for off-axis illumination in an optical lithography system. Applied Optics, 50: 725-732 (2011).

[16] W. Gao, S. Dejima, S. Kiyono. A Dual-Mode Surface Encoder for Position Measurement. Sensors and Actuators A, 117(1): 95-102 (2005).

[17] W. Gao, A. Kimura. A three-axis displacement sensor with nanometric resolution. CIRP Annals-Manufacturing Technology, 56: 529-532 (2007).

[18] H.L. Costa, I.M. Hutchings. Hydrodynamic lubrication of textured steel surfaces under reciprocating sliding conditions. Tribology International, 40: 1227-1238 (2007).

[19] A.A.G. Bruzzone, H.L. Coata, P.M. Lonardo. Advances in engineered surfaces for functional performance. CIRP Annals-Manufacturing Technology, 57(2): 750-769 (2008)

[20] N. Kawasegi, H. Sugimori, H. Morimoto, N. Morita, I. Hori. Development of cutting tools with microscale and nanoscale textures to improve frictional behavior. Precision Engineering, 33: 248-254 (2009).

[21] T. Obikawa, A. Kamio, H. Takaoka, A. Osada. Micro-texture at the coated tool face for high performance cutting. International Journal of Machine Tools and Manufacture, 51(12): 966-972 (2011).

[22] C. Sodtke, P. Stephan. Spray cooling on micro structured surfaces. International Journal of Heat and Mass Transfer, 50(19-20): 4089-4097 (2007).

[23] A.P. Pop, P. Ungur, G. Bejinaru Mihoc. Applications of microlens arrays. Fascicle of Management and Technological Engineering, VI(XVI): 675-680 (2007).

[24] N. Li, A. Tourovskaia, A. Folch. Biology on a chip: microfabrication for studying the behavior of cultured cells. Journal of Critical Reviews in Biomedical Engineering. 31: 423-488 (2003).

[25] S. Setzu, P. Ferrand, G. L, R. Romestain. Photo-lithography for 2D optical microstructures in porous silicon: application to nucleation of macropores. Applied Surface Science, 186(1-4): 588-593 (2002).

[26] N.H. Rizvi, D.K. Milne, P.T. Rumsby, M.C. Gower. Laser micromachining: new developments and applications. SPIE Proceedings, 3933 (2000).

[27] Laser Laboratorium Göttingen e.V.. Annual Report 2011: 39-41

[28] K.H. Choi, J. Meijer, T. Masuzawa, D.H. Kim. Excimer laser micromachining for 3D microstructure. Journal of Materials Processing Technology, 149(1-3): 561-566 (2004).

[29] M.J. Vasile, R. Nassar, J. Xie, H. Guo. Microfabrication techniques using focused ion beams and emergent applications. Micron, 30(3): 235-244 (1999).

[30] P. Olivero, S. Rubanov, P. Reichart, B.C. Gibson, S.T. Huntington, J.R. Rabeau, A.D. Greentree, J. Salzman, D. Moore, D.N. Jamieson, S. Prawer. Characterization of three-dimensional microstructures in single-crystal diamond. Diamond and Related Materials, 15(10): 1614-1621 (2006).

[31] P. Savander. Microlens arrays etched into glass and silicon. Optics and Lasers in Engineering, 20(2): 97-107 (1994).

[32] J. Ramiro, S. Merino, S. Azcárate. EUMINAfab: Micro and nano fabrication technologies for optical and sensor applications. http://science24.com/paper/23296

[33] A.A. Tseng. Recent developments in micromilling using focused ion beam technology. Journal of Micromechanics and Microengineering, 14: R15-R34 (2004).

[34] B. Kress, D. Zaleta, W. Daschner, K. Urquhart, R. Stein, S.H. Lee. Diffractive optics fabricated by electron-beam direct writing methods, Binary Optics: An Opportunity for Technical Exchange, NASA, Marshall Space Flight Center, Conference on Binary Optics: An Opportunity for Technical Exchange, 195-205 (1993).

[35] V.R. Manfrinato, L.H. Zhang, D. Su, H.G. Duan, R.G. Hobbs, E.A. Stach, K.K. Berggren. Resolution limits of electron-beam lithography toward the atomic scale. Nano Letters, 13(4): 1555-1558 (2013).

[36] F.Z. Fang, X.D. Zhang, X.T. Hu. Cylindrical coordinate machining of optical freeform surfaces. Optics Express, 16(10): 7323-7329 (2008).

[37] C.C. Chen, C.M. Chen, J.R. Chen. Tool path generation for diamond shaping of aspheric lens array. Journal of Materials Processing Technology, 192-193:194-199 (2007).

[38] M.H. Miller, K.P. Garrard, T.A. Dow, L.W. Taylor. A controller architecture for integrating a fast tool servo into a diamond turning machine. Precision Engineering, 16(1): 42-48 (1994).

[39] F.Z. Fang, X.D. Zhang, A. Weckenmann, G.X. Zhang, C. Evans. Manufacturing and measurement of freeform optics. CIRP Annals-Manufacturing Technology, 62(2): 823-846 (2013).

[40] E. Brinksmeier, O. Riemer, R. Gläbe, B. Lünemann, C.v. Kopylow, C. Dankwart, A. Meier. Submicron functional surfaces generated by diamond machining. CIRP Annals-Manufacturing Technology, 59: 535-538 (2010).

[41] E. Brinksmeier, R. Glabe, L. Schonemann. Review on diamond-machining processes for the generation of functional surface structures. CIRP Journal of Manufacturing Science and Technology, 5: 1-7 (2012).

[42] J.B. Zhou, L. Li, N. Naples, T. Sun, A.Y. Yi. Fabrication of continuous diffractive optical elements using a fast tool servo diamond turning process. Journal of Micromechanics and Microengineering, 23: 075010 (2013).

[43] K. Sawada, T. Kawai, Y. Takeuchi, T. Sata. Development of ultraprecision micro grooving (manufacture of V-shaped groove). JSME International Journal. Series C: Mechanical Systems, Machine Elements and Manufacturing, 43(1): 170-176 (2000).

[44] D. Dornfeld, S. Min, Y. Takeuchi. Recent advances in mechanical micromachining. CIRP Annals-Manufacturing Technology, 55(2): 745-768 (2006).

[45] K. Sawada, T. Kawai, Y. Takeuchi. High aspect ratio micro structuring by means of mechanical machining. Conference of The Japan Society of Mechanical Engineers, 2: 103-104 (2000).

[46] H. Suzuki, T. Moriwaki, Y. Yamamoto, Y. Goto. Precision cutting of aspherical ceramic molds with micro PCD milling tool. CIRP Annals-Manufacturing Technology, 56(1): 131-134 (2007)

[47] Y. Yamamoto, H. Suzuki, T. Onishi, T. Okino, T. Moriwaki, K. Fuji, Y. Goto, T. Ono. A

study on ultra precision cutting of micro aspherical molds of tungsten carbide with PCD milling tools. Conference of The Japan Society of Mechanical Engineers, 6: 179-180 (2006) (In Japanese).

[48] E. Brinksmeier, Y. Mutlugünes, F. Klocke, J.C. Aurich, P. Shore, H. Ohmori. Ultra-precision grinding. CIRP Annals-Manufacturing Technology, 59(2): 652-671 (2010).

[49] H.W. Hoffmeister, R. Wittmer. Grinding hard and brittle materials with CVD-diamond microgrinding wheels. Proceedings of the 24th Annual Meeting of the ASPE, Monterey, USA (2009).

[50] H. Suzuki, T. Higuchi, M. Nishioka, T. Kitajima, A. Yui, S. Okuyama, H. Shibutani, O. Horiuchi. Precision grinding of micro Fresnel shape and precision glass molding of micro Fresnel lens. Proceedings of the 16th Annual Meeting of the ASPE, Crystal City, USA, 25: 437-440 (2001).

[51] Y. Yamamoto, H. Suzuki, T. Onishi, T. Okino, T. Moriwaki. Precision grinding of micro array lens molding die with 4-axes controlled micro wheel. International Conference on Leading Edge Manufacturing in 21st Century, 1029-1034 (2005).

[52] S. Yin, H. Ohmori, Y. Uehara, T. Shimizu, W. Lin. Micro V-grooves grinding technique of large germanium immersion grating element for mid-infrared spectograph. International Conference on Leading Edge Manufacturing in 21st Century, 223-228 (2003).

[53] J.W. Yan, T. Oowada, T.F. Zhou, T. Kuriyagawa. Precision machining of microstructures on electroless-plated NiP surface for molding glass components. Journal of Materials Processing Technology, 209: 4802-4808 (2009).

[54] E. Paul, C.J. Evans, A. Mangamelli, M.L. McGlauflin, R.S. Polvani. Chemical aspects of tool wear in single point diamond turning. Precision Engineering, 18(1): 4-19 (1996).

[55] J.M. Casstevens. Diamond turning of steel in carbon saturated atmospheres. Precision Engineering, 5: 9-15 (1983).

[56] C. Evans. Cryogenic diamond turning of stainless steel. CIRP Annals-Manufacturing Technology, 40(1): 571-575 (1991).

[57] E. Brinksmeier, R. Gläbe, J. Osmer. Ultra-precision diamond cutting of steel molds. CIRP Annals-Manufacturing Technology, 55(1): 551-554 (2006).

[58] Y. Song, K. Nezu, C. Park, T. Moriwaki. Tool wear control in single-crystal diamond cutting of steel by using the ultra-intermittent cutting method. International Journal of Machine Tools and Manufacture, 49: 339-343 (2009).

[59] B. Bulla, F. Klocke, O. Dambon. Analysis on ductile mode processing of binderless, nano crystalline tungsten carbide through ultra precision diamond turning. Journal of Materials Processing Technology, 212: 1022-1029 (2012).

[60] D.E. Brehl, T.A. Dow. Review of vibration-assisted machining. Precision Engineering, 32 (3): 153-172 (2008).

[61] E. Shamoto, T. Moriwaki. Study on elliptical vibration cutting. CIRP Annals-Manufacturing Technology, 43 (1): 35-38 (1994).

[62] N. Suzuki, H. Yokoi, E. Shamoto. Micro/nano sculpturing of hardened steel by controlling vibration amplitude in elliptical vibration cutting. Precision Engineering, 35: 44-50 (2011).

[63] R.C. Skelton. Turning with an oscillating tool. International Journal of Machine Tool Design and Research, 8: 239-259 (1968).

[64] J. Kumabe, K. Fuchizawa, T. Soutome, Y. Nishimoto. Ultrasonic superposition vibration cutting of ceramics. Precision Engineering, 11(2): 71-77 (1989).

[65] V.I. Babitsky, A.V. Mitrofanov, V.V. Silberschmidt. Ultrasonically assisted turning of aviation materials: Simulations and experimental study. Ultrasonics, 42: 81-86 (2004).

[66] M. Zhou, X.J. Wang, B.K.A. Ngoi, J.G.K. Gan. Brittle-ductile transition in the diamond cutting of glasses with the aid of ultrasonic vibration. Journal of Materials Processing Technology, 121: 243-251 (2002).

[67] T. Moriwaki, E. Shamoto, K. Inoue. Ultraprecision ductile cutting of glass by applying ultrasonic vibration. CIRP Annals-Manufacturing Technology, 41: 141-144 (1992).

[68] T. Moriwaki, E. Shamoto. Ultraprecision diamond turning of stainless steel by applying ultrasonic vibration. CIRP Annals-Manufacturing Technology, 40: 559-562

(1991).

[69] K. Liu, X. P. Li, M. Rahman. Characteristics of ultrasonic vibration-assisted ductile mode cutting of tungsten carbide. International Journal of Advanced Manufacturing Technology, 35: 833-841 (2008).

[70] M. Zhou, Y.T. Eow, B.K. Ngoi, E.N. Lim. Vibration-assisted precision machining of steel with PCD tools. Materials and Manufacturing Processes, 18: 825-834 (2003).

[71] M. Zhou, B.K.A. Ngoi, M.N. Yusoff, X.J. Wang. Tool wear and surface finish in diamond cutting of optical glass. Journal of Materials Processing Technology, 174: 29-33 (2006).

[72] M. Xiao, S. Karube, T. Soutome, K. Sato. Analysis of chatter suppression in vibration cutting. International Journal of Machine Tools and Manufacture, 42: 1677-1685 (2002).

[73] E. Shamoto, Y. Morimoto, T. Moriwaki. Elliptical vibration cutting (2nd report, study on effects of vibration conditions). Journal of Japan Society for Precision Engineering, 65: 411-417 (1999). (In Japanese)

[74] E. Shamoto, N. Suzuki, R. Hino. Analysis of 3D elliptical vibration cutting with thin shear plane model. CIRP Annals-Manufacturing Technology, 57(1): 57-60 (2008).

[75] T. Moriwaki, E. Shamoto. Ultrasonic elliptical vibration cutting. CIRP Annals-Manufacturing Technology, 44(1): 31-34 (1995).

[76] E. Shamoto, N. Suzuki, Y. Naoi, T. Moriwaki. Development of ultrasonic elliptical vibration controller for elliptical vibration cutting. CIRP Annals-Manufacturing Technology, 51(1): 327-330 (2002).

[77] E. Shamoto, T. Moriwaki. Ultaprecision diamond cutting of hardened steel by applying elliptical vibration cutting. CIRP Annals-Manufacturing Technology, 48(1): 441-444 (1999).

[78] N. Suzuki, A. Nakamura, E. Shamoto, K. Harada, M. Matsuo, M. Osada. Ultraprecision micromachining of hardened steel by applying ultrasonic elliptical vibration cutting. Proceedings of International Symposium on Micromechatronics and Human Science, Nagoya, Japan, 221-226 (2003).

[79] E. Brinksmeier, R. Gläbe. Advances in precision machining of steel. CIRP

Annals-Manufacturing Technology, 50(1): 385-388 (2001).

[80] X.Q. Zhang, A.S. Kumar, M. Rahman, C. Nath, K. Liu. Experimental study on ultrasonic elliptical vibration cutting of hardened steel using PCD tools. Journal of Materials Processing Technology, 211: 1701-1709 (2011).

[81] N. Suzuki, M. Haritani, J. Yang, R. Hino, E. Shamoto. Elliptical vibration cutting of tungsten alloy molds for optical glass parts. CIRP Annals-Manufacturing Technology, 56(1): 127-130 (2007).

[82] N. Suzuki, R. Hino, S. Masuda, E. Shamoto. Ultraprecision cutting of sintered tungsten carbide by applying elliptical vibration cutting-Study on ductile cutting mechanics. Journal of Japan Society for Precision Engineering, 72(4): 539-545 (2006). (In Japanese)

[83] N. Suzuki, S. Masuda, E. Shamoto. Ultraprecision machining of sintered tungsten carbide by applying ultrasonic elliptical vibration cutting. Proceedings of 4th euspen International Conference, Glasgow, Scotland, 187-188 (2004).

[84] C. Nath, M. Rahman, K.S. Neo. A study on ultrasonic elliptical vibration cutting of tungsten carbide. Journal of Materials Processing Technology, 209: 4459-4464 (2009).

[85] C. Nath, M. Rahman, K.S. Neo. Machinability study of tungsten carbide using PCD tools under ultrasonic elliptical vibration cutting. International Journal of Machine Tools and Manufacture, 49: 1089-1095 (2009).

[86] C. Nath, M. Rahman, K.S. Neo. A study on the effect of tool nose radius in ultrasonic elliptical vibration cutting of tungsten carbide. Journal of Materials Processing Technology, 209: 5830-5836 (2009).

[87] G.D. Kim, B.G. Loh. Characteristics of chip formation in micro V-grooving using elliptical vibration cutting. Journal of micromechanics and microengineering, 17: 1458-1466 (2007).

[88] E. Shamoto, N. Suzuki, E. Tsuchiya, Y. Hori, H. Inagaki, K. Yoshino. Development of 3 DOF ultrasonic vibration tool for elliptical vibration cutting of sculptured surfaces. CIRP Annals-Manufacturing Technology, 54(1): 321-324 (2005).

[89] L. Yin, A.C. Spowage, K. Ramesh, H. Huang, J.P. Pickering, E.Y.J. Vancoille.

Influence of microstructure on ultraprecision grinding of cemented carbides. International Journal of Machine Tools and Manufacture, 44: 533-543 (2004).

[90] L. Yin, E.Y. Vancoille, K. Ramesh, H. Huang, J.P. Pickering, A.C. Spowage. Ultraprecision grinding of tungsten carbide for spherical mirrors. Proceedings of the Institution of Mechanical Engineers. Part B, Journal of engineering manufacture 218(4): 419-429 (2004).

[91] Y. Yamamoto, H. Suzuki, T. Moriwaki, T. Okino, Y. Hijikata, J. Roblee, T. Miyashita. Development of cross and parallel mode grinding machine for high na aspherical mold and die. Proceedings of the 21th Annual Meeting of the ASPE, Monterey, USA, 39: 499-502 (2006).

[92] H. Suzuki, T. Moriwaki, T. Okino, Y. Ando. Development of ultrasonic vibration assisted polishing machine for micro aspheric die and mold. CIRP Annals-Manufacturing Technology, 55(1): 385-388 (2006).

[93] H. Suzuki, S. Hamada, T. Okino, M. Kondo, Y. Yamagata, T. Higuchi. Ultraprecision finishing of micro-asphric surface by ultrasonic two-axis vibration assisted polishing. CIRP Annals-Manufacturing Technology, 59(1): 347-350 (2010).

[94] J.G. Zhang, N. Suzuki, Y.L. Wang, E. Shamoto. Fundamental investigation of ultra-precision ductile machining of tungsten carbide by applying elliptical vibration cutting with single crystal diamond. Journal of Materials Processing Technology, 214: 2644-2659 (2014).

[95] J.G. Zhang, N. Suzuki, T. Kato, R. Hino, E. Shamoto. Influence of material composition on ductile machining of tungsten carbide in elliptical vibration cutting. Key Engineering Materials, 523-524: 113-118 (2012).

[96] J.G. Zhang, N. Suzuki, E. Shamoto. Micro machining of binderless tungsten carbide by applying elliptical vibration cutting technology. Proceedings of The Japan Society for Abrasive Technology Conference (ABTEC), Kasugai, Japan, 109-114 (2011).

[97] M. Arif, M. Rahman, W.Y. San. Analytical model to determine the critical conditions for the modes of material removal in the milling process of brittle material. Journal of Materials Processing Technology, 212: 1925-1933 (2012).

[98] K. Jia, T.E. Fischer. Abrasion resistance of nanostructured and conventional cemented carbides. Wear, 200: 206-214 (1996).

[99] H. Saito, A. Iwabuchi, T. Shimizu. Effects of Co content and WC grain size on wear of WC cemented carbide. Wear, 261: 126-132 (2006).

[100] P.V. Krakhmalev, T. Adeva Rodil, J. Bergström. Influence of microstructure on the abrasive edge wear of WC-Co hard metals. Wear, 263: 240-245 (2007).

[101] Y.H. Ren, B. Zhang, Z.X. Zhou. Specific energy in grinding of tungsten carbides of various grain sizes. CIRP Annals - Manufacturing Technology, 58: 299-302 (2009).

[102] Z.G. Fang, J.W. Eason. Study of nanostructured WC-Co composites. International Journal of Refractory Metals and Hard Materials, 13: 297-303 (1995).

[103] J.W. Yan, Z.Y. Zhang, T. Kuriyagawa. Mechanism for material removal in diamond turning of reaction-bonded silicon carbide. International Journal of Machine Tools and Manufacture, 49: 366-374 (2009).

[104] Z.J. Yuan, J.C. He, Y.X. Yao. The optimum crystal plane of natural diamond tool for precision machining. CIRP Annals-Manufacturing Technology, 41(1): 605-608 (1992).

[105] M.S. Uddin, K.H.W. Seah, X.P. Li, M. Rahman, K. Liu. Effect of crystallographic orientation on wear of diamond tools for nano-scale ductile cutting of silicon. Wear, 257: 751-759 (2004).

[106] W.J. Zong, Z.Q. Li, T. Sun. The basic issues in design and fabrication of diamond-cutting tools for ultra-precision and nanometric machining. International Journal of Machine Tools and Manufacture, 50: 411-419 (2010).

[107] W.J. Zong, Z.Q. Li, T. Sun, D. Li, K. Cheng. Analysis for the wear resistance anisotropy of diamond cutting tools in theory and experiment. Journal of Materials Processing Technology, 210: 858-867 (2010).

[108] E. Brinksmeier, R. Gläbe, J. Osmer. Ultra-precision diamond cutting of steel molds. CIRP Annals-Manufacturing Technology, 53(1): 551-554 (2006).

[109] E. Brinksmeier, O. Riemer, A. Gessenharter, L. Autschbach. Polishing of structured molds. CIRP Annals-Manufacturing Technology, 53(1): 247-250 (2004).

[110] J.G. Zhang, N. Suzuki, Y.L. Wang, E. Shamoto. Ultra-Precision Nano-Structure

Fabrication by Amplitude Control Sculpturing Method in Elliptical Vibration Cutting. Precision Engineering (Accepted in 2014.07.11, in press).

[111] J.G. Zhang, N. Suzuki, E. Shamoto. Investigation on machining performance of amplitude control sculpturing method in elliptical vibration cutting. Procedia CIRP, 8: 328-333 (2013).

[112] P. Guo, K.F. Ehmann. Development of a tertiary motion generator for elliptical vibration texturing. Precision Engineering, 37: 364-371 (2013).

[113] P. Guo, K.F. Ehmann. An analysis of the surface generation mechanics of the elliptical vibration texturing process. International Journal of Machine Tools and Manufacture, 64: 85-95 (2013).

[114] W. Gao, T. Araki, S. Kiyono, Y. Okazaki, M. Yamanaka. Precision nano-fabrication and evaluation of a large area sinusoidal grid surface for a surface encoder. Precision Engineering, 27: 289-298 (2003).

[115] http://www.allied-material.co.jp/english/products/diamond/cutting/upc/

[116] D.E. Brehl, T.A. Dow. 3-D microstructure creation using elliptical vibration-assisted machining. Proceedings of the 22th Annual Meeting of the ASPE, Dallas Texas, USA, 21-26 (2007).

List of publications

Journal paper:

1-1 J. Zhang, N. Suzuki, Y. Wang, E. Shamoto. Fundamental investigation of ultra-precision ductile machining of tungsten carbide by applying elliptical vibration cutting with single crystal diamond. Journal of Materials Processing Technology, 124(11): 2644-2659 (2014).

1-2 J. Zhang, N. Suzuki, Y. Wang, E. Shamoto. Nano-Structure Fabrication by Ultra-Precision Amplitude Control Sculpturing Method in Elliptical Vibration Cutting. Precision Engineering (Accepted in 2014-07-11).

International conference paper:

2-1 J. Zhang, N. Suzuki, E. Shamoto. Investigation on machining performance of amplitude control sculpturing method in elliptical vibration cutting. Procedia CIRP 2013, 8: 328-333. (14th CIRP Conference on Modeling of Machining Operations, Torino, Italy)

2-2 J. Zhang, N. Suzuki, T. Kato, R. Hino, E. Shamoto. Influence of material composition on ductile machining of tungsten carbide in elliptical vibration cutting. Key Engineering Materials 2012, 523-524: 113-118. (14th International Conference on Precision Engineering, Hyogo, Japan)

Other conference paper:

3-1 J. Zhang, N. Suzuki, E. Shamoto. Micro machining of binderless tungsten carbide by applying elliptical vibration cutting technology. Conference of The Japan Society for Abrasive Technology(ABTEC), Kasugai, Japan, 2011: 109-114 (Best paper award).

Acknowledgements

It is my great honor to study in Ultra-precision Engineering Research Laboratory in Nagoya University. I would like to express my deepest gratitude to my supervisors, Associate Professor Norikazu Suzuki and Professor Eiji Shamoto for their valuable guidance and enthusiastic encouragement while working on this research project. I am also most grateful to them for their encouragement on my daily life in Japan.

Prof. Suzuki is always patient and enthusiastic to explain the problems both on the theoretical and experimental details. He taught me how to make scientific analyses and creative ideas in research work and more important how to be an excellent engineer. He gave me so much kind help and enthusiastic encouragement to overcome hard times.

Prof. Shamoto gave me this precious opportunity to study ultra-precision machining technology in Japan. He provided me with warm study environment and excellent machining equipments. He has broad spectrum of knowledge and creative ideas, and gave me so much valuable guidance and comments on my research works.

And also, I would like to thank Associate Professor Rei Hino for his helpful suggestions in research work and kind caring in my daily life. I would also like to thank Assistant Professor Sencer Burak for his encouragement on my daily life and the kind help on checking my journal papers in English. Moreover, I would like to express my gratitude to the PhD. student Takehiro Hayasaka for his much helpful assistance on checking my journal papers and doctoral dissertation.

Appreciation goes to Dr. Yilong Wang and PhD. student Yingjie Li in particular for their helpful suggestions in research work and encouragement in my daily life. I want to thank graduated student Mr. Daisuke Yamauchi for teaching me how to operate machine tools and measurement equipments in our lab. I also want to thank Mr. Yasuhiro Masanaka for his assistance in experiments and Ms. Tomoko Ishihara for her assistance in kinds of applications.

I am very grateful to Professor Tao Sun and Associate Professor Wenjun Zong from Harbin Institute of Technology in China to introduce me the research field of precision engineering.

I would like to particularly thank Professor Hirofumi Suzuki from Chubu University and Professor Noritsugu Umehara from Nagoya University for their valuable time and effort to give me the helpful guidance in my PhD thesis modification.

I would also like to express my sincere thanks to the China Scholarship Council (CSC) for their financial support.

Finally, I would like to thank my parents, my wife, my sister and all the family members for their encouragement and selfless love. Especially to my father, best wishes!